Development of advanced criteria for blade root design and optimization

Original
Development of advanced criteria for blade root design and optimization / Alinejad, Farhad. - (2018 Jul 17).

Publisher:
Politecnico di Torino

Published
DOI:10.6092/polito/porto/2711560

ScuDo
Scuola di Dottorato ~ Doctoral School
WHAT YOU ARE, TAKES YOU FAR

Doctoral Dissertation
Doctoral Program in Mechanical Engineering (30.th cycle)

Development of advanced criteria for blade root design and optimization

Farhad Alinejad

* * * * * *

Advisors
Prof. Daniele Botto
Prof. Muzio Gola

Doctoral Examination Committee:
Prof. Robert Parker, Reviewer, University of Virginia Tech.
Prof. Franco Furgiuele, Reviewer, Università della Calabria.
Prof. Mauro Filippini, Politecnico di Milano.
Prof. Carlo Rosso, Politecnico di Torino.
Prof. Maria Pia Cavatorta, Politecnico di Torino.

Politecnico di Torino
July 17, 2018

I hereby declare that, the contents and organisation of this dissertation constitute my own original work and does not compromise in any way the rights of third parties, including those relating to the security of personal data.

. . . .

Farhad Alinejad
Turin, July 17, 2018

Summary

In gas and steam turbine engines, blade root attachments are considered as critical components which require special attention for design. The traditional method of root design required high experienced engineers yet the strength of the material was not fully exploited in most cases. In the current thesis, different methodologies for automatic design and optimization of the blade root has been evaluated. Moreover, some methods for reducing the computational time have been proposed.

First, a simplified analytical model of the fir-tree was developed in order to evaluate mean stress in different sections of the blade root and disc groove. Then, a more detailed two-dimensional shape of the attachment capable to be analyzed in finite element (FE) analysis was developed for dovetail and fir-tree. The model was developed to be general in a way to include all possible shapes of the attachment. Then the projection of the analytical model over the 2D model was performed to compare the results obtained from analytical and FE methods. This comparison is essential in the later use of analytical evaluation of the fir-tree as a reduction technique of searching domain optimization. Moreover, the possibility of predicting the contact normal stress of the blade and disc attachment by the use of a punch test was evaluated. A puncher composed of a flat surface and rounded edge was simulated equivalent to a sample case of a dovetail. The stress profile of the contact in analytical, 2d and 3d for puncher and dovetail was compared.

As an optimizer Genetic Algorithm (GA) was described and different rules affecting this algorithm was introduced. In order to reduce the number of callbacks to high fidelity finite element (FE) method, the surrogate functions were evaluated and among them, the Kriging function was selected to be constructed for use in the current study. Its efficiency was evaluated within a numerical optimization of a single lob. In this study, the surrogate model is not used solely in finding the optimum of the attachment shape as it may provide low accuracy but in order to benefit its fast evaluation and diminish its low accuracy drawback, the Kriging function (KRG) was used within GA as a pre-evaluation of the candidate before performing FE analysis. Moreover, the feasible and non-feasible space in a multi-dimensional complex searching domain of the attachment geometry is explained and also the challenge of a multi-district domain is tackled with a new mutation operation. In order to rectify the non-continuous domain, an adaptive penalty method based on Latin Hypercube Sampling (LHS) was proposed which could successfully improve the optimization convergence. Furthermore, different topologies of the contact in a dovetail were assessed. Four different types of contact were modeled and optimized under the same loading and boundary conditions. The punch test was also assessed with different contact shapes. In addition, the state of stress for the dovetail in different rotational speed with different types of contact was assessed.

In the results and discussion, an optimization of a dovetail with the analytical approach was performed and the optimum was compared with the one obtained by FE analysis. It was found that the analytical approach has the advantage of fast evaluation and if constraints are well defined the results are comparable to the FE solution. Then, a Kriging function was embedded within the GA optimization and the approach was evaluated in an optimization of a dovetail. The results revealed that the low computational cost of the surrogate model is an advantage and the low accuracy would be diminished in a collaboration of FE and surrogate models. Later, the capability of employing the analytical approach in a fir-tree optimization is assessed. As the fir-tree geometry has a higher complexity working domain in comparison to the dovetail, the results would be consistent for the dovetail also. Different methods are assessed and compared. In the first attempt, the analytical approach was adopted as a filter to select out the least probable fit candidates. This method could provide a 7% improvement in convergence. In another attempt, the proposed adaptive penalty method was added to the optimization which successfully found the reasonable optimum with 47% reduction in computational cost. Later, a combination of analytical and FE models was joined in a multi-objective multi-level optimization which provided 32% improvement with less error comparing to the previous method. In the last evaluation of this type, the analytical approach was solely used in a multi-objective optimization in which the results were selected according to an FE evaluation of most fit candidates. This approach although provided 86% improvement in computational time reduction but it depends highly on the case under investigation and provides low accuracy in the final solution. Furthermore, a robust optimum was found for both dovetail and fir-tree in a multi-objective optimization. In this trial, the proposed adaptive penalty method in addition to the surrogate model was also involved.

Acknowledgements

Firstly, I would like to express my sincere gratitude to my advisors Prof. Daniele Botto for the continuous support of my Ph.D. study and related research, for his patience, motivation, and immense knowledge. His guidance helped me in all the time of research and writing of this thesis. I could not have imagined having a better advisor and mentor for my Ph.D. study.

In addition, I would like to express my deepest appreciation to dear Prof. Muzio Gola for his patience, his grateful advice and directions for my research. In addition to be an adviser, he was more like a friend to me and widened my view of the world.

Moreover, I would like to acknowledge ANSALDO Energia S.p.A. and thank Mr. Andrea Bessone, Mrs. Laura Traversone and all the staff who provided an opportunity to join their team as a researcher and provided me research facilities. Without they precious support it would not be possible to conduct this research.

Besides my advisors, I would like to thank dear professors in AERMEC lab group, Prof. Tresa Berruti, Prof. Christian M. Firrone, Prof. Stefano Zucca and Prof. Mario Lavella for their help, encouragement and support.

I thank my fellow office mates Dr. Ciara Gastaldi, Dr. Giuseppe Battiato, Dr. Muhammad Umer and Dr. Marco Lassalle for sharing their office with me and all the fun and joy we had during my stay in Italy besides to answer all my crazy questions.

I would like to dedicate this thesis to my loving parents.

Contents

List of Tables

List of Figures

Chapter 1

Introduction

1.1 Background

In gas and steam turbine industries, in order to obtain a high reliability and efficiency, the turbine blade attachments are considered as critical components which require special attention in their design [38]. In such engines, discs and blades are usually exposed to high temperature and high rotational speed. High rotational velocity develops huge centrifugal forces besides high temperature deteriorates the strength of the material [108]. Therefore the contact interaction between the blade and disc in the attachment generate high-stress profiles in normal operation of an engine [38]. This high contact stress in addition to a rather small relative displacement between mating surfaces in the contact may develop fretting fatigue and subsequently lead to premature failure of the components [91]. Fretting fatigue is not the only failure mode of the gas turbine disc attachment, there are some other modes of degradation and failure for the critical components such as low cycle and high cycle fatigue, creep, static yielding, corrosion and erosion in addition to wear, etc. [108]. The airworthiness of the aero gas turbines mandates the investigation of any possible failure of the blade. Any failure in one blade often provide a subsequent failures of downstream stages and finally lead to loss of engine. Failed blades in an aero engine have been mechanically analyzed by Hou et al. [41] in addition to metallurgical examination to identify the cases of failure. They found the low cycle fatigue in the top fir-tree root as the main initiation cause of failure proceeding with high cycle fatigue. Through a nonlinear finite element model of the blade and a sector of the disc in a pre-stressed modal analysis found maximum stress area coincide with the point of crack initiation.

The most frequent shape used in the blade and disc attachments are of two types of fir-tree and dovetail [78]. Meguid et al. [61] performed a comprehensive stress analysis of a fir-tree for an aero engine in 2D and 3D finite element method. They also validated their study by an automated photoelastic stress freezing technique along the interface of fir-tree components. In their study, some different features of the fir-tree affecting the state of stress have been evaluated such as number of lobs, contact slop and length. They suggested applying the 2D analysis for the design of the attachment with caution as it underestimates the maximum stress in the contact region. Similar results were reported by Papanikos et al. [74] for a dovetail attachment. In both studies, the crack initiation has been reported in the lower part of the contact where maximum stress concentration occurs. Rajasekaran et al [78] simulated the profile of contact stress in a dovetail blade root with a punch having a flat surface with rounded edges. They applied a short crack arrest method to predict the fatigue from the stress profile obtained with their simulation which had a good agreement comparing to the experimental results. In a study performed by [67], they found that the stress distribution plays a dominant role in fretting fatigue at the contact edge. They applied a proposed generalized tangential stress range – compressive stress range (TSR-CSR) diagram as a fretting fatigue failure criterion on a dovetail joint. Moreover, on the importance of relative displacement on fretting fatigue in the contact Nowell et al [71] performed a series of fretting fatigue experiments to evaluate the effect of contact relative displacement. They approved the Ruiz fretting fatigue parameter [83] is able to predict the initiation of the fretting crack. The peak stress has an important role in the life of the component under contact. Wei et al [106] by introducing a plastic model, described the high gradient stress at the edges of the contact in a dovetail. They performed the live evaluation with an energy-based critical plane equation for initiation prediction and a Paris formulation combining modified stress intensity factor to evaluate the propagation life. They found that the high gradient stresses at the edge of contact are always higher than the yield stress. Although the plastic zone around the high gradient stress is very small, the relaxation also does not reduce the peak significantly.

Over the last several decades, the computational mechanics has empowered designing for the industry. The energy market is not an exception, moreover, the increased demand of optimum design to benefit higher performance and efficiency with even lighter components (which is a critical issue for aviation) is demanded in the industry of gas turbine. Furthermore, the multidisciplinary analysis in this field makes the design process more complex and a large computational load is needed to reach the final product [1]. Moreover, automatic design optimization in mechanical engineering has been recently gained lots of attention due to the complexity of the modern designs. The market demand for increased efficiency and performance of the components in addition to the reduction of costs of design has always motivated engineers to apply improved methods with less computational cost in design [75]. Although commercial software including modern CAD systems in addition to various FE analysis packages provide a significant control over generation and alteration of the component geometry under design [20], an improvement in reducing computational burden by considering the characteristics of every problem differently. Such achievement can be obtained by incorporating different methods which best matches the problem under consideration. On the other hand, such optimization needs a high intervention of human in preparing the geometry of the component, preparing the meshed model for FE analysis, performing the analysis and interpreting the results and provide decisions in making the next amendment to the design for obtaining a target in the performance. Admitting the high demand for rapid improvement of the design from idea to the product requires diminishing the interference of human decision in the design process and performing the automatic optimization [19]. The optimization may be applied to the preliminary stages of the design where the designer tries to find the best arrangement of parameters of the system to satisfy the constraints and improve the performance. Furthermore, the optimization can be applied to an already designed component in order to improve its efficiency and performance [98].

There are different approaches to tackle the optimization problems. Hahn et al. [38] studied a number of optimization methods with different response functions in searching for a more efficient approach in designing the blades. They employed a combination of Abaqus and Isight to minimize the contact pressure and stress in a dovetail of a turbine blade. The parametric model with a nine variable parameters as input was developed and assessed by the optimizer. Some different optimizer were used in their study including, evolutionary optimization, direct, gradient and exploratory method. They used two surrogate models of Response Surface Method (RSM) and Elliptical Basis Function (EBF) although did not mention how they handled the problem of making the inverse of the correlation matrix in a highly correlated variables problem for obtaining the Mahalanobis distance. In the first level of optimization, they used optimal Latin Hypercube approximation for predicting the optimum values and also the sensitivity of the design to the selected design variables. In the second level of optimization, a limited number of parameters were selected, then, different optimization methods were applied. They found the evolutionary method and genetic algorithm as the most promising method in this problem. A gradient-based and modern stochastic method was applied to optimize a blade and disk fir-tree attachment by W. Song, et al. [99]. They found that the combination of gradient-based method with Genetic Algorithm (GA) provides a better optimum in comparison with the direct gradient-based search. In another work, Song et al. [98] defined constraints including all mechanical, geometrical and material limits to accommodate only one objective for a multi-level optimization of a fir-tree attachment which helped in a faster convergence. Later, Song and Keane [97] proposed an original optimization framework in which combining a surrogate function and genetic algorithm, minimized the number of callbacks to the high fidelity expensive code. Recently, D. Botto and F. Alinejad [18] tried to optimize a two dimensional dovetail attachment parametric geometry. They merged a surrogate function into the genetic algorithm optimization to successfully reduce the number of call backs to the high fidelity model. In every iteration, the surrogate model matured by being fed with a number of new training samples evaluated by the high fidelity model and provided more proper predictions, consequently, reduced the need for the high fidelity callbacks in the optimization process.

1.2 Motivation

The main purpose of the structural optimization is to find the best set of parameters (control parameters) defining the geometry of the structure that the structure behaves more effectively in a predefined interested property (output) of the structure under question. The efficiency and performance of engineered components are connected to their geometrical features. Therefore, in a design of any component, the optimal shape design has always been an interesting subject for many engineers. There are three types of shape optimization [40]:

1. Optimization of size: in this type, the aim is to find the best value (or vector of values) for a parameter (or set of parameters) related to the size of the component geometry (e.g. the thickness distribution of a cantilever beam or a plate under normal force);

2. Optimization of geometry shape: when the topology of the component is agreed during the design, a set of parameters to define the geometry is found then the structure optima is found without changing the topology. The different size properties of the geometry are tuned in this type also but the difference from the previous category is that the size changing makes the shape of the geometry is different from the original (initial) shape.

3. Optimization of topology: In this type of optimization not only different parameters defining an agreed shape is gone under assessment to find the optima but also the topology itself undergo changes to evaluate the possibility of finding an optimal topology for the problem under investigation.

Often due to the expensive process of designing geometry for the blade root, some complex profiles and different dimensions are prevented. Recently, the needs for an integrated device capable of responding to “what ifs” in an accurate and also fast way have been increased. “What if” is an important question raised during a design process for many engineers. In fact, the design is not satisfactory if this question has not been answered properly. Especially in the case of a complex coupled system, it is hard to understand the output consequents of any change to different input parameters of the system [94]. Fretting and low cycle fatigue has been reported mostly as the main cause of failure in gas turbine attachment failures ([10], [109], [103], [41], [106], [86], [91], [56]). Hence, the designers try to lessen the state of stress in the attachment as the main concern during the design to increase the service life of the components. The reduction in the stress may be provided by a more proper shape having more uniform stress and less peak stress or sometimes less weight of the components (related to frontal area in gas turbine terminology) which is again a shape modification problem ([37], [19], [24], [108], [61], [74], [73], [83], [98], [97] and [38]).

Figure 1.1 illustrates a typical fir-tree shape of the blade root attached to the disc. As seen, the centrifugal loads of blade in addition to other loads are transmitted through these attachments to the disc. Hence, the capability of the attachment to tolerate the extreme stress generated during the working conditions has a prior importance for the designer. It appears from the aforementioned investigations that there are some studies

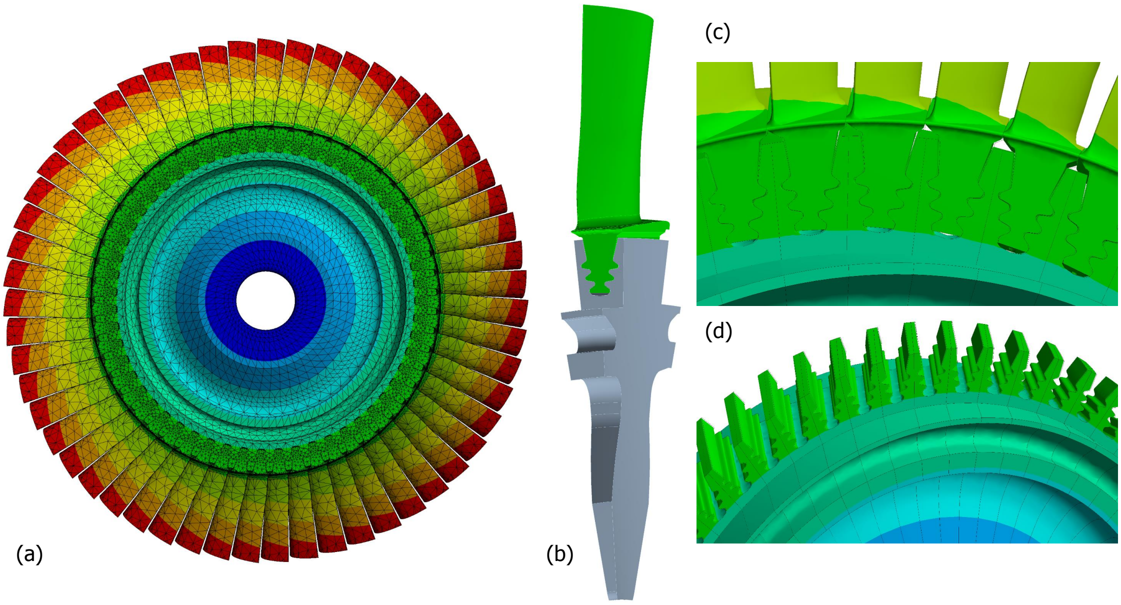

Figure 1.1: Blade and disc typical fir-tree attachment. a) Full disc and blades, b) Blade and its corresponding disc section, c) Close view of the fir-tree attachment, d) Fir-tree groove on the disc.

conducted to find the optimum blade root shape. However, limited studies provided a practical methodology in finding the optimum shape of the attachment with less computational effort. Moreover, very few works have investigated the effect of non-feasible space in a complex multi-dimensional domain of optimization process. The optimization has a close contiguity with the robustness, thus in this study, the robustness is also considered in the final optimum solution.

In the current study parametric models have been developed to define different attachments for blade and disc joint. Then, using different approaches in response function, penalty function and optimization algorithm, it was tried to reduce the computational cost in finding the optimum root shape. Different criteria were studied in multi-objective optimization.

1.3 Structure

In order to obtain a multi-objective robust optimum solution in a design, it is required to incorporate a parametric model of the geometry, response function (such as finite element analysis or surrogate functions) and optimization algorithm [58]. In the current thesis, it was tried to minimize the details and devote most part of the context to the principal flow of the study and results. The appendixes are to provide the reader more details if needed.

Chapter two initiates with the parametric model of the attachment. Two most popular types of dovetail and fir-tree have been modeled in parametric geometry in analytical and Finite Element (FE) analysis. The analytical approach is referred to a 1D model as the stress evaluations are performed just in one dimensional and the FE approach is referred to the 2D model as the analysis has been done in plane strain mode. The main purpose of this chapter is to provide the input variable parameters governing the shape of the attachment. The optimizer tries to find the optimum solution by manipulating these parameters which are named ‘input vector’. After detail inspection of the dovetail shape, a parametric model has been proposed for the fir-tree. In this chapter, the reader is introduced with the simple topology of the attachment. In chapter five, this parametric model is more improved to involve more types of topology for the attachment. Finally, the analytical simplified fir-tree model is projected on a 2D practical model of fir-tree and the results obtained from analytical and FE methods are compared. This comparison is essential in a later use of analytical evaluation of the fir-tree as a reduction technique to the searching domain in optimization in section 6.3.

Chapter three examines the possibility of predicting the contact normal stress of the attachment by the help of its equivalent punch test for which the analytical solution is available.

Chapter four tries to introduce the optimization algorithm used in the current thesis in addition to surrogate function developed to reduce the computational burden of the problem. To take more advantage out of surrogate model while avoiding its drawback of low accuracy in prediction, the Kriging model has been embedded within a Genetic Algorithm (GA) optimization as a filter before high fidelity FE model. Moreover, in this chapter, the feasibility of the input vector is explained. To provide a continuous domain out of feasible and non-feasible space an innovative adaptive penalty method using Latin Hypercube Sampling (LHS) has been proposed which unburden the computational load effectively. A standard benchmark for assessment of optimization algorithms named Rastrigin function, in addition to a dovetail and fir-tree parametric models were optimized by the proposed method in order to highlight its capabilities.

Chapter five introduces some different topologies of the contact in the attachment. Four different types of contact have been modeled and optimized under the same loading and boundary conditions. The punch test was also simulated with different contact shapes. Also the state of stress for the dovetail in different rotational speed with different types of contact was assessed.

Chapter six begins with an optimization of a dovetail with analytical approach and compared the optimum with the one obtained by FE analysis. Then the combination of GA and surrogate model is evaluated in an optimization of a dovetail. Later, the capability of employing the analytical approach in a fir-tree optimization is assessed. Different methods are evaluated and compared. Finally, the proposed adaptive penalty is applied to optimization of a dovetail and also a fir-tree. Also, robustness analysis is considered in this chapter.

Chapter seven sums up the finding and results.

Chapter 2

Parametric Models

A parametric model development has a significant influence on the performance of the shape optimization. Some ideal properties for a parametric model are listed by Pierret [75] as,

- The number of parameters required to define a large variety of physical rational shape must be as low as possible.
- As much as possible, by random selection of parameters in their range of variation, the parametric model should still generate a realistic shape.
- Be able to adopt the existing geometry with as less effort as possible.
- Be generic meaning that it provides a large variety of shapes.
- The parameters lower and upper bounds should be clearly definable by the designer.

Parametric model defining is highly subjected to the response function one may use during the optimization. There are two major methods utilized in the current study, analytical and FE method. Although the surrogate model is also used to replicate the response of the FE model, the parametric model is not affected by its usage. Hence, two major types of parametric model are developed, namely, analytical approach and FEM approach parametric models. The parametric model for the FE approach has been prepared for two types of the most popular attachments, dovetail, and fir-tree. A detailed description of the parametric models is in Appendix A and some details about the geometry calculations are in Appendix B. Moreover, the APDL batch Flow Chart developed to analyze a dovetail parametric model prepared with MATLAB in the current study is described in Appendix C. In this chapter, firstly, a brief introduction is given, then, the two approaches have been compared in an evaluation on a 4-lob fir-tree.

2.1 Analytical approach – Simplified fir-tree

The blade fir-tree root has been simplified to a model composed of straight lines with no curve and fairings (a detailed description may be found in Appendix A.1). In this model, the main purpose is to have a rough estimation of the mean stress distribution in different sections of the blade root and the disc groove. The shape of the lobs is reproduced by triangles of the same size and fairly the same shape. To evaluate the loading and subsequent stress in different parts of the components, it was assumed that the contact loading hold by every lob is the same.

2.2 FEM Approach

2.2.1 Dovetail 2D parametric model

It was tried to prepare the most generic parametric model for the dovetail yet simple enough to minimize the computational effort in its assessment. Figure 2.1 illustrated the schematic of the disc and its grooves adapting the dovetail. The dotted blue circle in Fig. 2.1-a illustrates the limit of the disc attachment penetration into the disc. Figure 2.1-b illustrates the half section of the blade and disc attachment and 2.1-c shows the close view of the blade dovetail in red and its groove on the disc in black.

The main feature of this parametric model is that the length of the lob for the dovetail is conducted by two guiding lines, a and b which have the same origin on the symmetry line. There are 16 parameters altogether to define a complete 2D dovetail shape. Nevertheless, not all these parameters are contributed to the optimization search. Some of these parameters are derived from other in order to provide a predefined tolerance and some are considered constant but at least 6 variable parameters are required to perform the optimization. A detailed description of the dovetail 2D parametric model employed in the current study is in the Appendix A.2.

2.2.2 Fir-tree 2D parametric model

Similar to the 2D dovetail parametric model, a fir-tree parametric model of 2D has been prepared. Figure 2.2 illustrates the disc and groove embedding the fir-tree attachment in different views. The detailed description of the 2D parametric model is in Appendix A.3 and the geometry parameter details are in Table A.1. With no doubt, the number of parameters for defining this model is more than that of a dovetail. There are 18 parameters to define the shape of a simple 2D fir-tree shape but the least number of variable parameters contributing in an optimization run is 8.

In order to obtain at least 75% of accuracy in stress profile obtained from a contact, Sinclair et al. [93] recommended setting the element size of the order of 1% of the radius at the contact edge. In an optimization, as there is a comparison among different shapes,

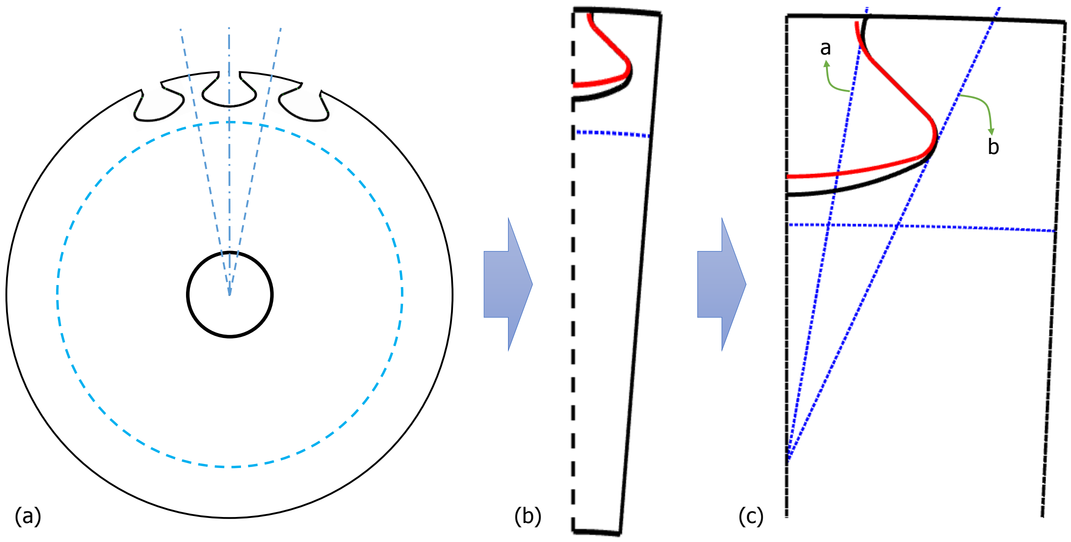

Figure 2.1: Dovetail attachment: a) disc, b) half section of the dovetail and corresponding disc c) close view of the dovetail.

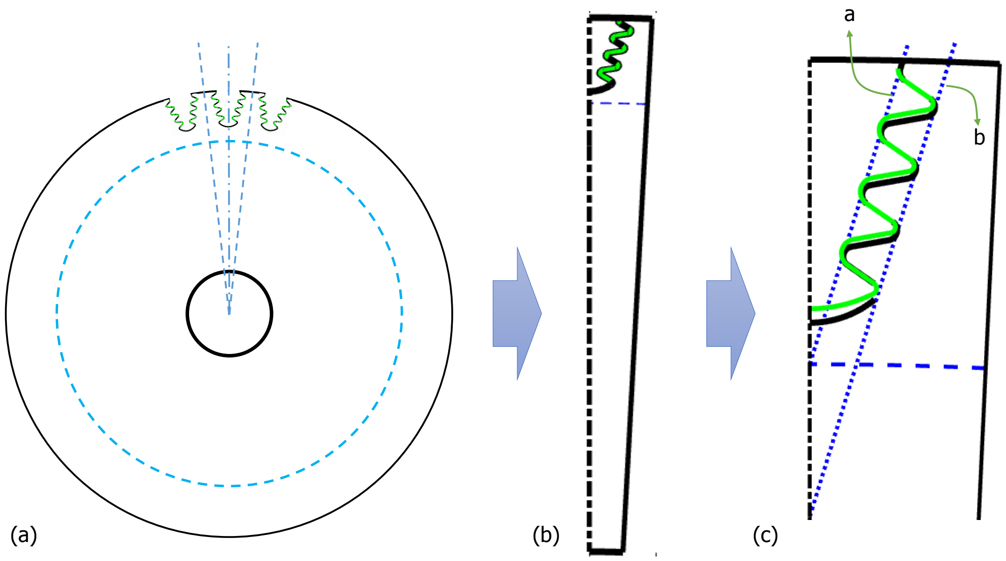

Figure 2.2: Fir-tree attachment: a) disc, b) half section of the Fir-tree and corresponding disc c) close view of the Fir-tree.

the accuracy of the peak contact stress is not the priority. In the current study, the coarse

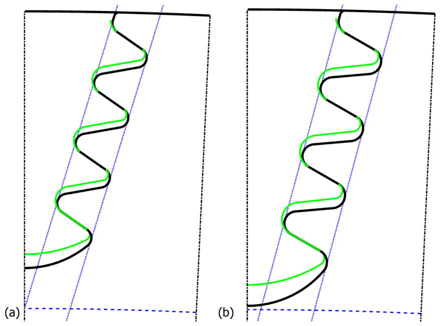

Figure 2.3: Sketch of two random fir-tree shapes

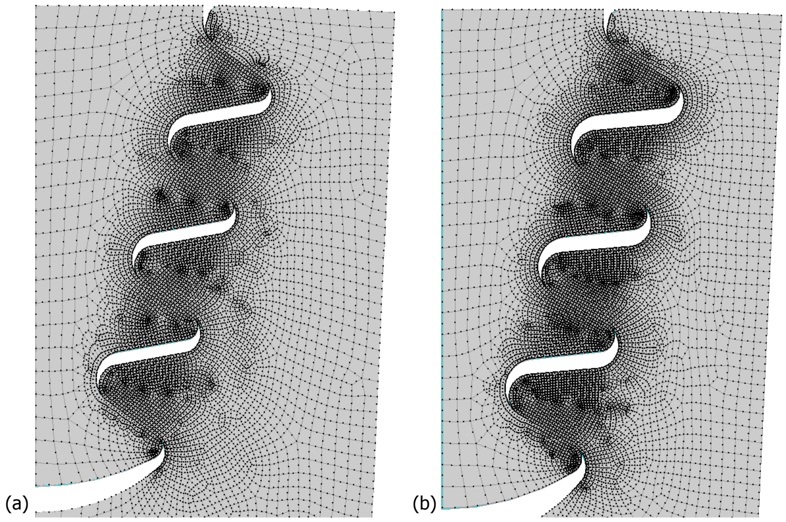

Figure 2.4: Mesh density for two random fir-tree shapes

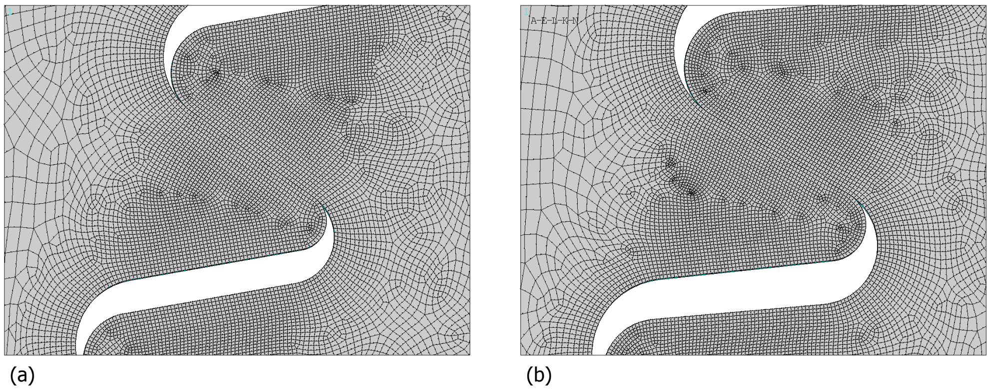

Figure 2.5: Similar mesh density on contact area for two random fir-tree shapes.

mesh sizing (as defined by Sinclair et al. [93]) was applied but also the density of the element size in the contact surfaces has been forced to maintain the same for all samples during optimization. Such objective has been accomplished by defining a constant sizing in the FE model for contact edges and the same density of mesh for the rest of the components for all samples. Figure 2.3 compares two random sketches of the fir-tree (a and b) and Fig. 2.4 illustrates the uniformity of the mesh density in the two samples. Figure 2.5 shows the similarity of automatically generated mesh density in contacting surfaces between the two random samples.

2.3 FE and Analytical Methods Comparison on Fir-tree

In order to evaluate the stress in different sections of the fir-tree attachment, without using the Finite Element Method (FEM), a simplified model is evolved from the original one. Figure 2.6-a illustrates the simplified fir-tree model. In this model, an individual lob is modeled with two straight lines (red lines) originating from the intersection of the curves to guiding lines. As there is not an accurate analytical method available for determining the load sharing among the lobs of a fir-tree, the contact force is assumed to be the same on every individual lob as a rough estimation. Hence, the loads on every section of the blade root and also the disc area is evaluated by knowing the elementary input parameters. In a simplified lob (2.6-b), the W_t is the contact length, α_t is the angle of contact line relative to the wedge angle, γ, which has the same value as of the parameter α_a (see Fig. A.6).

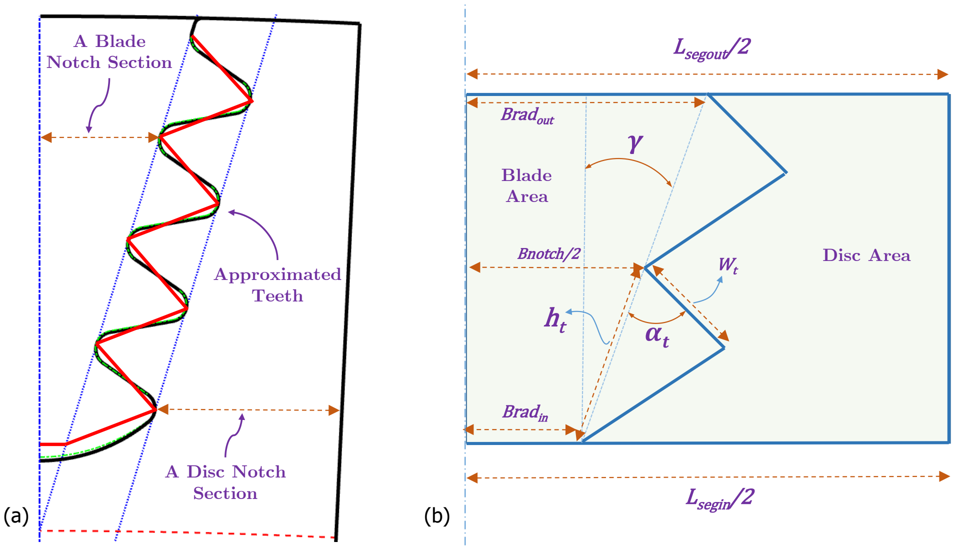

Figure 2.6: a) Projection of Analytical Simplified model of a fir-tree b) Sketch details of the derived model.

From a simplified model, nine values are calculated; four are the average stress on the blade notch section (Fig. 2.7), another four are the average stress on the disc notch section, plus one value which is the average contact normal stress. The stress values are normalized to their corresponding material ultimate stress value in order to provide the possibility of comparing.

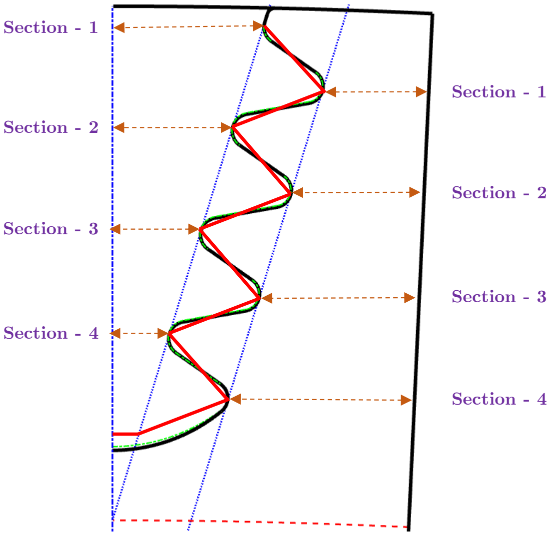

Figure 2.7: Different neck sections on blade and disc attachment.

For every notch of the blade and disc, there is one mean tensile stress calculated. Hence, for the case sample in this section, there are four values for blades and four values for the disc sector. From every four values, the max value is selected out. Also, as it is assumed to have the same contact force for every lob, there is just one value obtained for the contact pressure. Consequently, at the end of the analytical evaluation, there are just three values obtained from the blade and disc fir-tree attachment. One is the max mean tensile stress on blade and another is the same value for the disc and the last value is the contact mean normal stress. All values are normalized to their corresponding material ultimate stress (the contact pressure is normalized to the blade ultimate stress).

As seen in Fig. 2.8, every lob is simplified with two lines (red dotted lines), which connects the intersection of the curves with the guiding lines. For obtaining the mean contact pressure, the normal force on every lob is divided to the length of contact and the axial thickness of the component. But in this study, it was found that using the length of line-2 (see Fig. 2.8) underestimates the results in comparison to the results obtained from the FE method. Hence, the actual contact length (line-1) was used for the calculation of mean contact stress.

Figure 2.9 illustrates the boundary conditions and the loading on the simplified model of the fir-tree. The centrifugal load of the blade F_{blade} is applied on the lower part of the shank and the reaction force F_{reaction} exerted to the disc is the sum of F_{blade} plus

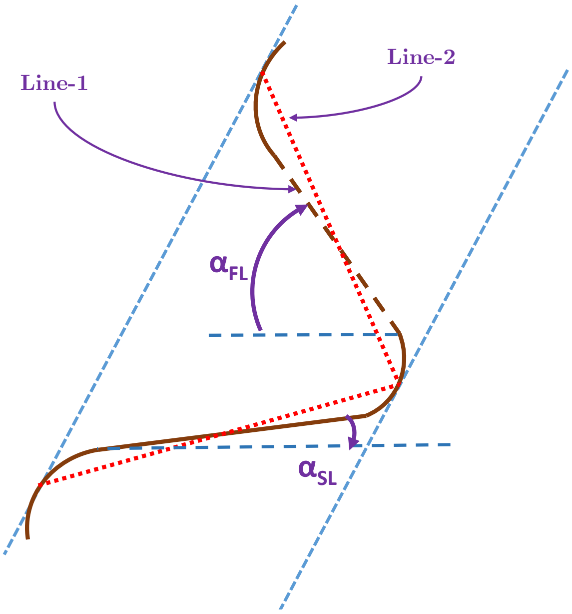

Figure 2.8: Simplified lob in a fir-tree.

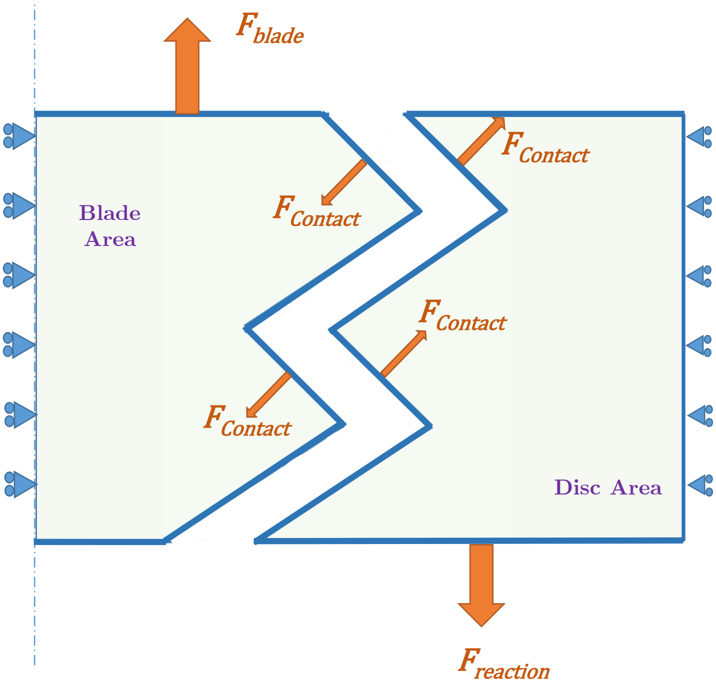

Figure 2.9: Boundary conditions and loadings for simplified analytical fir-tree parametric model.

Table 2.1: Specification of the sample trail in the analytical and FE analysis (Parameters definitions are found in Table A.1).

Specification	Value	Specification	Value
Number of Lobs	4	P_a	334 (mm)
Number of Blades	68	P_b	349 (mm)
Hub radius	404 (mm)	R_{C1}	1 (mm)
Axial Length	48.4 (mm)	R_{C2}	1 (mm)
Rim Radius	216.5 (mm)	R_{CA}	10 (mm)
Centrifugal Force	$(0.436142)\omega^2(N)$	α_{FL}	35 (deg)
Rotational speed, ω	382 (rad/s)	α_{SL}	10 (deg)
Ultimate Stress Blade	500E6 (Pa)	Wedge angle (γ, α_a)	17 degree
Ultimate Stress Disc	1136E6 (Pa)	Disc Density	8219.8 (kg/m^3)
Blade Density	3910 (kg/m^3)	Coefficient of Friction	0

the centrifugal load due to the mass of the upper part of the disc section. Assuming a friction-less contact for mating surfaces, the contact force is normal to the contacting surfaces.

The applied loads and shape specifications for a trail case plus material properties are tabulated in Table 2.1. The mean tensile stress was calculated analytically by assuming the same contact normal load for every lobe. The four sections, for blade and disk, in which the tensile stress has been calculated are illustrated in Fig. 2.7. The analytical results are compared to the ones obtained from FE analysis in Tables 2.2 and 2.3 for blade and disc sections, respectively. Moreover, one may find a comparison between mean normal contact stress obtained analytically and numerically in Table 2.4. As seen the error values especially for the contact pressure is substantial but later in section 6.3, we will see that high error values have not a dramatic effect on the efficiency of analytical method in finding the optimum.

Table 2.2: The blade sections tensile stress normalized to the ultimate stress.

Section	FEM	Analytical	Error (%)
Section 1	0.1415	0.1480	4.6
Section 2	0.1460	0.1414	-3.1
Section 3	0.1199	0.1290	7.6
Section 4	0.0972	0.1012	4.1

Table 2.3: The disc sections tensile stress normalized to the ultimate stress.

Section	FEM	Analytical	Error (%)
Section 1	0.0296	0.0270	-8.8
Section 2	0.0472	0.0443	-6.1
Section 3	0.0615	0.0561	-8.8
Section 4	0.0660	0.0649	-1.7

Table 2.4: The normal mean contact stress in different lobs.

	FEM (MPa)	Analytical (MPa)	Error (%)
Lob 1	62.010	86.49	40
Lob 2	78.179	86.49	11
Lob 3	67.844	86.49	27
Lob 4	58.870	86.49	47

2.4 Conclusion

Some parametric models of the blade and disc attachment were developed both for FE analysis and simplified fast calculation analytical method. The FE parametric models were designed such that they have as low number of variable parameters as possible yet cover a wide range of shapes of their types. Two main types of blade root have been considered in the current study namely dovetail and fir-tree.

An automatic mesh generation was applied to the parametric model to maintain the same mesh density over contacting surfaces. Similar mesh density provides similar error on the resultant contact peak stress hence enabling comparison among different shapes in an optimization.

The analytical model developed had a similar order of error for the blade and disc notch sections average tensile stress but the mean contact pressure over lobs obtained by the simplified analytical method was far from the FE results (later we will see in section 6.3 that the exact value has the least importance as the trend of the results during optimization follows that of high fidelity model).

Chapter 3

Contact in Punch and Blade Attachment

In this section, the profile of contact normal stress is studied for the blade and disc attachment. Punch test is examined to evaluate its capability to emulate the profile of the normal stress on the contact of blade and disc attachment. Moreover, due to the high computational load of three dimensional FE analysis of the parametric model especially in the heavy process of optimization, it is demanded to know whether it is possible to use two-dimensional analysis to provide reasonable results. Due to simplicity, the dovetail has been selected as the blade and disc attachment type.

3.1 Punch test

Ciavarella et al. [24] studied the contact problem to calculate the stress state due to compression of an elastic flat punch having rounded edges over a compliant half-plane. Figure 3.1 illustrates the punch and the half-plane which are both elastic but their material properties may be dissimilar. The pressure distribution is obtained from,

$$\frac{bp(\phi)}{P} = -\frac{2/\pi}{\pi - 2\phi_0 - \sin(2\phi_0)} * \left\{ (\pi - 2\phi_0)\cos\phi + \ln\left[\left|\frac{\sin(\phi+\phi_0)}{\sin(\phi-\phi_0)}\right|^{\sin\phi} \times \left|\tan\left(\frac{\phi+\phi_0}{2}\right)\tan\left(\frac{\phi-\phi_0}{2}\right)\right|^{\sin\phi_0} \right] \right\} \quad (3.1)$$

where, $-\pi/2 \leq \phi \leq \pi/2$, then, ϕ_0 is calculated by solving,

$$\frac{2PR}{a^2E^\star} = \frac{\pi - 2\phi_0}{4\sin^2\phi_0} - \frac{\cot\phi_0}{2} \quad (3.2)$$

Now, b can be obtained having $b = a/\sin\phi_0$. Moreover, $E^\star$ is the equivalent stiffness of the two bodies,

$$\frac{1}{E^\star} = \frac{1}{E_1}(1-\nu_1^2) + \frac{1}{E_2}(1-\nu_2^2) \quad (3.3)$$

A detailed description of the governing equations is found in [24]. More details about the punch test analytical solution can be found in [42].

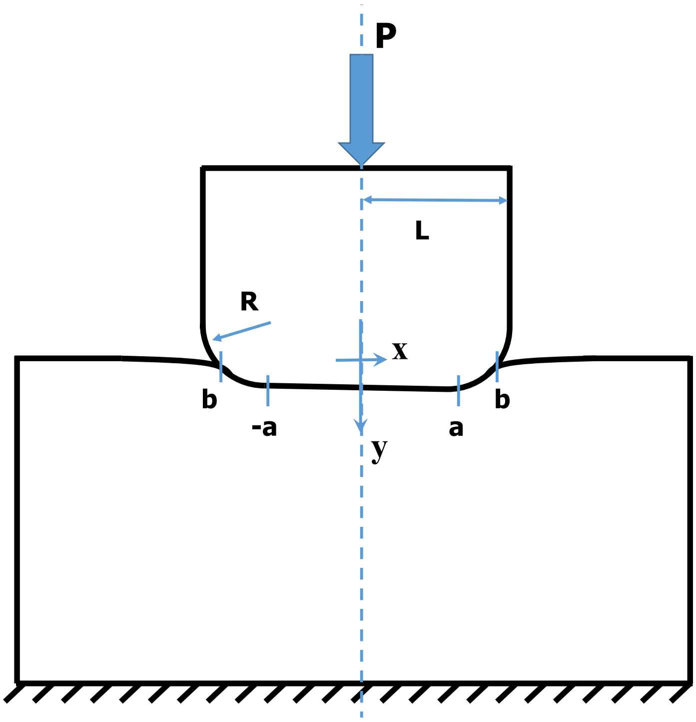

Figure 3.1: A schematic of a Punch test as a benchmark for analyzing the state of stress of contact in the dovetail. (a) is the end of the straight line, (b) is the end of closed contact status after applying the pressure P, L is the half of puncher span, R is the radius of the puncher edge.

3.2 Dovetail and equivalent Punch Model

The parametric model introduced in section A.2 was evaluated in this analysis. One sample model is considered for the rest of the analysis as an example. The contact slope is 44 degree and its length is 2.05 mm, R_{C1} for the disc is 0.39 mm and R_{C1b} is 2.2 mm. For the disc Inconel 718 and for the blade TiAl material has been selected. Total centrifugal load to the blade is 20 kN and as the thickness of the component is 20 mm the equivalent load on the punch is 721 [N/mm]. Furthermore, the equivalent radius of the puncher is,

$$\frac{1}{R_{eq}} = \frac{1}{R_{C1}} - \frac{1}{R_{C1b}} \rightarrow R_{eq} = 0.474(mm)$$

3.3 Contact Normal Pressure Profile

The 3D and 2D model of the dovetail has been analyzed using the FE method. The normal pressure profile in the contact area is under question in this analysis. Figure 3.2 illustrates the path from which the normal pressure is picked in the middle section of the component. The same data is extracted from the face of the component to have a comparison between the middle section and the face of the component. Moreover, the same dovetail model under the same condition with a different coefficient of friction has been analyzed to evaluate the effect of friction on the contact in a dovetail. To make the comparison, the equivalent punch has been modeled in 3D and analyzed by the FE model. The same path in the middle section of the model has been applied to obtain the normal pressure profile of the contact. Figure 3.3 illustrates the location of the path. Moreover, to provide high accuracy finer meshing has been applied to the contact area as illustrated in fig. 3.4.

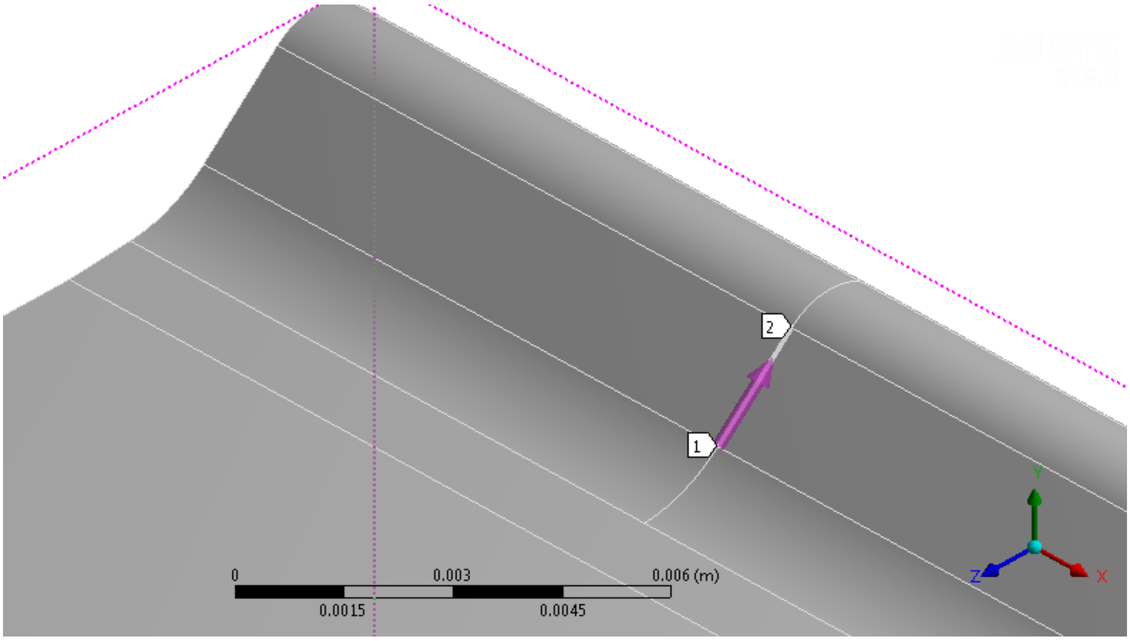

Figure 3.2: Dovetail FE model: location and direction of the path on which the contact normal stress is obtained.

Moreover, the punch test has been analytically solved and the profile of normal contact stress has been used as a reference for comparison. Figure 3.5 compares the contact normal pressure in the dovetail and its equivalent punch as a reference. As seen, the dovetail model having zero friction is more comparable to the punch result.

Figure 3.6 compares the results of the punch test in 2d and 3d FE analysis with the dovetail results and also with the reference. As seen the 2d and 3d analysis results of the punch test (in the face of the component) have no significant difference and both are

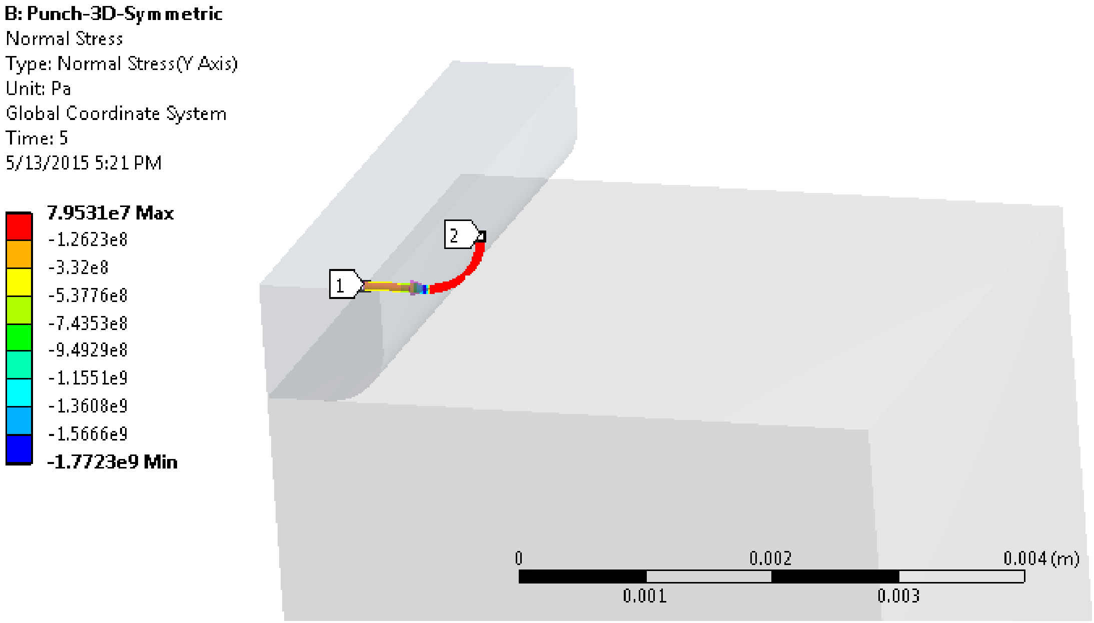

Figure 3.3: Punch test FE model: location and direction of the path for obtaining the contact normal stress.

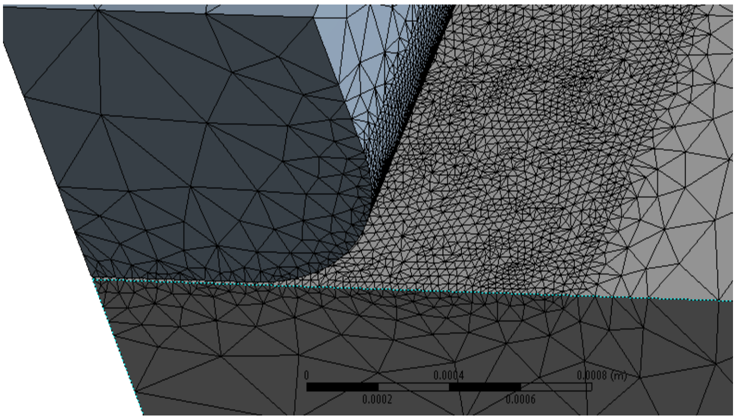

Figure 3.4: Punch 3D FE model mesh density in contact surfaces.

similar to that of dovetail in 3d no frictional analysis. The analytical profile of stress (reference) although predicted higher stress peak but follow the same profile of stress as for the dovetail.

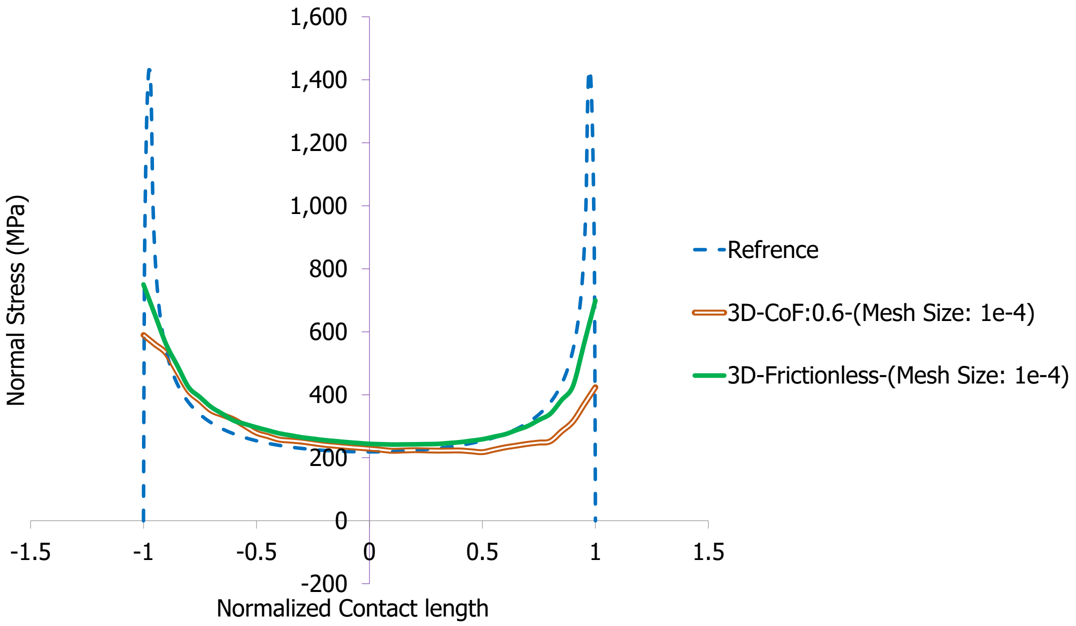

Figure 3.5: Comparison of normal stress in the contact area. The reference is the analytical solution of the punch test which is compared to the dovetail with and without friction.

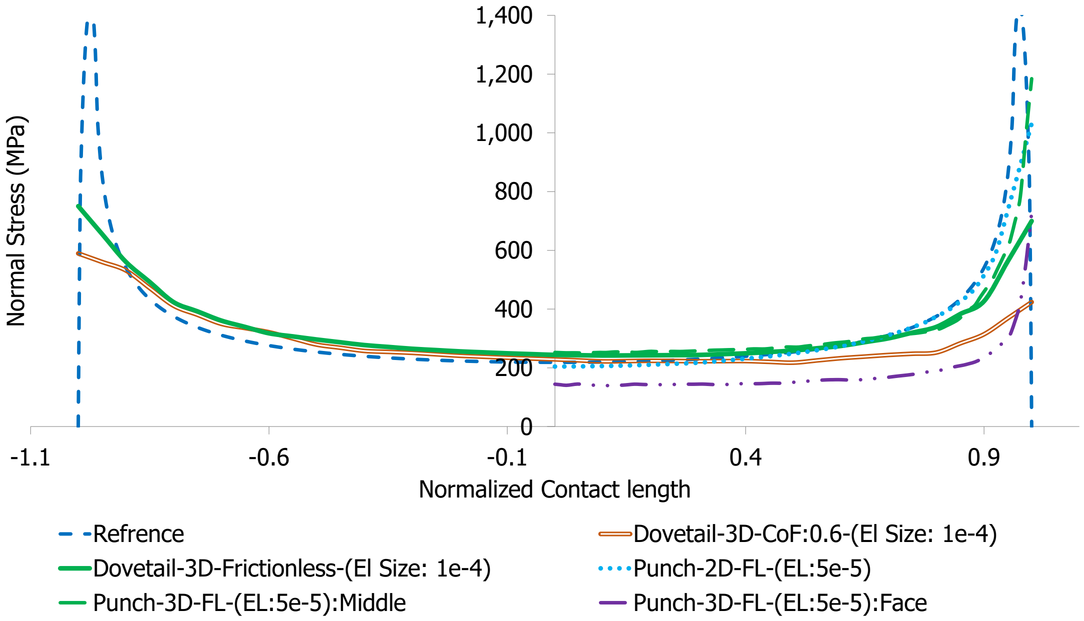

Figure 3.6: Comparison of contact normal stress among Dovetail and Punch test.

3.4 Conclusion

A punch test has been set up as a benchmark to emulate the profile of normal stress in the contact surfaces of a dovetail. 2D and 3D FE analysis were performed on both dovetail and its equivalent punch test in addition to normal stress analytical solution of the punch test.

The samples were evaluated with and without friction. It was found that the existence of friction provides less contact normal pressure for the dovetail as the load to be tolerated is shared between normal and tangential stress over contacting mates.

In the study of the 3D model of the punch test, it was found that the middle section of the puncher endures higher peak normal stress in comparison to the face of the component. Also, the 2D FE analysis results of the punch test had higher conformity to that of the middle section of the puncher, enabling the use of 2D FE analysis as an estimation of higher cost 3D analysis.

Chapter 4

Optimization and surrogate

Although there are a number of traditional searching methods for finding the optimum in a searching domain, they are not advisable for solving an optimization problem in a multi-dimensional complex noncontinuous system. By significant progress in the computational capability of computers in addition to the introduction of machine learning methods, there are advanced methods available as optimizers.

4.1 Genetic Algorithm

Among different methods of optimizations, Genetic Algorithm (GA) has shown to be effective to find the optima in a complex multi-dimensional searching domain [38], [77], [99], [65]). Therefore, for the current study GA has been applied. GA is a type of evolutionary computation which simulates a biological process. There are three main rules governs the GA which are Selection, Crossover and Mutation. There are a number of different methods developed for every rule which are explained in Appendix D. Furthermore, two sample problems are solved in this appendix to illustrate its capabilities in finding the optimal solution.

4.2 Surrogate Modeling

The surrogate modeling plays an important role in analysis and optimization of computationally expensive simulations. By processing the input parameters affecting the output, the surrogate model provides a numerical approximation of the output. The surrogates are constructed by processing some sample points determined by the high fidelity models using Design of Experiment (DOE) methods. Such a process is called Training. The Surrogate model provides a fast approximation of the outputs at new design points. Surrogate models (also known as response surface models or meta-models MMs) are used in place of the expensive simulation model during the optimization. One of the applications of this method is to create a simplified model of a system with unknown behavior (Expensive Black-Box Optimization Problems) and also surrogate models are used instead of computationally demanding models to speed up analyzing processes. The main drawback is that since a surrogate model is an approximation of the original model, the estimation errors are introduced to the problem. But the advantages overcome its drawback especially if a model simulation is computationally expensive. There are two major methods for construction of a surrogate function:

- Interpolation models: e.g. Radial Basis Function (RBF) and Kriging Function.
- Regression models: e.g. Linear Regression model and Support Vector Regression model.

A detailed description of these methods is found in Appendix E. Since, the accuracy of the surrogate functions are dependent to the training samples, the method for sampling the searching domain plays an important role in the final results obtained using surrogate-based optimization methods. There are two methods of sampling described in Appendix E from which the Latin Hypercube Sampling (LHS) has been selected for the current study for the cause of providing more uniform distribution in a working domain.

In the current study, the Kriging model has been used as a surrogate function. Some disadvantages of Kriging function are,

1. Kriging is very sensitive to noisy problems. Its prediction capability reduces by an increase of noise ([44]).
2. Due to the fact that a k-dimensional optimization is required in Kriging model to find the maximum likelihood estimate of the parameters in fitting the model, the kriging method needs higher computational burden comparing to other methods.
3. It is rather sophisticated in theory.

On the other hand, some advantages of Kriging function are,

1. It has a better accuracy comparing to other surrogate models ([77],[32]).
2. It has a statistical base which makes error estimation for new sample points possible.
3. Accept more training samples after construction which makes its accuracy higher during the adaptive mode.
4. In addition to estimating the response, the Kriging is able to provide an estimate of the posterior variance of the input vector under question. This capability makes possible the use of Kriging method embedded in GA optimization before applying the FE method as a response function ([18],[97]).

The advantages of Kriging function overweigh the drawbacks in the current study as the problem is not noisy (especially near the optimum) and the time to construct the Kriging model is negligible comparing to high fidelity calculation.

4.3 Evaluating and Validating Kriging Function

In order to evaluate the capability of Kriging function in reproducing the results of an FE analysis, the deflection of a single lob has been considered as a case study. In fact, it was favorable to know how much Kriging function is able to predict the deflection of a single lob under contact pressure and also the optimization using FE and Kriging models provide to what extent similar results. Hence, a simple lob was modeled with a parametric geometry similar to models described in section 2 but this model was quite simplified and had just two variable parameters which were L, length of the lob and H, the thickness of the lob root. Then, FE analysis was performed on this parametric model to obtain the bending displacement of the midpoint of the lob under a concentrated loading. The concentration loading was applied as the aim was to provide an alternative fast calculation function which provides an estimate of every lob bending stiffness and to be used embedded in simplified analytical model (which later we will see there is no need to provide such estimation as the assumption of similar load sharing for every lob provides enough efficiency in optimization of a fir-tree in section 6.3). Fig. 4.1-a illustrates the FE analysis of the single lob. Genetic Algorithm was applied on both FE and Kriging model with the objective of minimizing the bending deflection, i.e. the objective was minimum relative displacement of the midpoint of the lob, point S, to the root of the tooth, point D (Fig. 4.1 - b).

The comparison of the optimization done by FE and also the surrogate model is listed in Table 4.1). The number of initial populations prepared by DOE was 40 samples and the input variable parameters were arbitrarily limited to the range of [5, 30] mm. The error was calculated as,

$$Error = \frac{\delta_{Kriging} - \delta_{FEM}}{\delta_{FEM}} \tag{4.1}$$

where, δ is the deflection of the lob and subscripts FEM refer to the value obtained by FE analysis or the equivalent Kriging value of the FEM optimum depending on corresponding row or column selected. Likewise, subscript $Kriging$ refers to the value calculated by Kriging function or the FE analysis value obtained from the BBF optimum input vector. By looking at the first column of the table, it is seen that the error of the surrogate model (Kriging function) was approximately 0.01 which is negligible in comparison to the benefits of low computational time in case of there is a need to provide a rough estimation of the result with a fast evaluation. It is worth to know that the result of the Kriging model (Table 4.1) for other sets of parameters are also comparable to the FE solution.

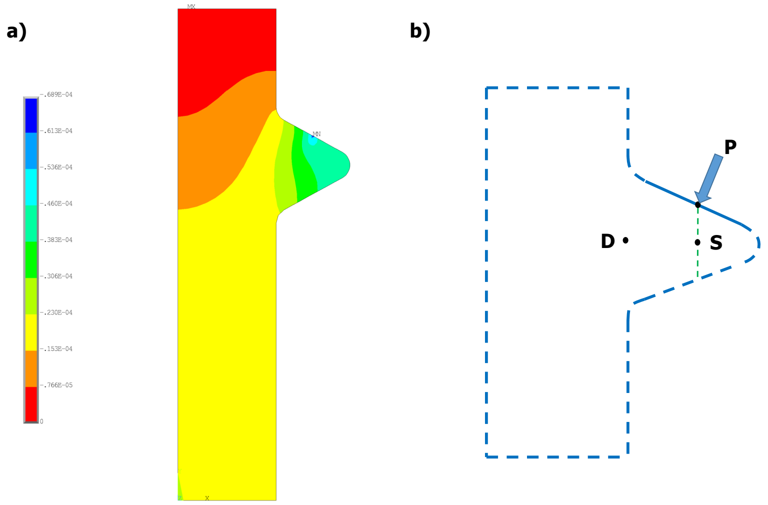

Figure 4.1: Lateral Deformation of a single tooth a) FE result, b) Position of S and D points.

Table 4.1: Optimum Values obtained via GA and Black Box Function

Fitness extraction method	Corresponding FEM Value	Corresponding Kriging Value	Error
FEM Optimum	2.35e-05	2.349e-05	-0.0005
B.B.F Optimum	2.37e-05	2.17e-05	-0.084
Error	0.010556	-0.07432	

4.4 Embedding Surrogate function in GA

In the previous section, it was found that the surrogate model has the advantage of fast calculation hence unloading the computational effort. On the other hand, accuracy in finding the optimum is questionable. The error of the optima found although is trivial, it is not negligible, especially for the optimization purposes, where small changes to the objective do matter. It means that although the Kriging model provides a fast estimation of the results but applying such model as a sole model for optimization may not provide a satisfied accuracy (which is the main goal of optimization because in an optimization every small amount of improvement does matter).

In order to benefit the fast calculation advantage of the surrogate model in addition to high accuracy of the FE model, the two models are used together in the optimization algorithm. Figure 4.2-a demonstrate FE analysis as a response function to the input vector. The objective value can be a stress value. In fig. 4.2-b a pre-evaluation of the input vectors by the surrogate model has been added before the FE analysis. By this pre-evaluation, most of the input points having a low probability of fitness in the searching domain will be filtered out. Therefore less call backs to the high fidelity FE model are needed. consequently, this approach lessen the computational burden.

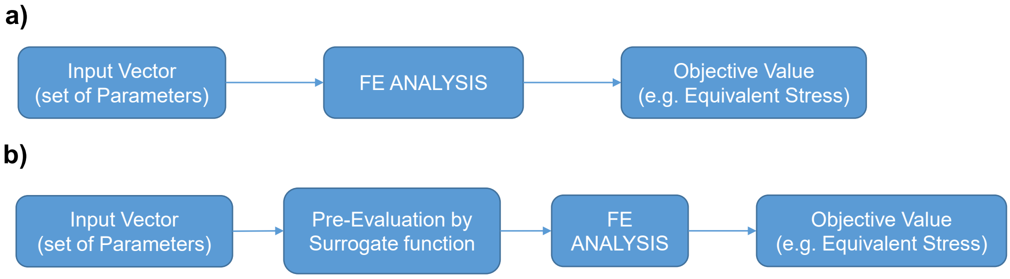

Figure 4.2: Response to input vector with a) FE analysis b)pre-evaluation added FE analysis.

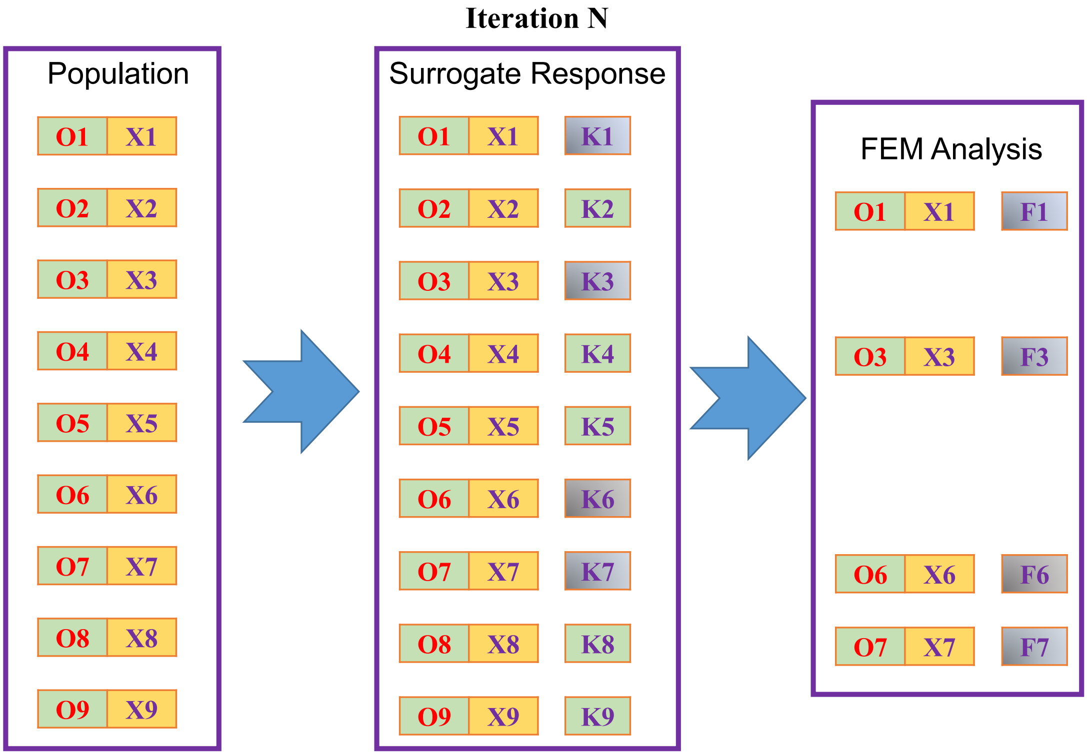

Figure 4.3: Population pre-evaluation by Kriging Function.

In fact, in every iteration the population is gone into evaluation process of surrogate function (in this case the Kriging function), then the highest probable fit samples are permitted to proceed to the rest of process. Figure 4.3 shows a schematic illustration of a population of nine sample points evaluated by Kriging then FE model. If one assumes

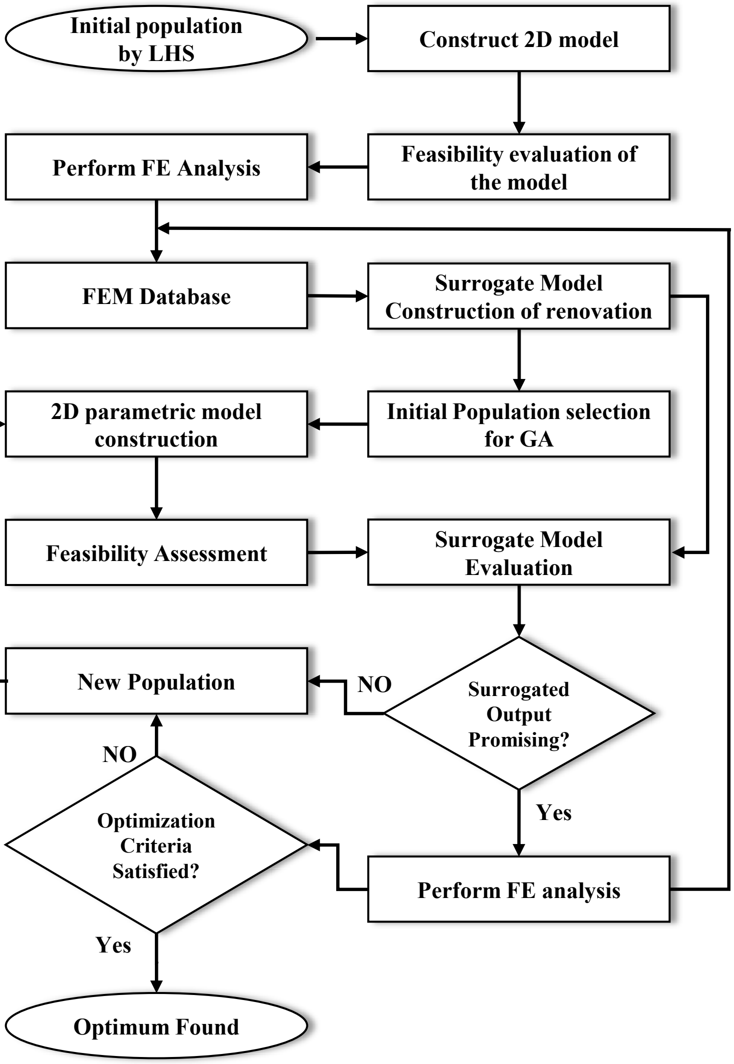

Figure 4.4: Embedding Kriging function into GA optimization.

a k dimensional input vector of every individual in a population as $\{p_1, ..., p_k\}$, for the sake of mating between parents this input vector should be divided into at least two vectors of $\{p_1, ..., p_m\}$ and $\{p_{m+1}, ..., p_k\}$ which are named vectors **O** and **X**, respectively. Moreover, **F** represents the objective value/s obtained by the FE model and **K** represents the response/s of the Kriging function.

The flowchart in Fig. 4.4 illustrates the idea of embedding the pre-evaluation of the surrogate model in GA. In every iteration, the results of the solutions done by FE model are collected and stored in a pool of training samples. The pool is sorted and a number of high fit samples are then fed to the Kriging model in every loop in order to improve its accuracy.

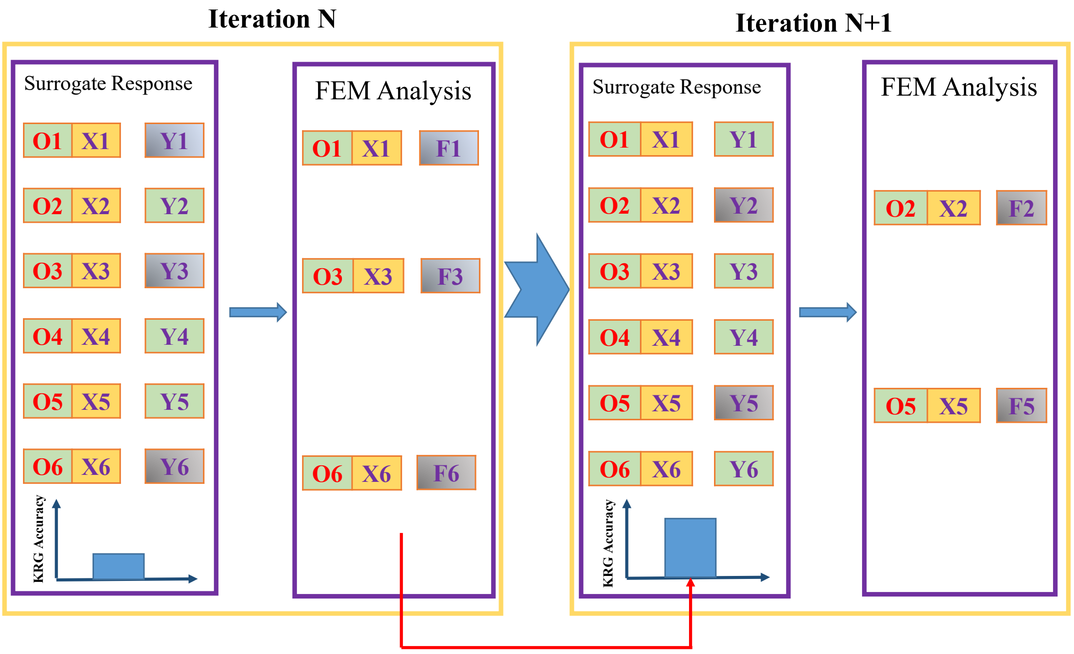

Figure 4.5: Maturation of Kriging Model in every loop.

Figure 4.5 illustrates the schematic maturation of the Kriging function during an optimization process loop. In this schematic, **Y** is the objective value obtained by the surrogate response. While genetic algorithm converges, the differences between individuals in the populations are decreased. It means that the difference among objective values (outputs) and also the Euclidean distance among individuals in the parameters domain (inputs) reduces, hence, the accuracy of the surrogate function improves. This is because of the fact that the number of training samples is the same but the searching domain is smaller in every iteration, therefore, the surrogate model cover a smaller searching space with a higher accuracy.

4.5 Feasibility

The parameters of a problem in an optimization process are restrained to variate between a limited range of values which are defined by various constraints of the problem. These limits are known as nominal boundaries of the problem and are defined according to physical or manufacturing restrictions of the design. Hence, the input vector $\mathbf{X}'$ is limited as,

$$\mathbf{X}^i_{Lower} \leq \mathbf{X}^i \leq \mathbf{X}^i_{Upper} \tag{4.2}$$

However, every combination of input vector selected in this predefined limit does not necessarily provide a real physical geometry. Therefore, this limitation defined by the designer does not reflect the real existing boundary of the working domain. This is due to the fact that every parameter value selection would affect others in a way that the relation in Eq. 4.2 becomes

$$\mathbf{X}^i_L(\mathbf{X}^j) \leq \mathbf{X}^i \leq \mathbf{X}^i_U(\mathbf{X}^j) \tag{4.3}$$

Indeed, the equation 4.3 determines the feasible space of the searching domain. In other words, while working with a parametric model encountering some cases for which the input vector **X** does not provide a physical meaningful geometry is inevitable. In these cases, the geometry is located in a non-feasible space. For an optimizer, the non-feasible space may cause difficulty for the seeker in finding the optimum (this problem is addressed in the following section). The non-feasibility can raise in two circumstances, non-consistency and design constraints. Figure 4.6 illustrates two examples of such non-feasibility. Half of the blade and disc section has been illustrated due to symmetry. The red line is the blade root and the black line is the disc groove. Figure 4.6-a shows a non-feasible sample in which the geometry has no physical meaning and Fig. 4.6-b shows a non-feasible sample where the geometry is now consistent, but a design limit has been surpassed. The design constraint which has been exceeded in this case is the maximum allowable penetration of the dovetail groove into the disk.

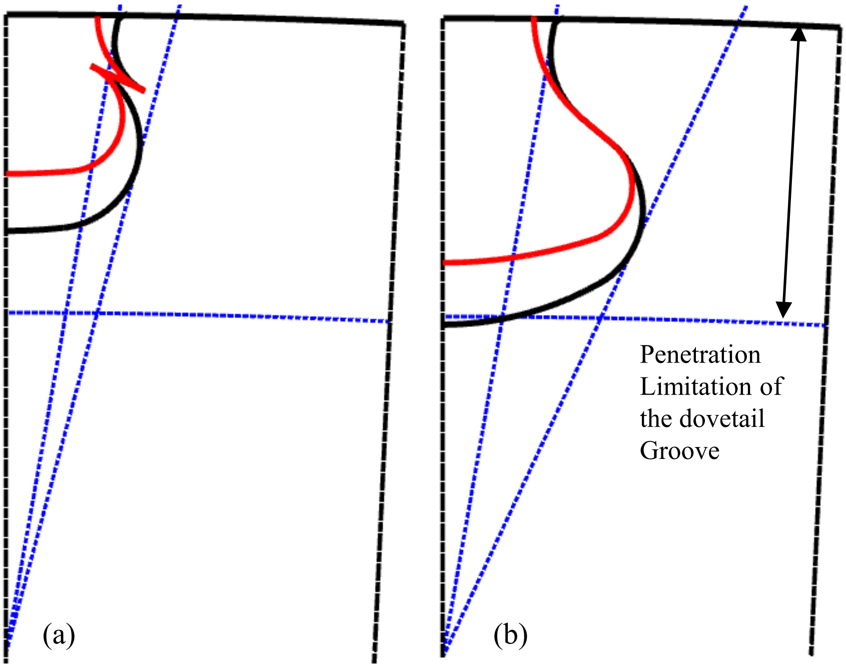

Figure 4.6: Non-Feasible geometry, red line: Blade dovetail, Black line: Disc groove, a) No physical meaning b) Violation of constraints.

4.6 Penalty Allocation

In real applications of optimization, especially in mechanical problems, the function we are dealing with is not always a continuous function and also the function is not a mathematical function. In fact, usually, the response of mechanical analysis is a black box function (B.B.F) in which there are many numerical calculations combined to reach the solution. In these cases, the problem is not only the high computational time needed to reach the optimum but also due to the non-feasibility of some large parts of the domain, the optimizer may not be able to reach the global optimum. There are two techniques proposed by the author described in Appendix F by which the non-continuity of the searching domain is rectified and also by a modification in the mutation process of GA, its capability to find the global optima has been increased in a multi-district domain. As the current problem of the blade and disc attachment lie in one district of feasible space and one non-feasible space, the proposed penalty method has been detailed in this section.

There are different objectives favorable in the case of blade and disc attachment such as minimizing the Equivalent stress, Contact Normal Pressure, Maximum Principal Stress (MPS) over notches, frontal area, Mass or Maximizing the Fatigue life of the components. In order to reduce the computational burden during the optimization it is common to consider some objectives as constraints. For example limiting the input vectors having equivalent stress less than some predefined value or avoiding the life cycle of the components exceeding a predefined value. For considering the fatigue life of the contacting area in the attachment please refer to Appendix G.

While searching through input vectors in a working domain of a parametric model, confronting non-feasibility cannot be avoided. The designers always try to trim the boundaries of parameters to make the working domain as small as possible and consequently decrease the undesirable non-feasible spaces. Although, such trimming may help in convergence, even in the most careful selection of boundaries, there is no guarantee that there would be always a real physical geometry definable for the input vector selected during the search process. In other words, the non-feasible space exists inside the allowable range of parameters which may occur due to mutual interaction of parameters or violating a design constraint. The same issue happens in the case of blade and disc parametric attachment. Because of severe interconnection among different parameters of the design, the working domain is occupied by non-feasible space with a high ratio.

Figure 4.7 embodies the feasible space for a blade root of type fir-tree having three lobs. The cloud of points is used to illustrate the feasible space for four sets of combination of three parameters. It is obvious in this figure that even by adhering to nominal boundaries for every parameter there is a high proportion of non-feasible space in the working domain. Such an issue may raise a problem for the optimizer as there is no value to be allocated to the points selected in these spaces as an objective value. There are some solutions to rectify this problem in the literature [80]. The simplest method among them is to neglect the inputs inside non-feasible space and allocate them an objective value

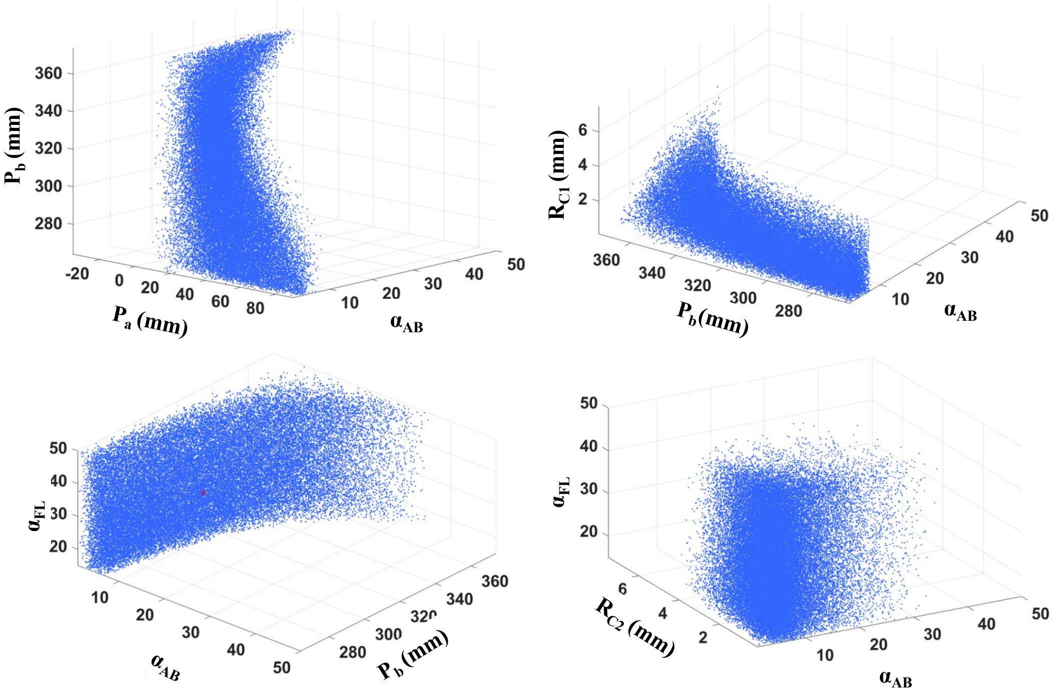

Figure 4.7: Cloud of Feasible space inside the working domain. As the working domain is in a higher dimension than 3D, different illustrations with a different selection of input variable parameters have been shown here (Please refer to Table A.1 for parameters description).

which is considered as the least fit to the optimizer, hence, making the optimizer to filter these points out of its current population. This method is known as the death penalty. However, this method will waste the valuable information of the non-feasible space by just ignoring it. For instance, the death penalty method makes no difference between two input points the optimizer has picked in a non-feasible space even if one is really close to the feasible space and give them the same objective value so that making sure they both will be dropped out in the proceeding of the optimization process.

Such an issue is much bolder while working with higher dimensions of working domain. It means that if the number of variable input parameters is high, a larger working domain would exist, while, due to the interconnection of more parameters (which now their agreement is more conflicting) the feasible space is much smaller, hence, providing a real challenge for the optimizer to fall inside this space. Therefore, when the optimizer with a death penalty method crosses the proximity of the feasible space very closely but does not observe its closure. Subsequently, in a high dimension searching domain, there is always the risk of not finding a feasible solution by the optimizer and the whole process fails.

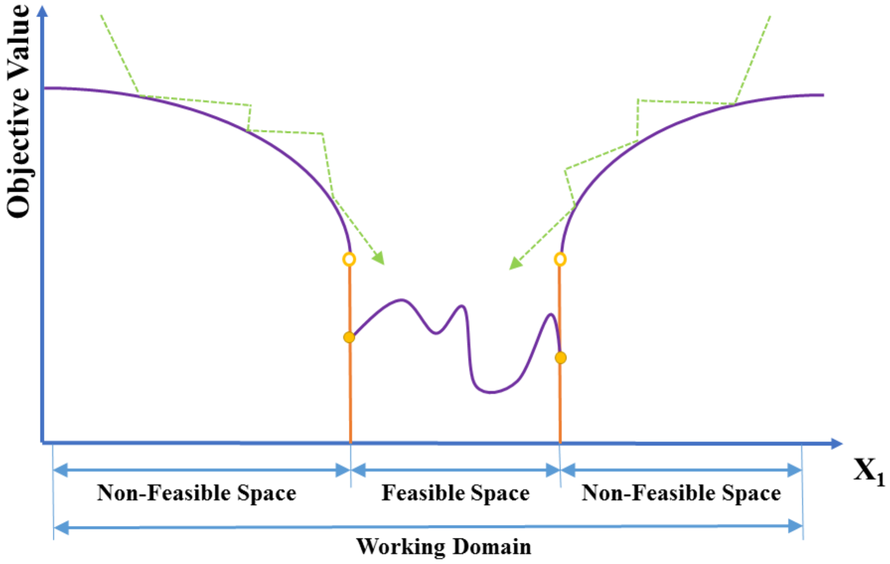

Figure 4.8: The LHS adaptive penalty method.

Alternatively, the method of adaptive penalty provides a more improved fix to this problem by taking the advantage of input vectors even in non-feasible space. In this method, the interested input point is given an objective value of inversely proportional to its Euclidean distance to the feasible boundary. In fact, the objective value is considered more fit by the optimizer as the input point gets more close to the feasible space. Consequently, such an approach forces the seeker to fall into the feasible space (fig. 4.8). However, application of this method requires the careful determination of the feasible boundary even if it does not necessarily have a regular shape.

Applying the death penalty to the response function bring out the chance of trapping the GA into a local optimum. On the other hand, in order to apply the adaptive penalty, there is not a known boundary segregating the feasible and non-feasible spaces. It means that for applying the adaptive penalty which benefits from the Euclidean distance to the nearest boundary firstly the feasible boundary should be known.

Therefore a novel method has been proposed in this study to determine the boundary of the feasible space of the blade and disc attachment parametric model working domain.

In this method, using the LHS method, some uniformly distributed samples are generated inside the nominal boundary, then, using a simple low-cost geometric evaluation, the feasibility of them are examined. This evaluation is quite fast in comparison to the whole process because there is no requirement to perform heavy numerical methods. Hence, the real physical boundary of the feasible space is found by a cloud of points.

Then, by applying the following penalty function which replaces the objective function, an integrated space is provided,

$$\phi_p(\mathbf{X}) = \begin{cases} \phi(\mathbf{X}) & ,\mathbf{X}\text{ feasible.} \\ C_f\left(\sum_{i=1}^{n}\left(\left(\frac{X_i-X_i'}{Ub_i-Lb_i}\right)^2+1\right)\right) & ,\mathbf{X}\text{ not feasible,} \end{cases} \tag{4.4}$$

where $\mathbf{X}'$ is a sample point inside the feasible space and is the nearest point to the questioning point $\mathbf{X}$ (Fig. 4.9) and n is the number of parameters. Coefficient C_f should be high enough to be effective as a penalty value. As a rule of thumb, C_f should be in an order of magnitude higher than the maximum expected value of the objective function.

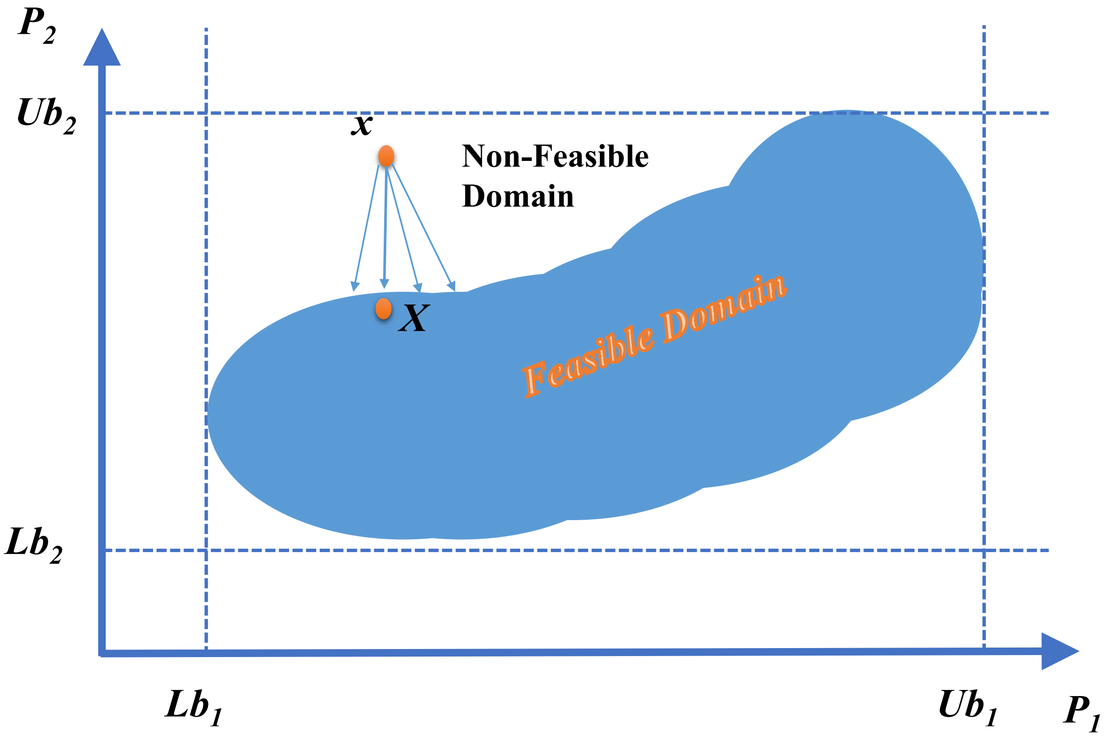

Figure 4.9: Non-feasibility handling by proximity to the boundary of feasible space

The same routine is also applied inside the primary found feasible space to the samples which after FE analysis are found to violate some constraints. Hence, these points are also considered non-feasible points are the same penalty function of (4.4) but with a lower C_f is applied to them.

To examine the effectiveness of the proposed method, a dovetail is optimized applying the proposed adaptive penalty and compared with the results obtained using the death penalty. Figure 4.10 reports the results of the comparison of the death and adaptive penalty method. The objective function values are shown against the number of high fidelity function runs. It is clear from Fig. 4.10 that the GA using the adaptive penalty converged faster and found a better objective value than the one using the death penalty.

The computational time spend to find the feasible space using LHS is compensated with the time saved during the optimization process so there is a gain in the overall procedure.

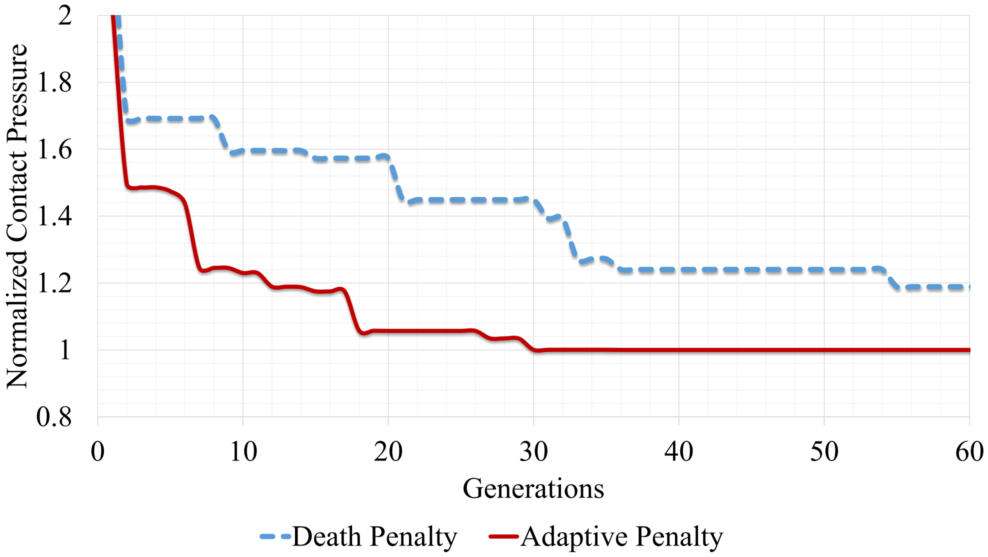

Figure 4.10: Optimization of a dovetail applying death and adaptive penalty functions

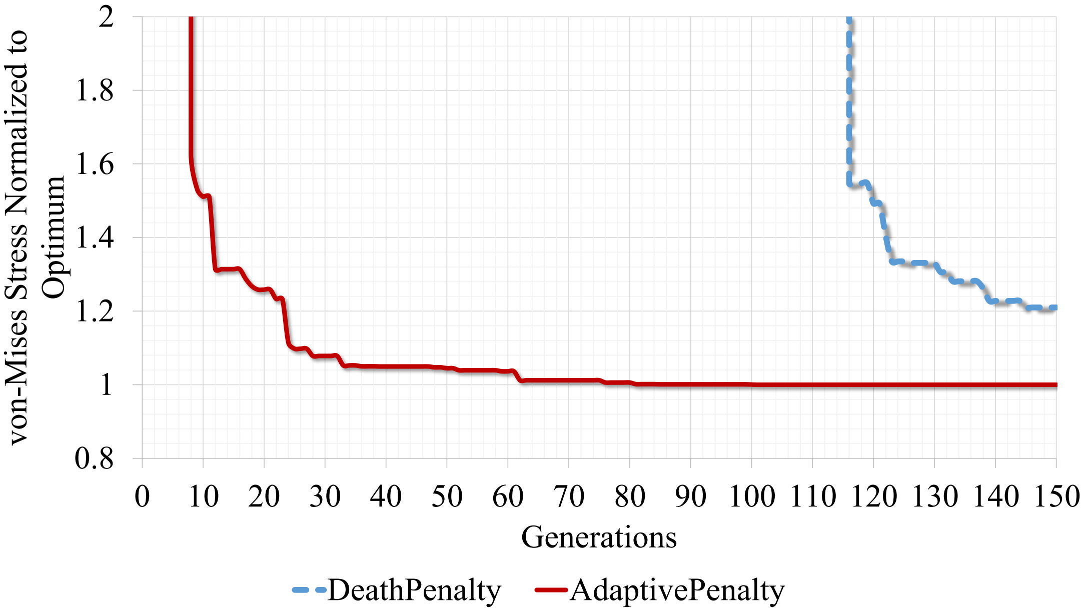

Figure 4.11: Optimization of a 3lob fir-tree applying death and adaptive penalty functions

In another attempt, it has been tried to minimize the von-Mises stress in a 3-lob fir-tree. Both death penalty and adaptive penalty were applied and the results are compared in Fig. 4.11. The fir-tree shape is defined with more parameters that make the interconnection among them more complicated because more parameters should agree to make a physical meaning geometry. This is why the feasible space is smaller and the void spaces grow bigger in this case. Figure 4.11 shows that the adaptive penalty provided better performance even in such more complex domains.

4.7 Conclusion

In this chapter, the optimizer was introduced in addition to the surrogate function used for emulating the response of the FE model (high fidelity model). To evaluate the conformity of the results obtained from the surrogate function with that of high fidelity model, a simple model of a single lob were employed. The model went through an optimization (minimizing the bending deflection) once with the FE model and once with the Kriging model. The results obtained by the Kriging model showed high conformity with that of the FE model, hence making this Meta model able to provide an estimation of the results in a fast calculation effort.

With the aim to benefit from the low-cost response of the Kriging function in addition to the high accuracy of the high fidelity model, an adaptive surrogate model were developed embedded in a GA optimization. Such surrogate function gets mature while the optimization proceeds due to the fact that more training samples are available on every generation. The effectiveness of this method will be discussed in chapter 6.

Later, the feasibility in a searching domain was discussed. Two main sources of non-feasibility were introduced. One is not to have a physical meaning geometry and the other is to violate some predefined constraints.

It was found that the parametric models under current study hold a single district feasible space inside their searching domain, although a modified mutation procedure in the genetic algorithm was introduced and evaluated to rectify the problem of finding a global optimum in case of facing isolated multi-district feasible spaces.

In order to take advantage of the data inside non-feasible space during optimization, an adaptive penalty was applied. As the border of the feasible space was unknown, a Latin Hypercube Sampling method was applied to the searching domain to determine the feasible and non-feasible spaces. The proposed method rectify also the problem of difficulty in finding the feasible space and possible termination of the solution process.

The proposed method was applied to two blade and disc attachment parametric models of dovetail and fir-tree in order to evaluate its effectiveness. It was found that this method is even more effective in a higher dimension complex searching domain.

Chapter 5

Contact Topology Assessment

The contact pressure profile is very sensitive to the topology of the contact. In this chapter different topologies of the contact for a dovetail under similar conditions is examined and different contact criteria are compared. Four different topologies for the dovetail contact is assessed. The punch test is also applied to provide a benchmark to study different parameters of the contact although the main purpose is to have a minimum contact peak stress in the attachment. Hence, after applying every contact type, an optimization was conducted under a very limited range of parameters variation to find the best shape of its kind in terms of contact pressure peak.

5.1 Single-Curve (Type-I)

A dovetail of which the contact is composed of a straight line between two single curves is named type-I in the current study. An already optimized shape of the dovetail in terms of contact pressure and notch maximum principal stress has been selected as the sample to this study. Beforehand, a punch against a flat was set up as a benchmark ([24], [93], [78] and [18]). To be consistent with the dovetail geometry, an equivalent radius for the punch was determined using the fillet radius of the blade R_b and of the disk R_d. The equivalent radius R_{eq} was ([45]),

$$\frac{1}{R_{eq}} = \frac{1}{R_d} - \frac{1}{R_b} \tag{5.1}$$

Figure 5.1 sketches the dovetail and its equivalent punch test. Figure 5.2 compares the contact stress distributions of the dovetail with the benchmark. As seen, there is a high conformity in the peak normal contact pressure between the dovetail and the punch but the median part of the contact showed different stress profile due to the fact that in the dovetail the component does not just undergo normal contact but also bending exists.

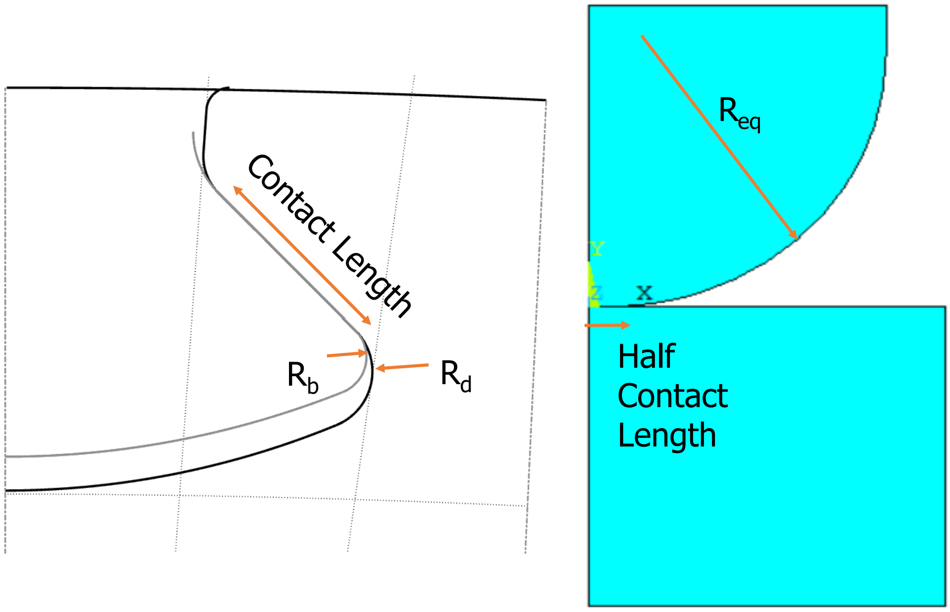

Figure 5.1: The Equivalent Punch Test for the dovetail with Type-I curve

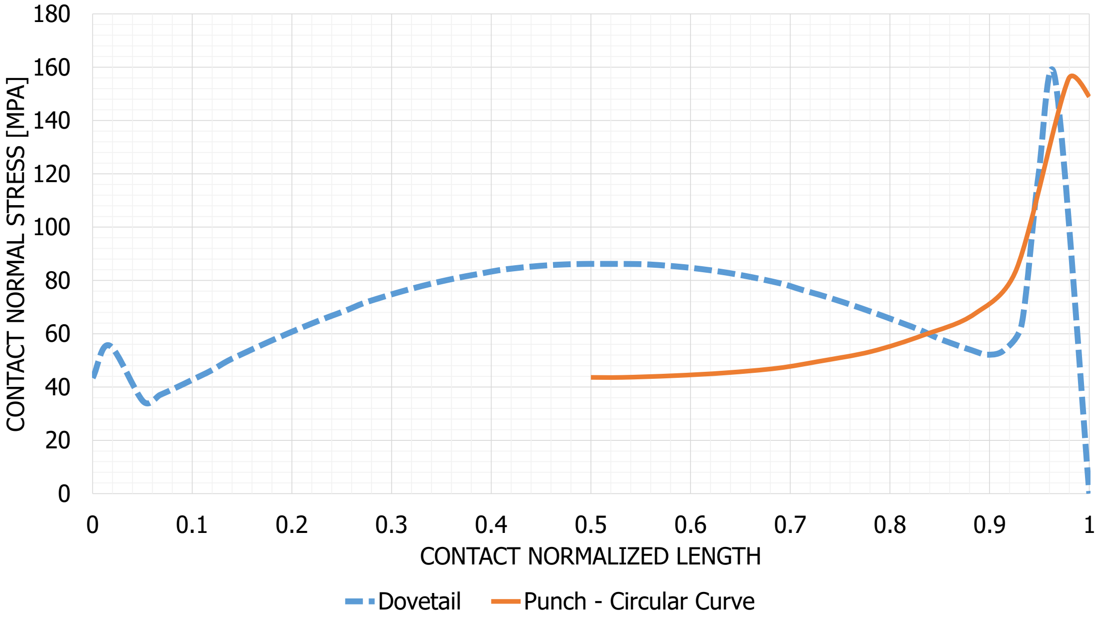

Figure 5.2: Dovetail contact (Type-I) and its equivalent punch test

5.2 Multi-Curve (Type-II)

The second contact shape benefits from more curvatures instead of a single radius curve for notches. The curve near the contact has the highest radius and as getting far from the contact the radius decreases. This method helps to save the space while maintaining a smooth transition from line to curve in a contact edge (Fig. 5.3). In the current study, two curvatures of different radius were used. The radius and angles of the first and second curves are R_1, α_1 and R_2, α_2 respectively.

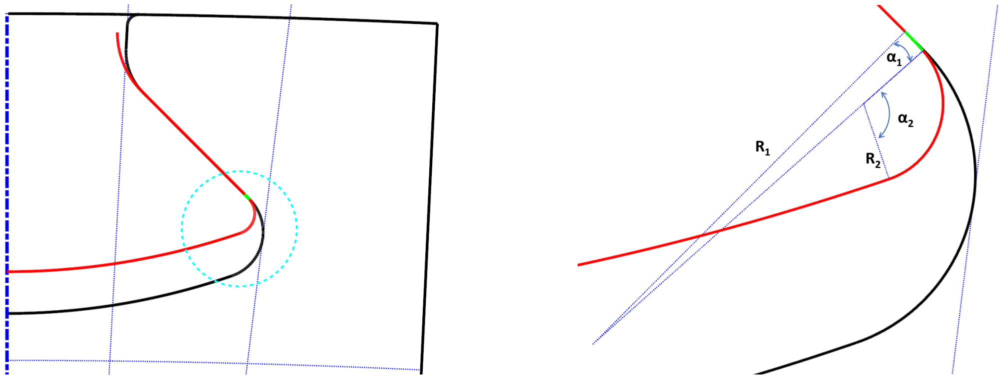

(a) Symmetrical sketch of a dovetail. (b) Close view of the lower contact edge.

Figure 5.3: Sketch of a Dovetail having Type-II contact shape.

5.3 Polynomial-Curve (Type-III)

In the contact profiles Type-I and Type-II, the transition of the straight line to the arc with a constant radius occurs instantly. In fact, at the two sides of the contact, the straight line connects to an arc with an already defined radius (Type-I) and then continues with another arc with another smaller radius in Type-II. In the current study, a new profile was introduced, Type-III, in which the arc with a constant radius was substituted with a third order polynomial. This polynomial was designed in such a way that its curvature is continuously changing from zero (the same curvature of the straight line) to a predefined value. This profile, denoted as polynomial-curve, provides a better transition from the straight line of the contact comparing to two previous topologies. The polynomial-curve (Type-III) and the circular curve (Type-I) are compared in Fig. 5.4.

In order to evaluate the effect of the polynomial curve on the state of stress, a punch test was used as a benchmark. At first, a polynomial curve with the same ending point (full height) of Type-I was tested. In this condition, Type-III shows a reduction of the peak stress of 40%, see Fig. 5.6. Further, two other ending points were evaluated, one with half of the full height and the other with 20% of the full height. These profiles showed a higher reduction of the peak stress about 48 % which compared to the first

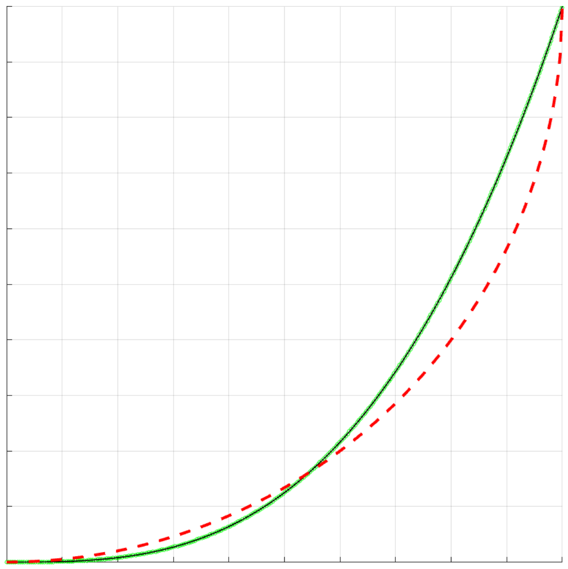

Figure 5.4: Circular (red dashed)(Type-I) vs Polynomial (green shined black)(Type-III) curve

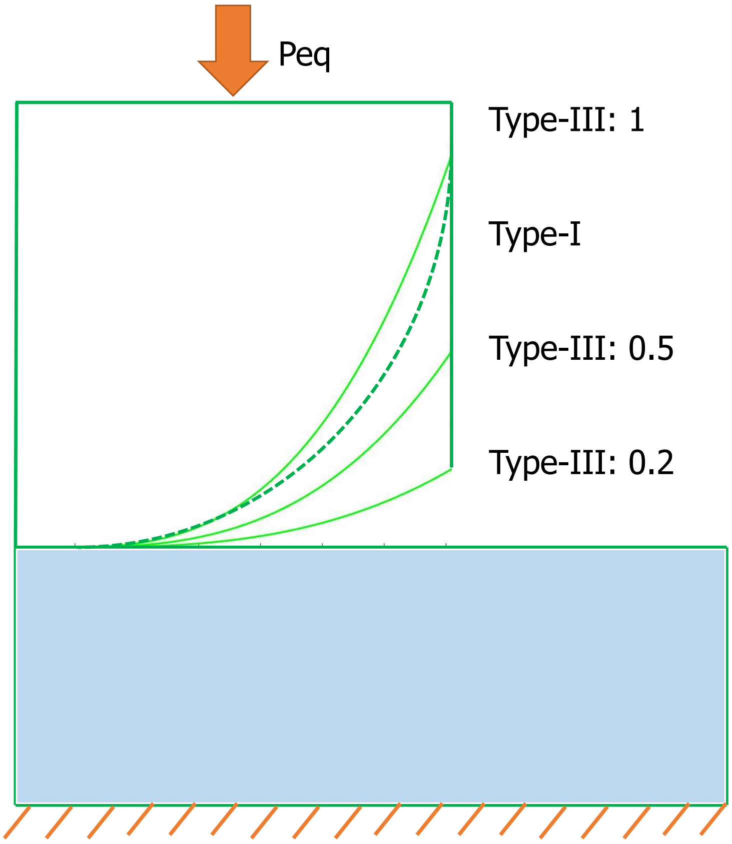

Figure 5.5: Punch test comparing a single curve (Type-I) with a polynomial curve (Type-III) of different ending points.

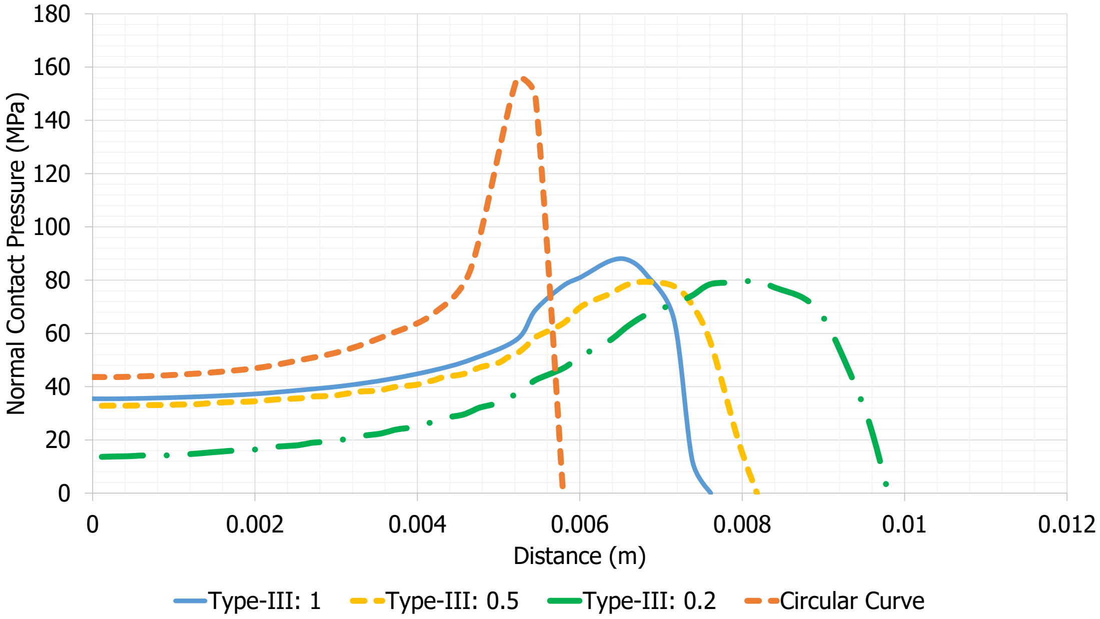

Figure 5.6: Normal Contact Pressure for different Punch Profiles.

ending point is negligible. The polynomial curve with different ending points in comparison with the circular curve is shown in Fig. 5.5. Correspondingly, the normal pressure for them is graphed in fig. 5.6. As seen the peak normal contact stress is not affected by the ending point of the contact edge curve.

The polynomial curve (Type-III) was applied on the attachment in the blade dovetail in a way that all other parameters were kept constant and the only variable parameter was the angle in which the polynomial curve joins the constant curve of the dovetail fillet (Fig. 5.7). The angle in which the polynomial curve is joining the constant curve of the contact edge is illustrated in Fig. 5.8. In fact, lower α leads to a less frontal area of the dovetail and save in total weight of the attachment.

It was found that by applying different ending point to the Type-III profile using a different angle of curve ending did not provide a significant reduction on the contact peak pressure (Fig. 5.9). It means that the contact pressure profile is insensitive to the joining position of the polynomial curve.

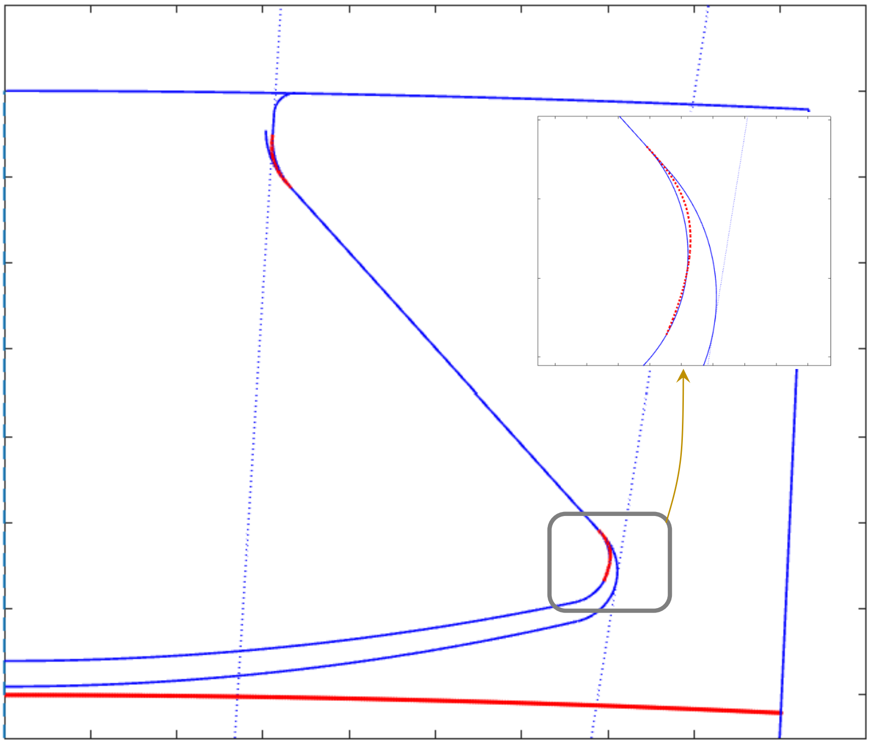

Figure 5.7: Dovetail with polynomial curvature (Type-III).

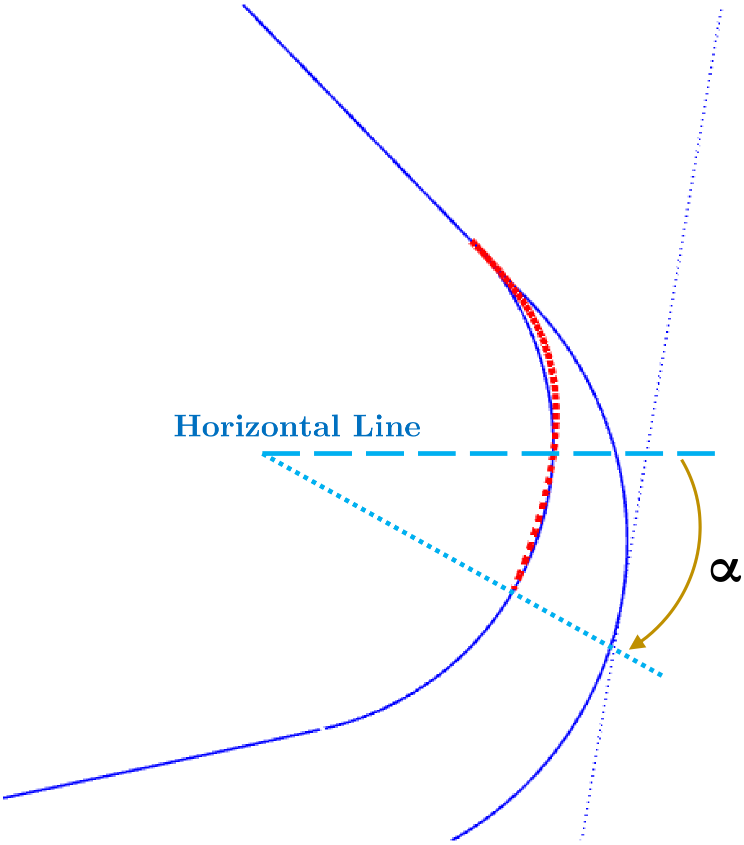

Figure 5.8: The position of the polynomial curve joins the simple curve, α.

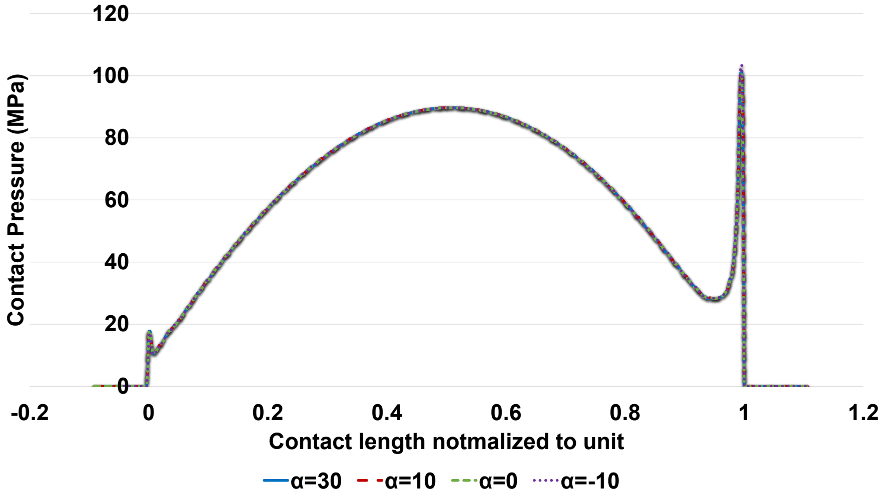

Figure 5.9: contact pressure of polynomial curve (Type-III) joint with different α

5.4 Crown type (Type-IV)

The last topology (Type-IV) applied was the one introduced by [92]. In this topology, instead of a straight line for the contact, a high radius curvature is applied. Figure 5.10 compares three different topologies of the contact for a dovetail.

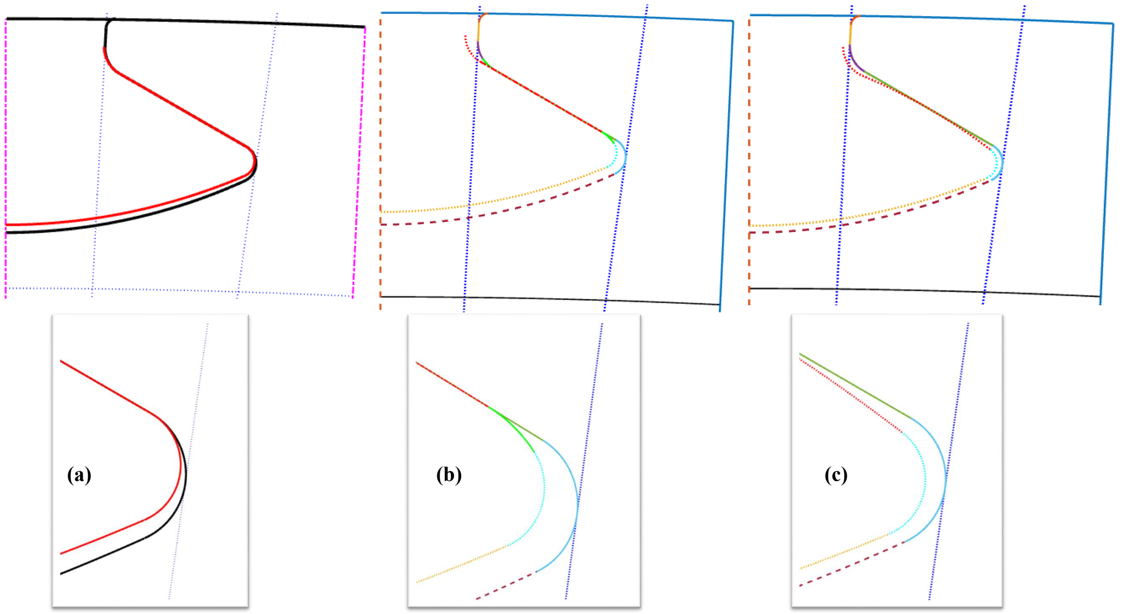

Figure 5.10: Three different types of dovetail topology; (a): Type I, (b): Type II and (c): Type IV

5.5 Contact Criteria Assessment

Applying the four different contact shapes on the optimum geometry leads to different profile of contact pressure on the mating surfaces. The results are compared in Fig. 5.11. The contact stresses were normalized to the stress peak in Type-I. As seen, the crown type (Type-IV) attachment provides the lowest contact normal pressure peak. Due to the fact that some parameters of the dovetail model had to be changed to adopt the corresponding contact type, the resultant normal force would not be the same for all four Types of the dovetail although comparison can still be made as all types undergo optimization again but with a reduced searching domain.

Also, some other critical measures in the dovetail evaluation were obtained by the FEM and compared in Fig. 5.12. The first maximum principal stress (MPS) for both blade and disc notches was obtained for all four types of topology. Also, von-Mises stress all over the blade and disc was compared. Moreover, the relative displacement

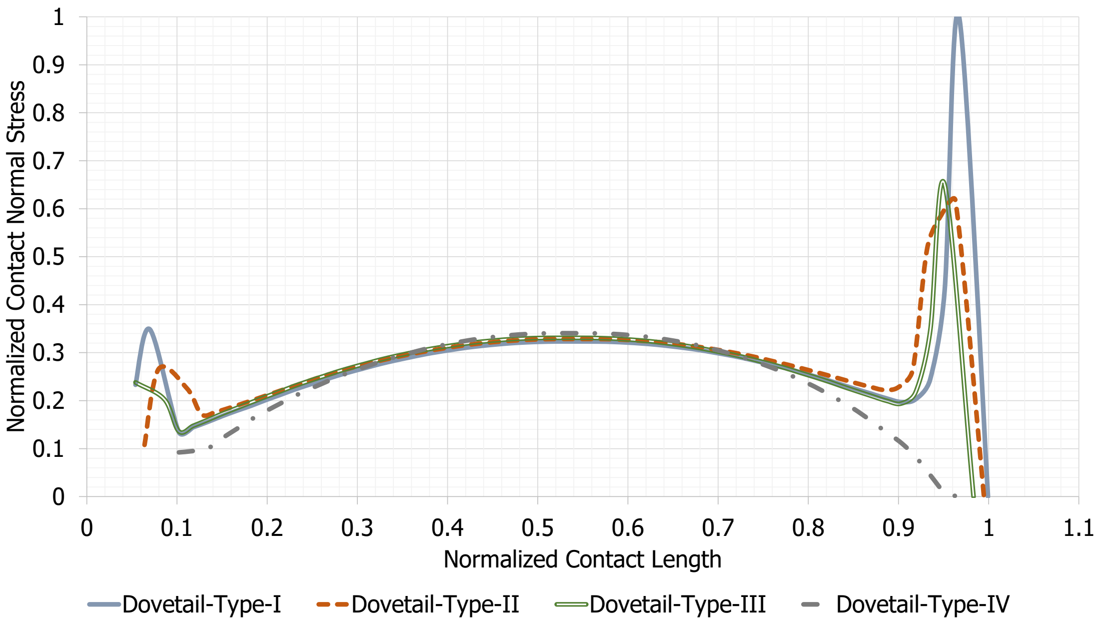

Figure 5.11: Normalized contact normal stress for dovetail with different contact shapes

of the attachment as an important element in fretting fatigue was compared for all four types of topology. The crown type demonstrated the least relative displacement among others. The polynomial type showed just an improvement in the blade notch MPS and all other indexes remained the same as for the original single curve type. The Multi-curve type of the attachment (Type-II) provided lower MPS in the disc and the von-Mises stress compared to other types. The cause is due to the fact that in this type of attachment the designer can use a very large radius in the curvature close to the attachment while ending to a very sharp curve to save the space in areas which contact is less effective but other parameters like MPS and von-Mises are dominant. On the other hand, due to the relative shift of contact mating surfaces, the effective equivalent force of the contact pressure has moved a little farther from the root of the blade and introduces more bending stress on the upper notch (blade) comparing to that of other types of topology.

Also, the multi-curve attachment (Type-II) had less maximum relative displacement in the contact area comparing to Type-III and Type-I curve due to the fact that the contact area has been reduced and the attachment is more compressed permitting less relative displacement.

The crown type topology (Type-IV) showed the minimum blade MPS and the minimum relative displacement among the compared geometries. Nevertheless, this topology shows the maximum MPS and Equivalent stress in the disc notch.

As the shape of the dovetail is designed according to the working condition thus the optimum may be very sensitive to working condition changes. A variation to the RPM has been carried out and the effect of rotational speed to the design criteria of the four

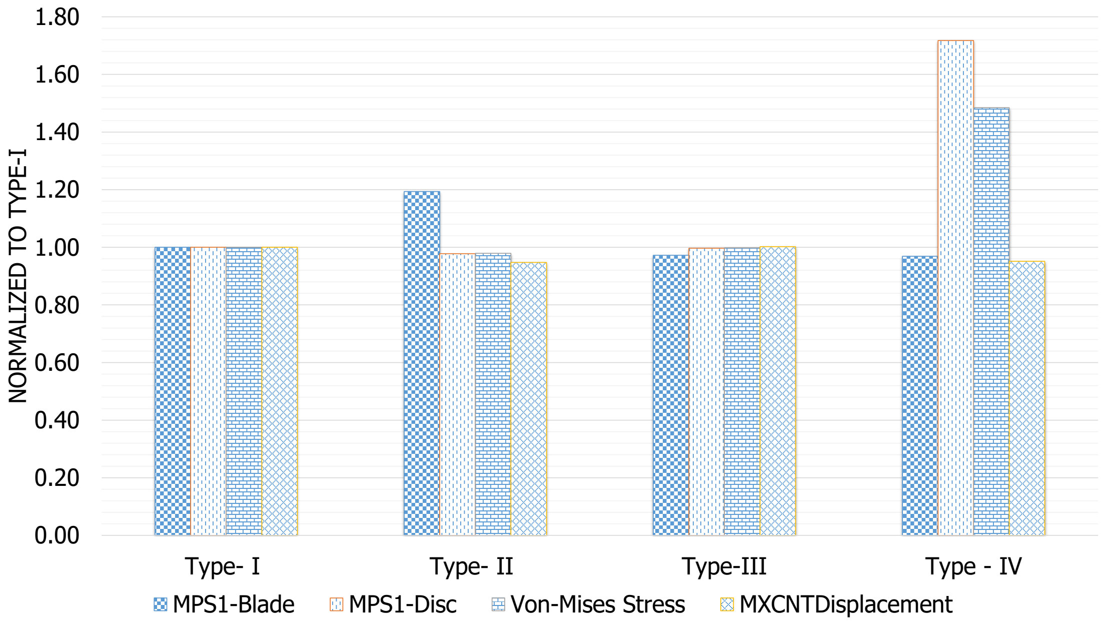

Figure 5.12: Comparing different criteria for different contact shapes of the dovetail type attachments has been evaluated. The evaluation has been carried out in three speeds of 191, 300 and 382 radians per second.

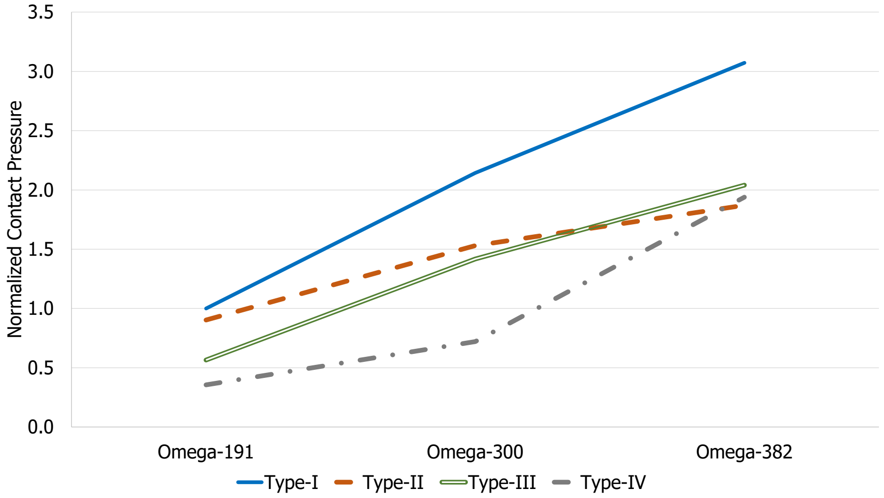

Figure 5.13: Normalized max Contact Pressure for different attachments in different rotational speed

As seen in Fig. 5.13, the crown type attachment (Type-IV) tends to deviate from its privilege manner in higher rotational speed due to the fact that the curvature for the contact is not concave enough and the contact will extend beyond the length it is designed

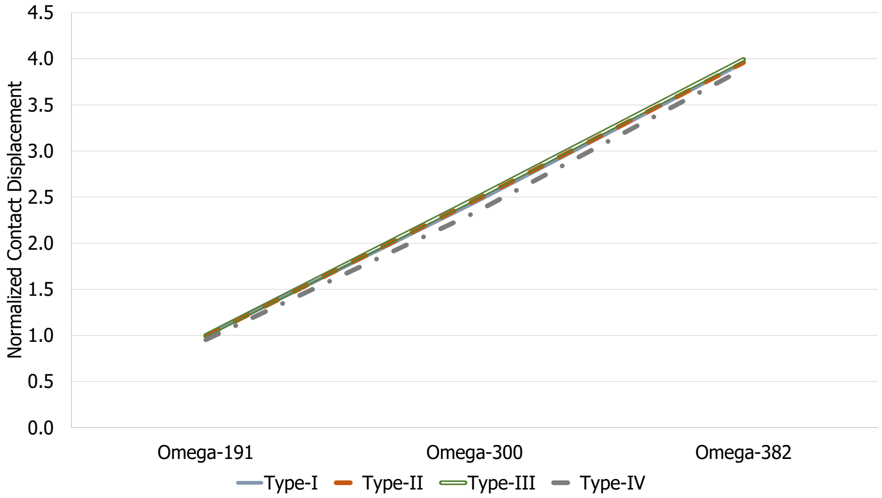

Figure 5.14: Normalized Contact slide for different attachments in different rotational speed

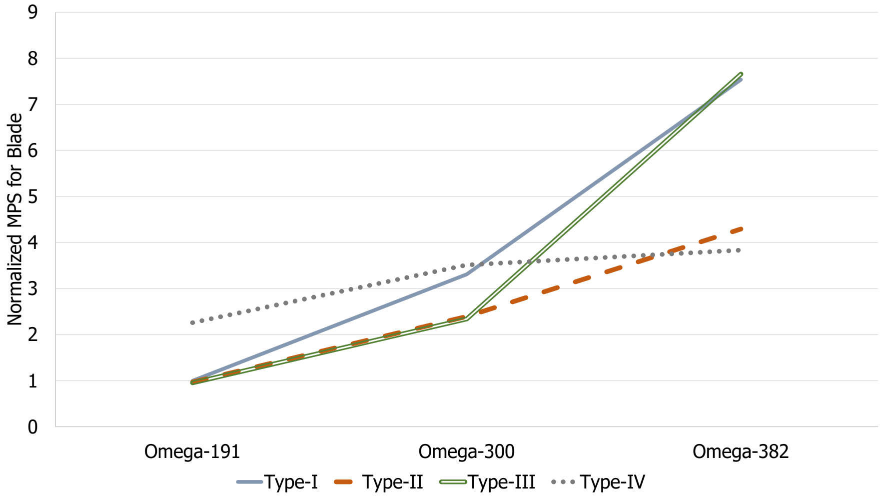

Figure 5.15: Normalized Maximum first Principal Stress in blade root for different attachments in different rotational speed

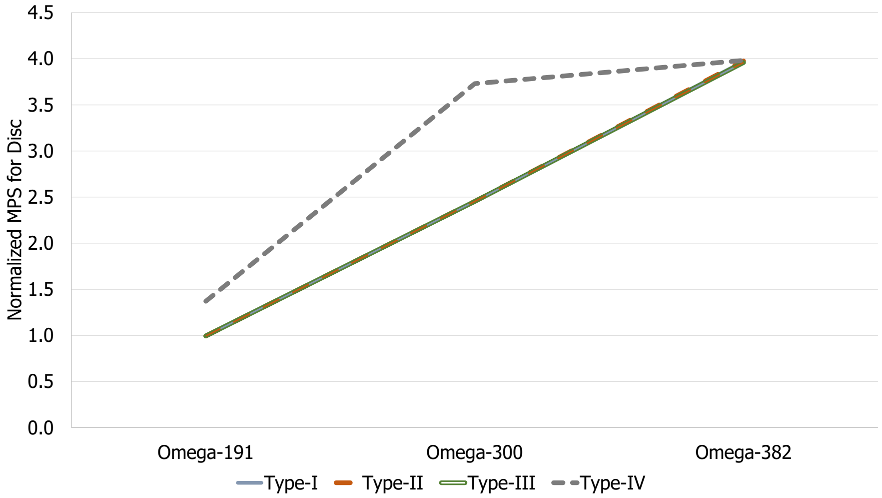

Figure 5.16: Normalized Maximum first Principal Stress in Disc for different attachments in different rotational speed

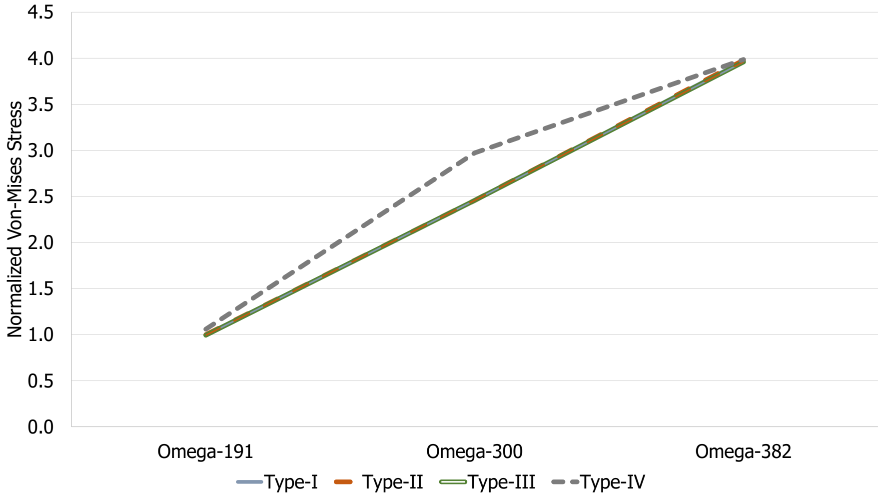

Figure 5.17: Normalized von-Mises Stress for different attachments in different rotational speed

for. Hence, the contact normal stress follows the same profile of the other three types of attachment in which a peak in the corner of contact shows up. On the other hand, this type of attachment although engage less contact area at lower RPM but the peak is still quite less compared to the other three types. Therefore, this benefit makes the designer possible to consider an over speed loading and design the curvature radius for that load and the contact will still provide a smooth profile for contact normal stress without any high sharp peak.

5.6 Conclusion

The contact normal pressure is highly sensitive to the topology of the contact in the attachment. In order to evaluate such feature, four different topologies named Type-I to IV were studied. Also, the punch test was applied as a benchmark for this study. It was found that by introducing a gradient change in the curvature of the contact edges, less peak stress will arise, although this trend has a limitation as by highly smoother gradient no improvement happens (i.e. in its extreme case, which was Type-III, no significant improvement was found compared to Type-II).

Moreover, maximum principal stress in the blade component as well as disc component, von-Mises stress of the attachment and maximum relative displacement of contacting mates were compared among the four types of topology in different rotational speed. Generally, the type-II was found to show better performance in comparison to other types of topology.

Chapter 6

Results and Discussion

6.1 Analytical Approach - Dovetail

In the current section, the aim is to compare the optimization using the FEM analysis with the one with the analytical approach on the basis of the minimum peak contact pressure. Using the formulation by Ciavarella et al. [24] described in subsection (3.1) the peak normal contact pressure can be estimated analytically. Therefore, to evaluate the possibility of this approach in finding the optimum dovetail shape which has a minimum normal stress in contact, an optimization using genetic algorithm was performed with analytical and FEM approach. In other words, two different runs with different objective functions were performed.

To eliminate other factors affecting the comparison and as the analytical approach is not able to calculate the stress profile on the components, the maximum stress on the notches are controlled by limiting the components neck length. In this case, the neck for the blade is limited to 3 mm and for the disc, it is 5 mm. Also, there was no requirement of having higher stress on the blade relative to the disc. In the analytical approach, the centrifugal force is considered due to the blade mass. For the FE approach in addition to applying a uniform pressure representing the centrifugal force of the blade to its neck, the density of the blade root was also defined. It means that the blade root mass is also accounted for in this approach. In both approaches, the symmetry is applied. The parametric model of the dovetail with a simple contact profile (i.e. one straight line embedded between two single curves) and having a curved groove shape was used for this assessment. In this case, the input vector for the dovetail parametric model is,

$$\text{Input Vector}^T = [\alpha_A, \alpha_B, R_{C1}, R_{C2}, \alpha_{FL}, R_{CA}, R_{C1b}, R_{C2b}]$$

In order to have less peak stress in the contact area, it is recommended to set the curvature of the blade very close to the curvature of the disc groove (see Eq. 5.1) but practically it is not possible due to installation and manufacturing reasons. Also, if one may not consider enough gap between the lower curve of the blade root and the disc groove, the deflection of the lob may affect the stress state in the groove (as lower surfaces may contact after applying the load). Hence, the following constraints were applied to maintain a minimum tolerance (which is arbitrarily selected for the current study, although, one may apply another rule for the minimum tolerance according to the respected manufacturing practices),

$$\begin{aligned} 1.1\times R_{C1}-R_{C1b} &\leq 0 \\ -1\times R_{C2}+1.1\times R_{C2b} &\leq 0 \end{aligned}$$

which in matrix notation is,

$$\begin{bmatrix} 0 & 0 & 1.1 & 0 & 0 & 0 & -1 & 0 \\ 0 & 0 & -1 & 0 & 0 & 0 & 0 & 1.1 \end{bmatrix} \times \begin{bmatrix} \alpha_A \\ \alpha_B \\ R_{C1} \\ R_{C2} \\ \alpha_{FL} \\ R_{CA} \\ R_{C1b} \\ R_{C2b} \end{bmatrix} \leq 0$$

This constraint is to guarantee enough separation in the notches (i.e. the inner curve in a notch should be less in radius comparing the outer curve). Also, the lower and upper bounds were assigned as,

$$\begin{aligned} \text{Lower Bound} &= [10,20,5,5,10,4,5,5] \\ \text{Upper Bound} &= [90,100,40,30,60,60,40,40] \end{aligned}$$

The bounds were decided according to the extreme possible range for every parameter. As the optimization is performed on the basis of integer variation of parameters and due to having higher accuracy the parameters $\alpha_A, \alpha_B, R_{C1}, R_{C2}, R_{C1b}$ and R_{C2b} were considered 10 times the original values which were divided by 10 after the optimizer selects the current vector of inputs (before generating the geometry), so, these variables had the increments of 0.1 of unit. On the other hand, as the curvature of the groove, R_{CA}, was less sensitive (its value was already large), its increment was considered 10 times of unit. Moreover, the variable parameter α_{FL} had an increment of the unit. The objective for both optimization runs was the contact Pressure peak value. The optimum geometries found by the two methods are illustrated in Figure 6.1. The table of results comparison for the optimization by the two methods is in Table 6.1.

Figure 6.2 compares the contact pressure profile of the two optima found. As seen the maximum contact pressure for the analytical optimum is much higher in comparison with the FEM optimum. On the other hand, the profile of contact pressure for the analytical case is more like the Herzian contact shape but the contact pressure profile for the FEM optimum has a peak in the lower edge of the contact. In case of having a singularity in the contact edges, the peak stress is dependent on the mesh sizing. In the

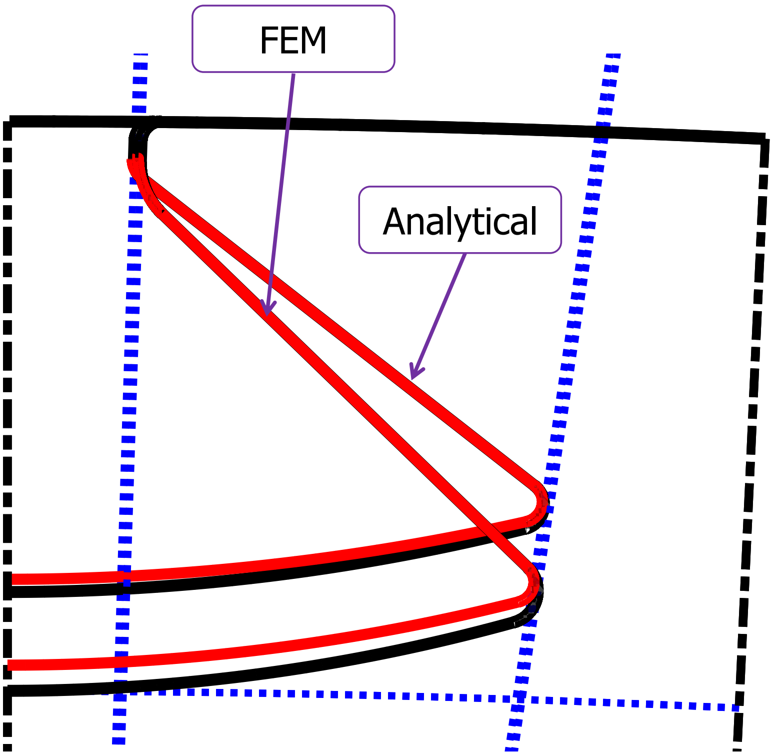

Figure 6.1: the analytical optimum vs. FEM optimum geometry.

Table 6.1: The comparison of the FEM results for analytical optimum vs FEM optimum geometry

	Analytical	FEM
Max First Principal Stress [Pa]	0.857e9	0.8e9
Max Equivalent stress [Pa]	0.761e9	0.726e9
Max Contact Pressure [Pa]	0.119e9	0.098e9
Max Contact Relative displacement [m]	0.493e-4	0.593e-4

optimization process it is not recommended to apply very fine mesh due to high computational costs. Therefore, as a post process to the optimization, it is suggested to evaluate the geometry obtained with finer mesh. After applying a finer mesh to both geometries, the peak for the FEM optima showed higher value while the increase for the Analytical optimum geometry was negligible. Figure 6.3 compares the contact pressure profile of

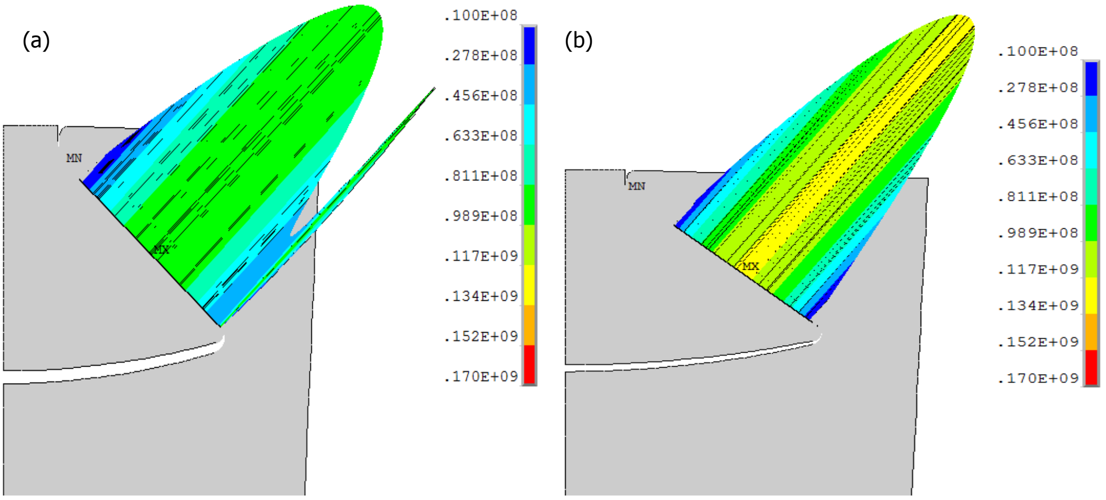

Figure 6.2: The Contact pressure profile for a) FEM Optima, b) Analytical Optima.

the two optimum found. Table 6.2 compares the results after applying a finer mesh to both geometries.

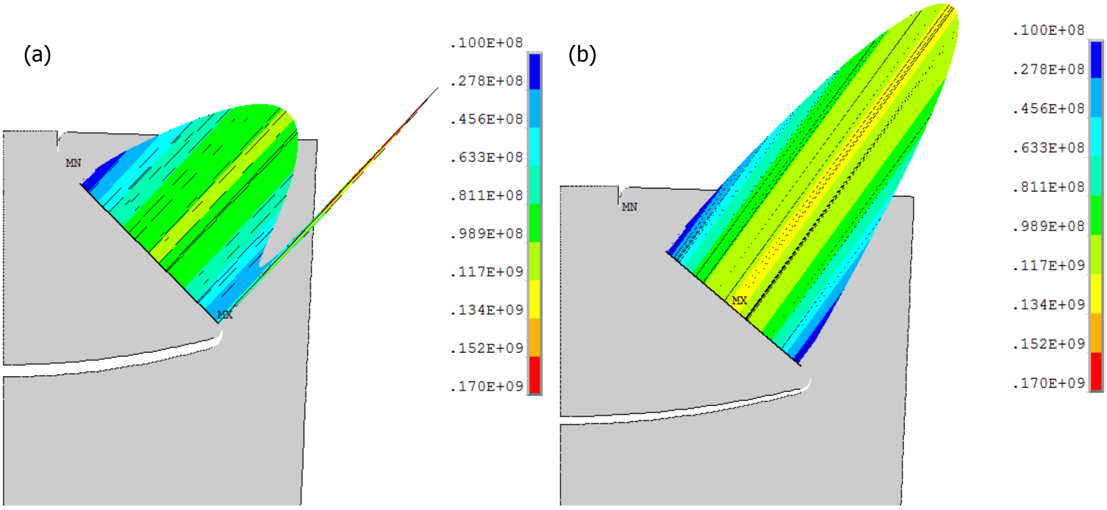

Figure 6.3: Applying a finer mesh for a) FEM Optima, b) Analytical Optima.

Table 6.2: The comparison of the FEM results after applying a finer mesh for analytical optimum vs FEM optimum geometry

	Analytical	FEM
Max First Principal Stress [Pa]	0.85e9	0.813e9
Max Equivalent stress [Pa]	0.755e9	0.722e9
Max Contact Pressure [Pa]	0.118e9	0.162e9
Max Contact Relative displacement [m]	0.471e-4	0.593e-4

6.2 FEM Approach - Dovetail Optimization Using Co-Kriging GA

In this section, a simple 2D dovetail is modeled in parametric terms then optimized for von-Mises equivalent stress with the two Objective functions of the FE method and Co-Kriging surrogate model.

6.2.1 Attachment Description

The dovetail geometry tackled is a modified and parameterized version of an existing dovetail blade root consisting of single curves and straight lines. As the blade and disc have common contacting surfaces some parts of the geometry is the same for both, while the rest are derived according to the variable parameters in addition to meet the constraints. The parametric geometry can be derived by 11 variable parameters and 4 constants described in the Table (6.3). The variable parameters are those values which are manipulated in order to obtain the optimum shape. The constants are the values already defined by the limitation of manufacturing and also the constraints of the nature of the problem such as the constraints extracted from the fluid dynamic analysis. A slice section of the disc and blade is selected and due to the symmetry nature of the problem, half of this section is modeled for analysis. The boundary condition for the model is the symmetry boundary condition for the section lines which prevent displacement in the angular direction (Fig. 6.4). The centrifugal body loading is applied to the whole model by introducing rotational speed ω and defining the density of the material used. Also, having the weight of the blade, its center of mass radial distance and rotational speed provide us the centrifugal load applied to the blade root. As is illustrated in figure 6.4, this force is applied by a uniform pressure proportional to the force and the section area in which blade will attach to the root.

The parametric model uses 11 values to be constructed. There are two guiding lines a and b which determine the share of the tooth on the blade and disc attachment (see Fig.6.4). The curvatures C1 and C2 are two main curvatures on the disc and are tangent to the guiding lines. By changing the radial location of point P_a and P_b and also by changing the corresponding angles, the location of the curvatures changes. The curvature C2b for the blade is considered as one millimeter less in radius comparing to C2 of the disc so it is not an independent variable. The parameterization of the design means that different sets of parameters provide different shapes for the blade and disc joint. Every parameter has a range of variations and certainly, the space of variables contains a feasible and a non-feasible domain as some sets of parameters may result in unacceptable shape. After generating the parametric model an in-house code evaluates the feasibility of the model according to mathematical and logical relationships because every shape generated may not have a physical existence or may violate some predefined constraints (see Sec. 4.5 for more about feasibility).

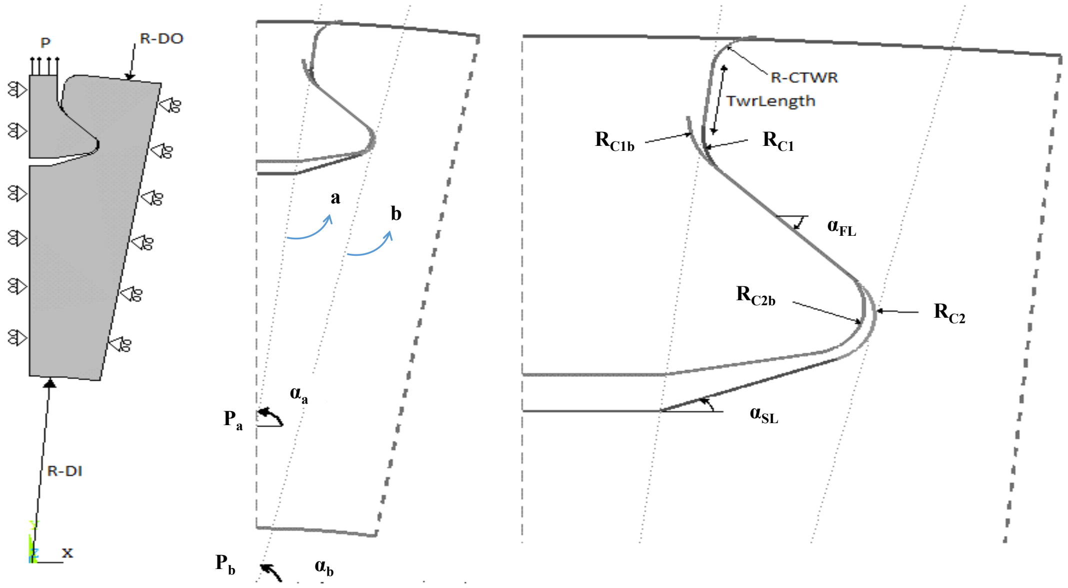

Figure 6.4: Boundary conditions and detailed schematics of the parameters of a dovetail.

6.2.2 Finite element model

Although the loading may not be uniform along disc thickness in a disc and blade attachment, still it is possible to consider the attachment as a 2D problem due to the fact that the geometry is the same in the axial direction (along the skew line) but with different loading [98]. Hence, for simplicity, the FE analysis was performed in 2D plane strain. A high order, 2D, 8-node element having large deflection capability was used. As total

Table 6.3: The parameters and variables of the blade and disc attachment

Parameter	Description	Type	Lower : Upper Bound
y_A	Radial distance of the origin of the first guidance line to center of the disc	Variable Parameter	-20:+80 [mm]
α_A	Angle of the first guidance line	Variable Parameter	60:88 [degree]
y_B	Radial distance of the origin of the second guidance line to center of the disc.	Variable Parameter	-20:+80 [mm]
α_B	Angle of the second guidance line	Variable Parameter	60:88 [degree]
R_{C1}	Radius of the upper fillet on disc	Variable Parameter	1:10 [mm]
R_{C2}	Radius of the bottom fillet on disc and blade	Variable Parameter	1:10 [mm]
α_{FL}	Contact tilt angle (positive)	Variable Parameter	5:70 [degree]
α_{SL}	Bottom line on disc angle (positive)	Variable Parameter	15:70 [degree]
R_{CTWR}	Radius of the upper fillet	Variable Parameter	1:10 [mm]
$TwrLength$	Length of the upper part of the disc	Variable Parameter	1:5 [mm]
R_{C1b}	Radius of the blade neck fillet	Variable Parameter	1.1:20 [mm]
n_{blades}	Total number of blades	Constants	68
R_{DO}	External radius of the disc	Constants	404 [mm]
R_{DI}	Internal Radius of the disc	Constants	216 [mm]
ω	Angular Velocity	Constants	3646 [RPM]
M	Mass of the blade	Constants	0.7 [kg]
C_f	Coefficient of Friction	Constants	0.3
E	Module of Elasticity	Constants	2.020e11 [N/m^2]
ν	Poisson Ratio	Constants	0.3
ρ	Density	Constants	8220 [kg/m^3]
F_c	Centrifugal Load	Constants	14113 [N]

process is automatic, the element size should be defined before the process startup. It is known that the mesh convergence in an FE analysis containing contact is very difficult. It is common to simplify the contact with a punch test. So, the mesh convergence has been done on a simplified equivalent punch test. The contact length and loads from the non-optimum case were applied to the equivalent punch test. Having the radius for blade and disc, the equivalent radius for the punch test was calculated as,

$$\frac{1}{R_{eq}} = \frac{1}{R_d} - \frac{1}{R_b}$$

where R_{eq} is the equivalent radius and R_d is the radius of the top fillet on the disc and R_b is the radius of the fillet of the blade neck area. Figure 6.5 illustrates the schematics of the equivalent punch test. Figure 6.6 compares the normal contact stress with analytical analysis and also FE analysis with four different elements sizes of 0.5, 0.4, 0.1 and 0.05 [mm]. Figure 6.7 compares different element sizes for arresting the peak stress in the contact area. Figure 6.8 plots the variation in peak normal stress in the contact area with different element sizing. The mesh size of 0.1 [mm] was taken for all the optimization process (figure 6.9).

Although in the current study a mesh convergence test has been applied for mesh size selection, it is not an obligation. Because, in the optimization, the aim is to do the comparison among different shapes of attachment and the exact values are not required. It means that if the error of the non converged mesh size is the same for every shape under evaluation, it is possible to do the comparison. Moreover, the same mesh size in the contact area may provide the same error rate, especially when the shapes under evaluation are near convergence in the optimization and the variation in input parameters are not significant.

6.2.3 Optimization method, Boundary conditions and Constraints

For optimizing the dovetail shape for the case under study in this section a genetic algorithm embedded by a Kriging function described in section 4.4 was used. The objective to this optimization was the equivalent von-Mises stress of the whole components. The symmetric boundary conditions were applied to the parametric model of the dovetail and the corresponding disc section as illustrated in fig. 6.4.

6.2.4 Results and discussion

For comparison reasons, a non-optimum geometry was selected and stress analyzed with the same boundaries and loadings conditions. Figure 6.10 compares a non-optimum shape and the GA optimum shape. As seen, the optimum shape digs more radial distance into the disc but it cannot progress extensively due to the fact that centrifugal force burden stress on the disc and having a large cavity of the blade root in the disc makes the disc powerless in tolerating the load.

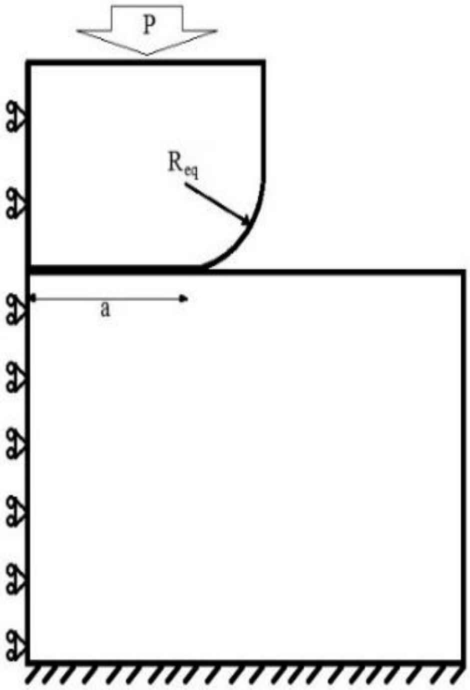

Figure 6.5: Schematics of the equivalent punch test.

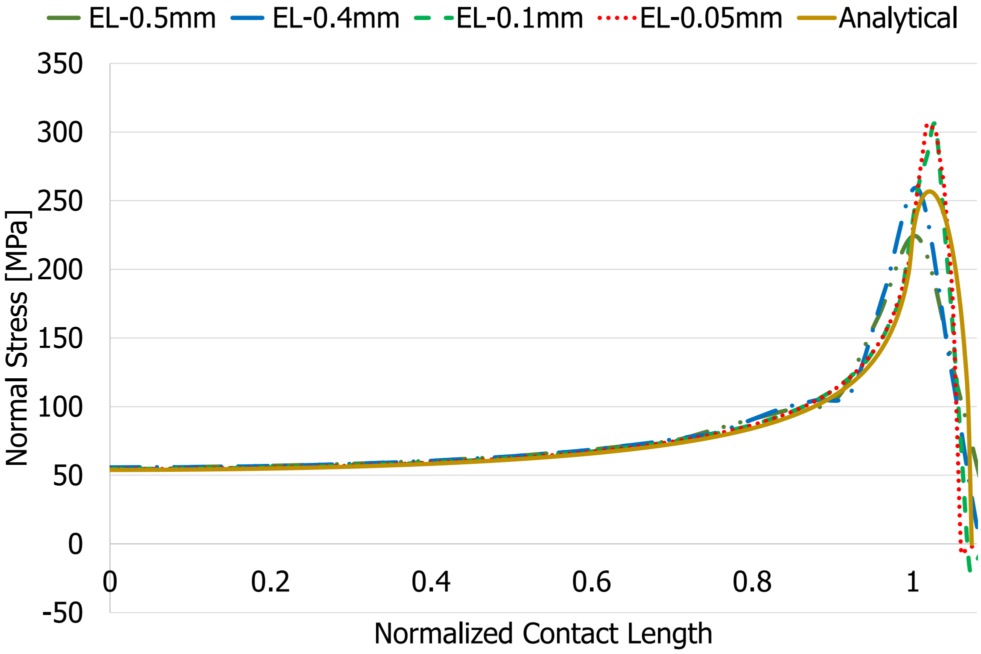

Figure 6.6: Normal contact stress profile for different element sizes.

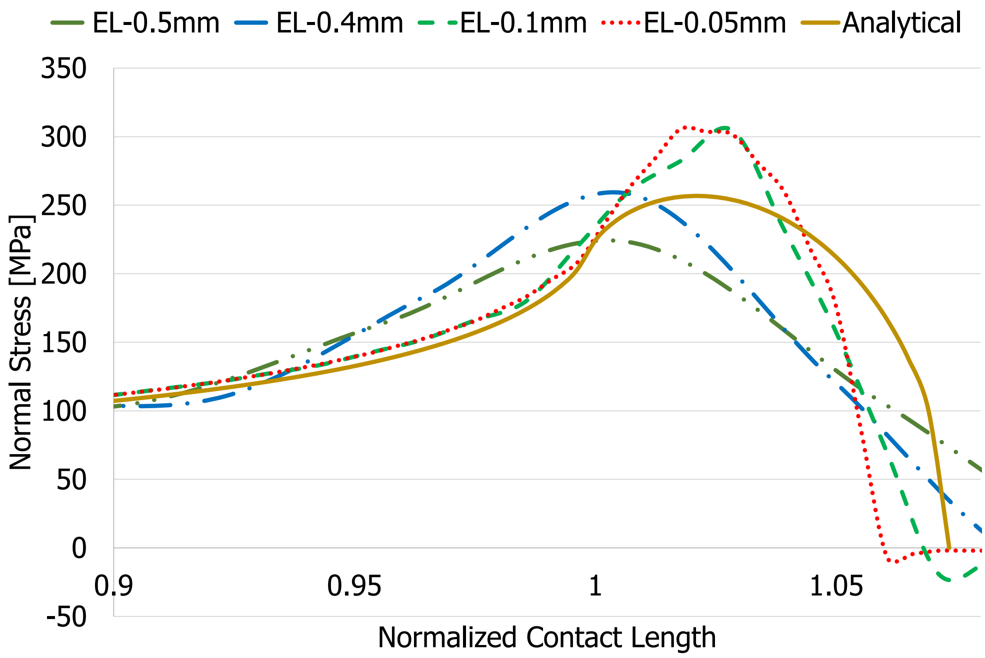

Figure 6.7: Detailed view of normal stress in contact with different element sizes.

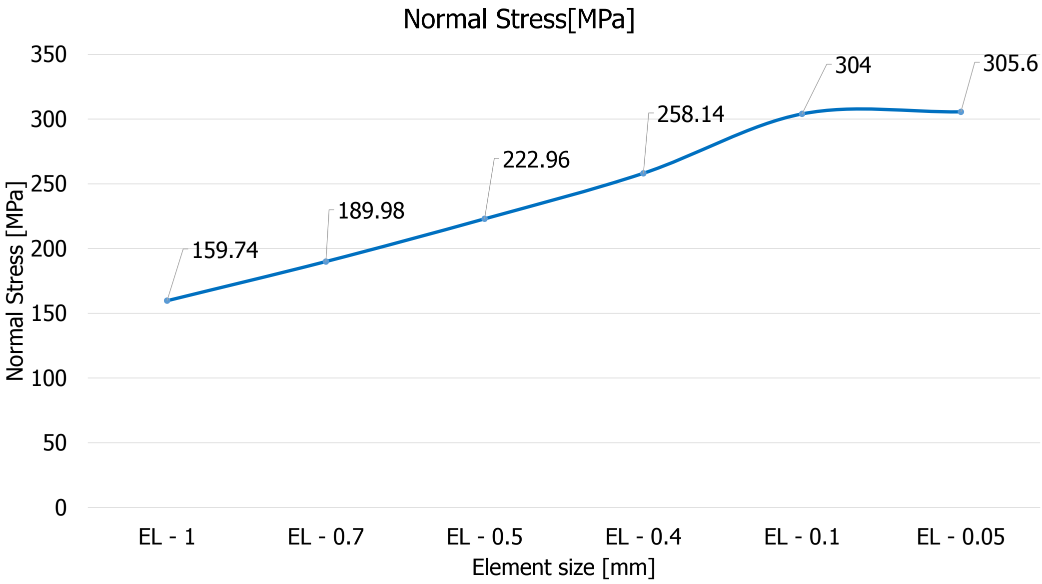

Figure 6.8: Mesh convergence for normal contact stress.

Figure 6.11-b illustrate Von-Misses stress distribution in the non-optimum geometry which is comparable with that of GA optimum geometry in figures 6.12-b. The equivalent stress for the optimum geometry is 39% less in comparison to that of non-optimum

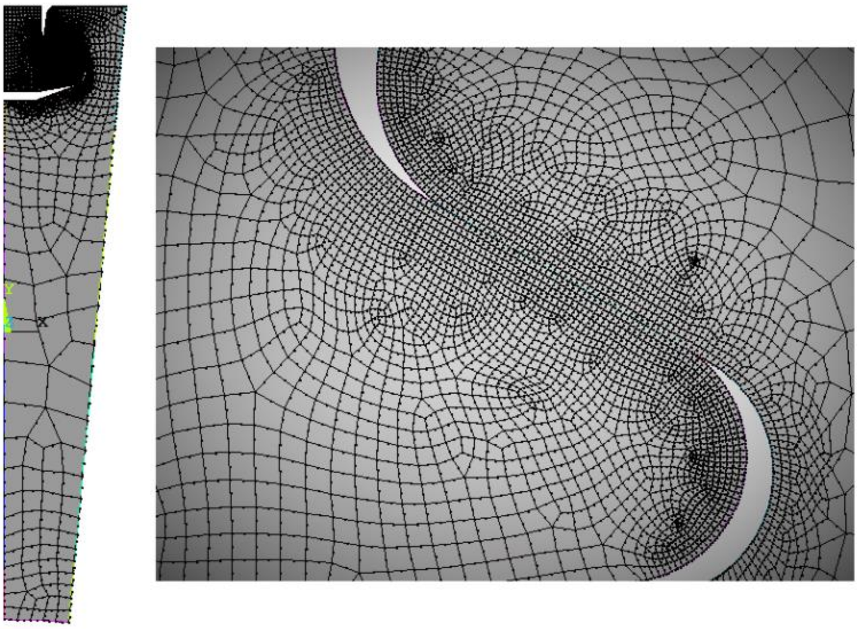

Figure 6.9: Automatic generated mesh of a dovetail parametric model.

geometry. By further surveying Figs. 6.11-b and 6.12-b, it is found that the optimizer tries to employ entire geometry to withstand the loadings thus one may find more uniform stress among the geometry. On the opposite, for the non-optimum geometry, stress changes more intensely point to point, providing high concentrated stress. Although the mean equivalent stress is higher in the neck area of the blade part for the optimum shape (which is an adverse effect in terms of creep failure) but the value is still far from the critical stress of the material. Nevertheless, for an advanced design, it is recommended to put extra constraints for the mean stress in critical areas.

Figure 6.11-a and 6.12-a compares pressure in contact for the non-optimum and the optimum geometry, respectively. It is found that this value is 37% less for the optimum one. Note that although the peak of the equivalent stress happens at the top part of the contact, the peak of the contact pressure for the optimum geometry has moved to the bottom part of the contact which is the opposite to the non-optimum geometry. The contact pressure graphs corresponding peaks on the equivalent stress contours are defined by letters A and B in corresponding figures. The contact line is longer for the optimum geometry which provides more mating surfaces for transferring the centrifugal loads.

By including the KRG model in the genetic algorithm optimization procedure the time to converge will reduce as some part of the fitness value evaluation performs by KRG model. As this optimization is done by the help of KRG model in addition to the FE model and the KRG model is not the only model providing the objective response for the optimizer, it is also called Co-KRG method. Figure 6.13 illustrates the optimum geometry obtained by Co-KRG method and compares with the GA-optimum geometry.

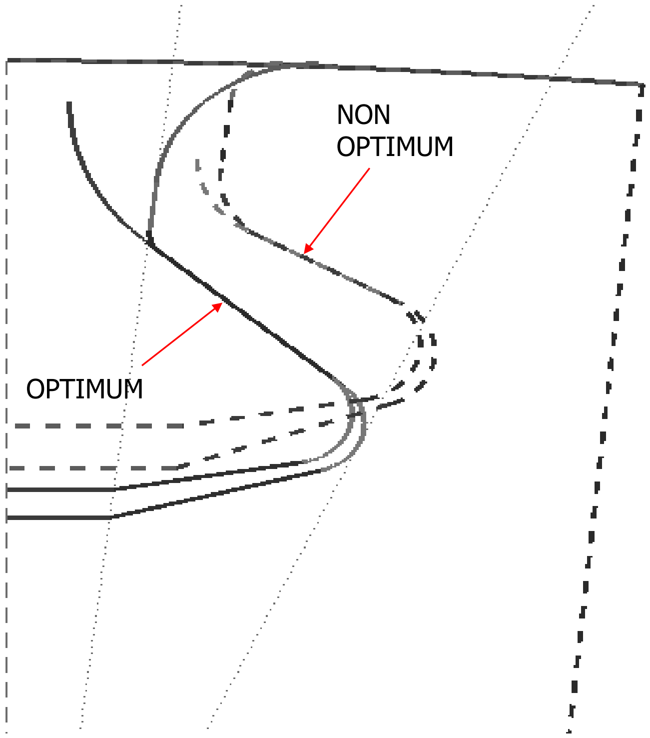

Figure 6.10: Optimum (continues line) vs. non-optimum (dashed line) geometry

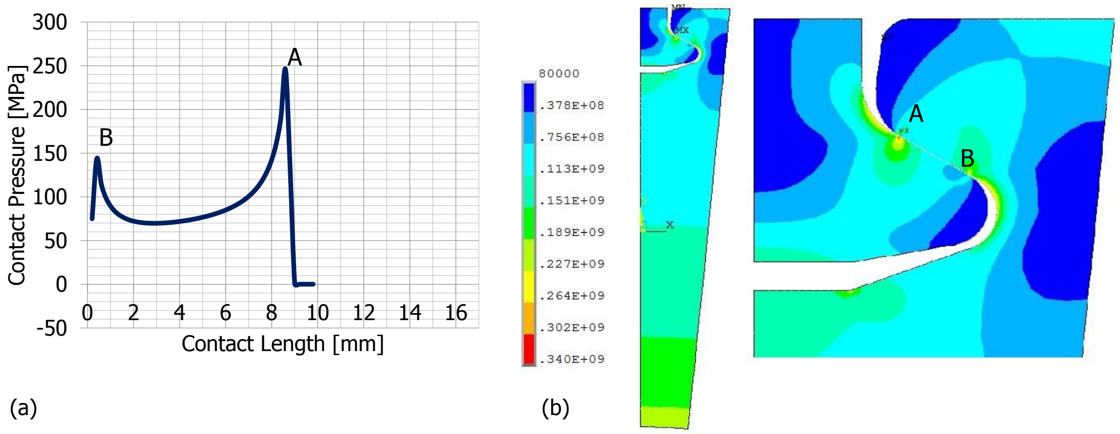

(a) (b)

Figure 6.11: Non-optimum a) Contact Pressure b)von-Mises stress contour (Max σ_{EQV}=339 MPa).

The convergence comparison between two methods can be found in Fig. 6.14. Figure 6.15-b contours the Von-Misses stress distribution in the Co-KRG optimum geometry.

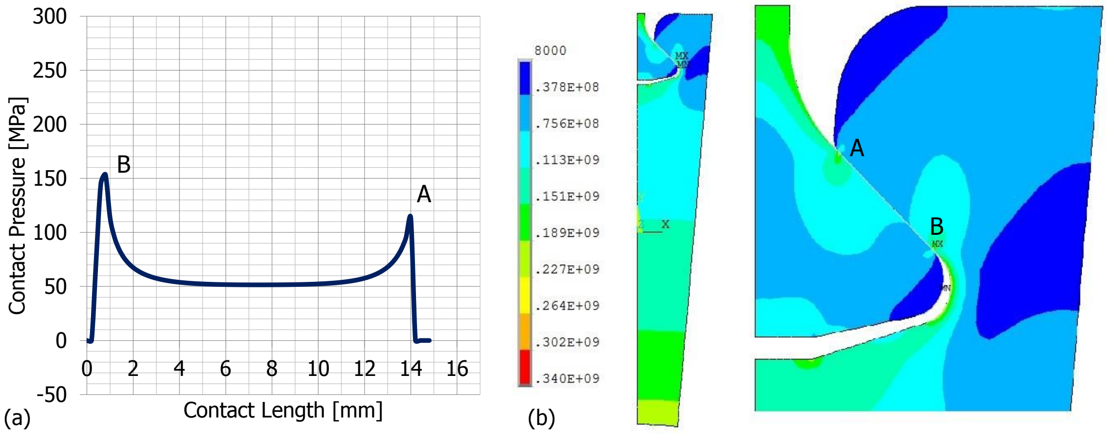

Figure 6.12: GA optimum geometry a) Contact Pressure b) von-Mises stress contour (Max σ_{EQV}=207 MPa).

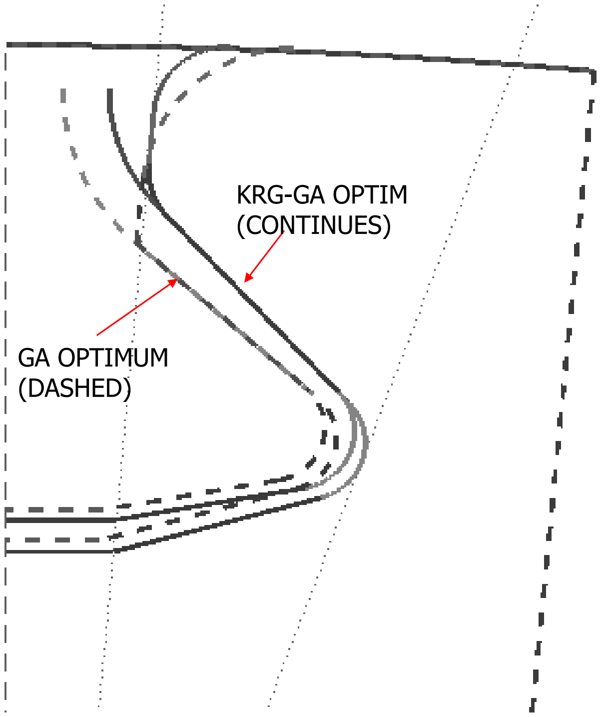

Figure 6.13: Co-KRG optimum (continues line) vs. GA-optimum (dashed line) geometry.

The equivalent stress for the optimum geometry is 36% less in comparison to that of non-optimum geometry. The number of FE analysis for the GA method was 14102 and for the Co-KRG was 3475 which is 75% less. Although the Co-KRG method could not provide the same reduction in the fitness value, the time to convergence overcome this small difference between the two methods. Figure 6.15-a illustrates pressure in contact for the Co-KRG optimum geometry. This geometry suffers 40% less peak stress comparing to that of non-optimum one. Figure 6.16 compares equivalent stress along the curve C2

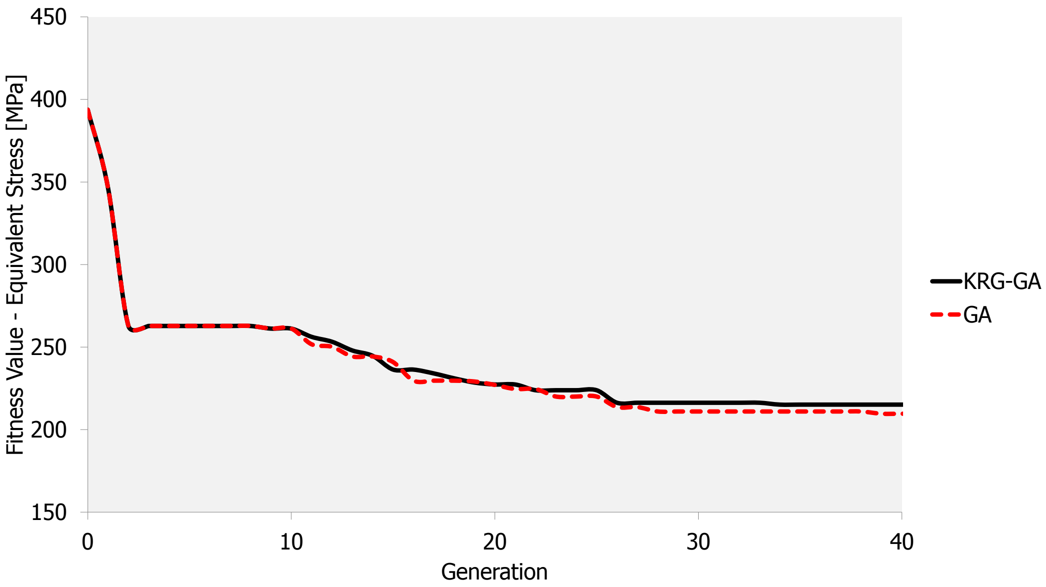

Figure 6.14: Genetic algorithm (dashed line) vs. Co-KRG convergence.

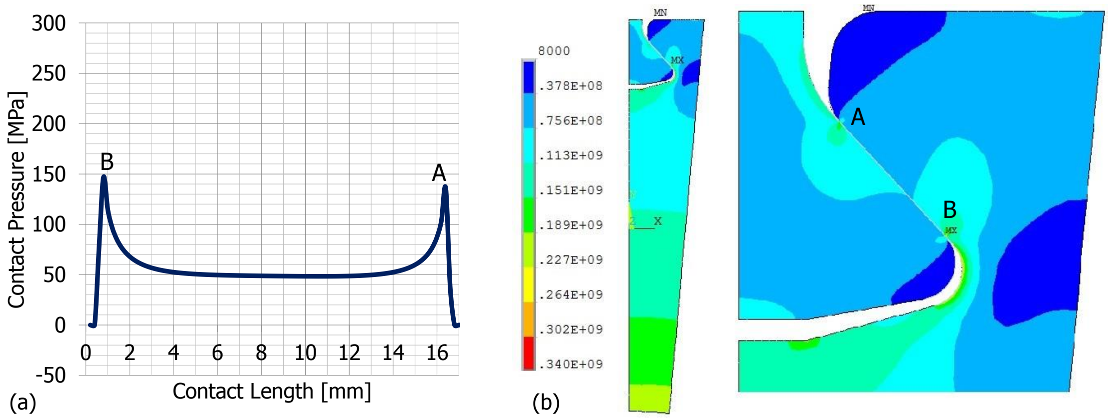

Figure 6.15: Co-KRG optimum geometry a) Contact Pressure b) von-Mises stress contour (Max σ_{EQV}=216 MPa).

(neck area of the disc) for the three geometries. The direction of plotting is from the lower part of the curve to the point B. Table 6.4 compares the contact length and the normal mean stress of non-optimum, GA optimum and Co-KRG optimum shapes. It is

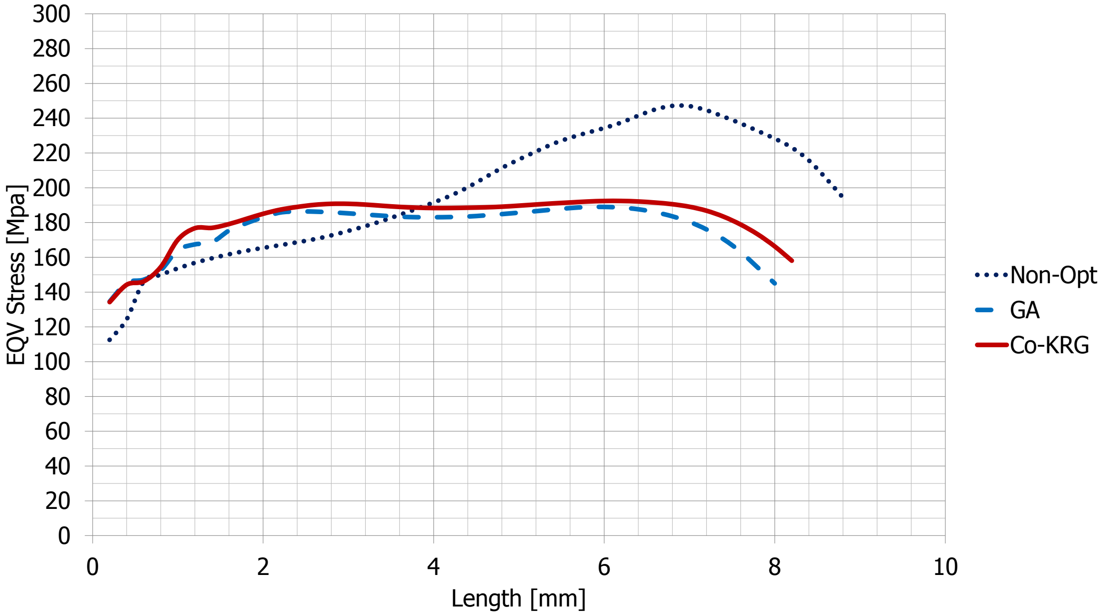

Figure 6.16: Equivalent stress along disc fillet edge.

found that the normal mean stress is less for the optimum shapes which has an advantage considering especially fretting fatigue. Figure 6.17 compares the contact normal stress for the three dovetail shapes. The length of contact is normalized to the non-optimum shape.

Table 6.4: Comparison of contact for non optimum and optimum shapes.

Parameter	Non-Optimum	GA Optimum	Co-KRG Optimum
Contact Length [mm]	9.334	14.548	16.779
Normal Mean stress [MPa]	88.4	58.6	55.4

The local sensitivity analysis has been performed by altering one parameter at a time while keeping all other parameters at their baseline value. The difference between obtained equivalent stress to the optimum one normalized to the optimum equivalent stress is the sensitivity measure.

$$\text{Normalized sensitivity} = \frac{\delta\sigma}{\sigma_{opt}} \tag{6.1}$$

The results are graphed in Figs. 6.18 and 6.18. As predicted the share of material devoted to the blade has the highest priority over other parameters.

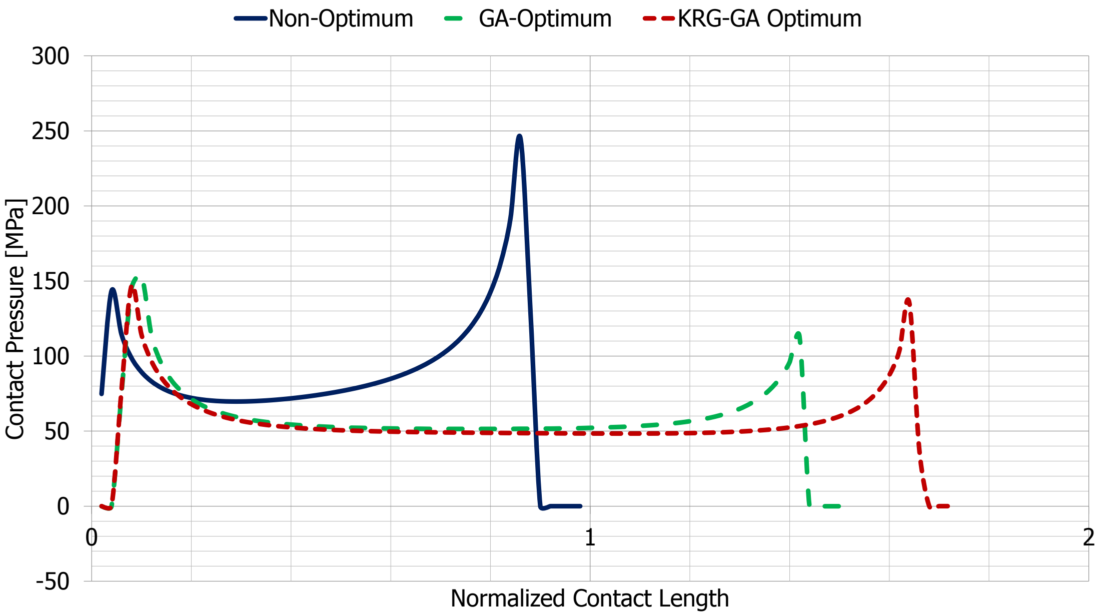

Figure 6.17: Contact Normal Stress comparison among non optimum GA Optimum and Co-KRG optimum dovetail.

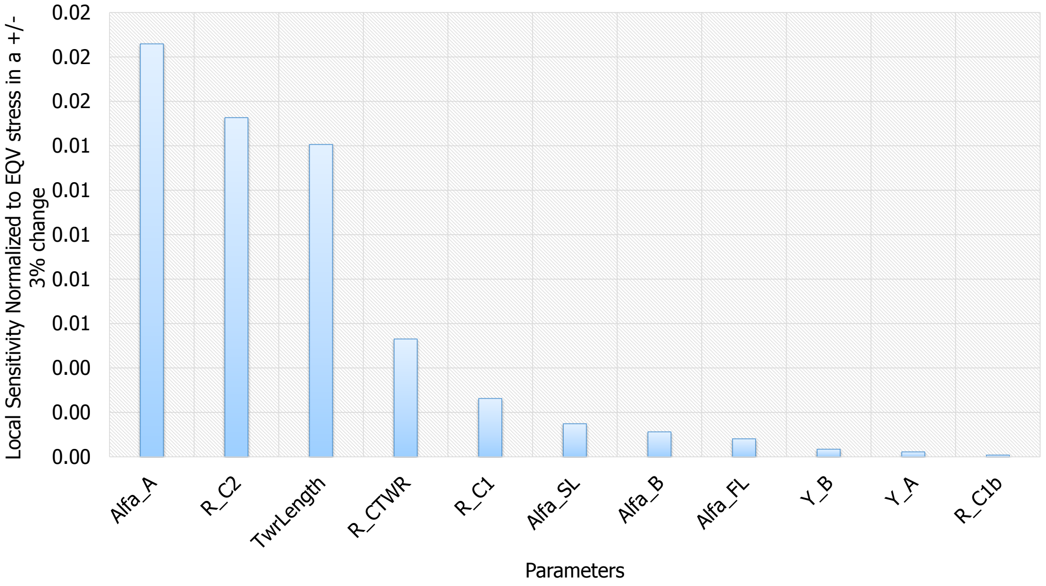

Figure 6.18: The local sensitivity arrangement in different input variable parameters in terms of equivalent stress.

In order to evaluate the effect of coefficient of friction different FE analysis performed and the results are graphed in fig. 6.20. By increasing the coefficient of friction the

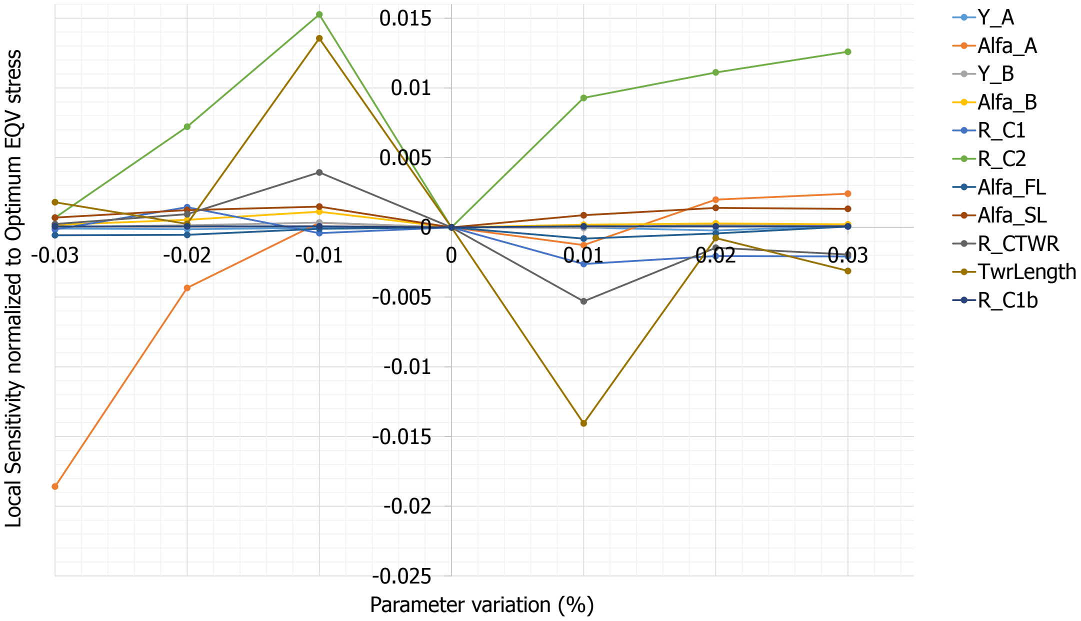

Figure 6.19: Details of normalized sensitivity for different input variable parameters.

maximum equivalent von-Mises stress transfer from the disc notch to the contact area.

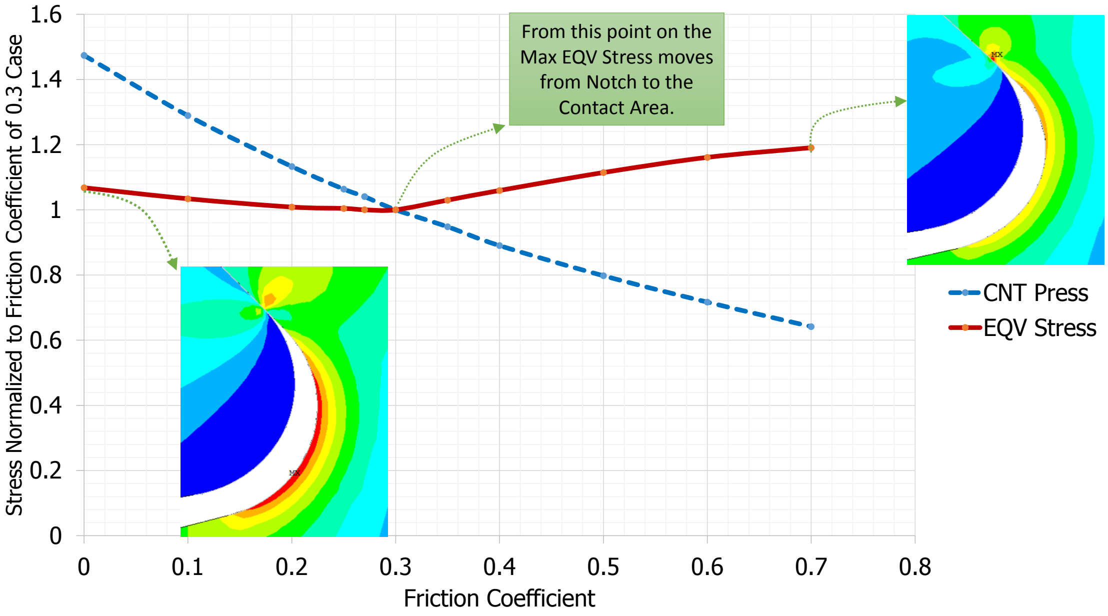

Figure 6.20: Contact Pressure and Eqv Stress for different coefficients of friction in contact.

In another optimization run with the objective of minimizing normal contact pressure the dovetail having less peak contact normal stress was demanded. Figure 6.21 compares the contact normal stress in the non-optimum and the optimum found for the dovetail. The profile of the contact stress is more Herzian in shape for the optimum dovetail. This attachment lacks the peak singular stress which is evident in the non optimum dovetail.

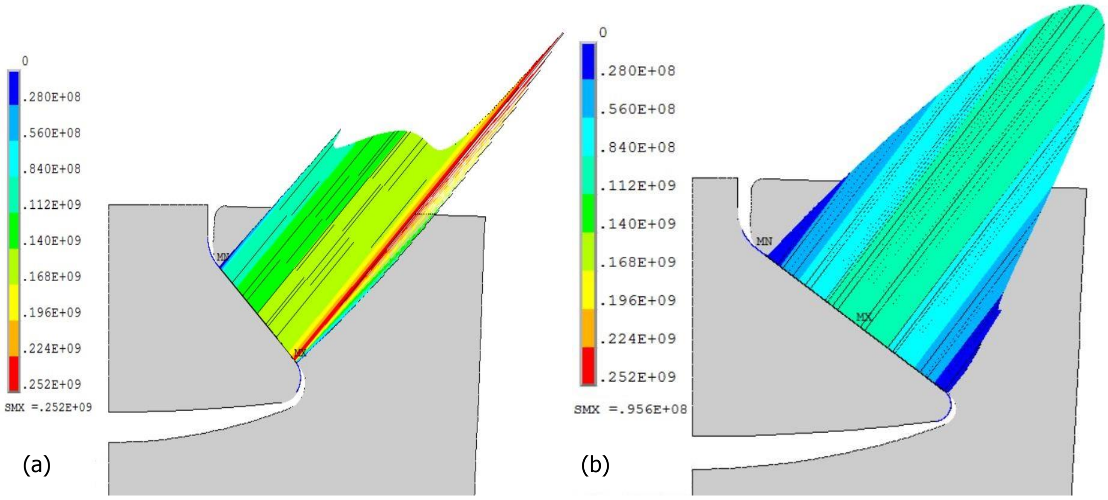

Figure 6.21: Contact Normal Stress on a) Non-Optimum b) Optimum dovetail.

6.3 Analytical Assisted FEM Approach - Fir-tree optimization

In this section, a fir-tree of four lobs is selected as a case study to evaluate the possibility of applying fast evaluation analytical method in combination of the FE method in a multi-objective optimization run. The main effort in this section is to present different strategies in embedding the analytical method into the optimization to lighten the heavy computational loads (i.e. less callbacks to the high fidelity model which in here is FE analysis) while maintaining the accuracy of the process.

6.3.1 Parametric model

A simplified parametric model as described in Fig. 2.3 along with an FE ready fir-tree parametric model described in Sec. A.3 having four lobs was used in this study.

6.3.2 Optimization Method and Constraints

A single objective Genetic Algorithm (GA) is used to find the optimum fir-tree shape having minimum von Mises stress. To do so, the different parameters of the parametric model is changed by the optimizer, then, their corresponding objective values are compared. The set of parameters are called input vectors and the objective value is a specific mechanical property of the geometry (which in the current study is the von Mises stress) evaluated by the finite elements method. Due to the fact that the number of callbacks to the FEM analysis is an index of the convergence time in such optimization process, the authors tried to decrease this number by incorporating the simplified model into the GA process before applying the FE (Fig. 6.22).

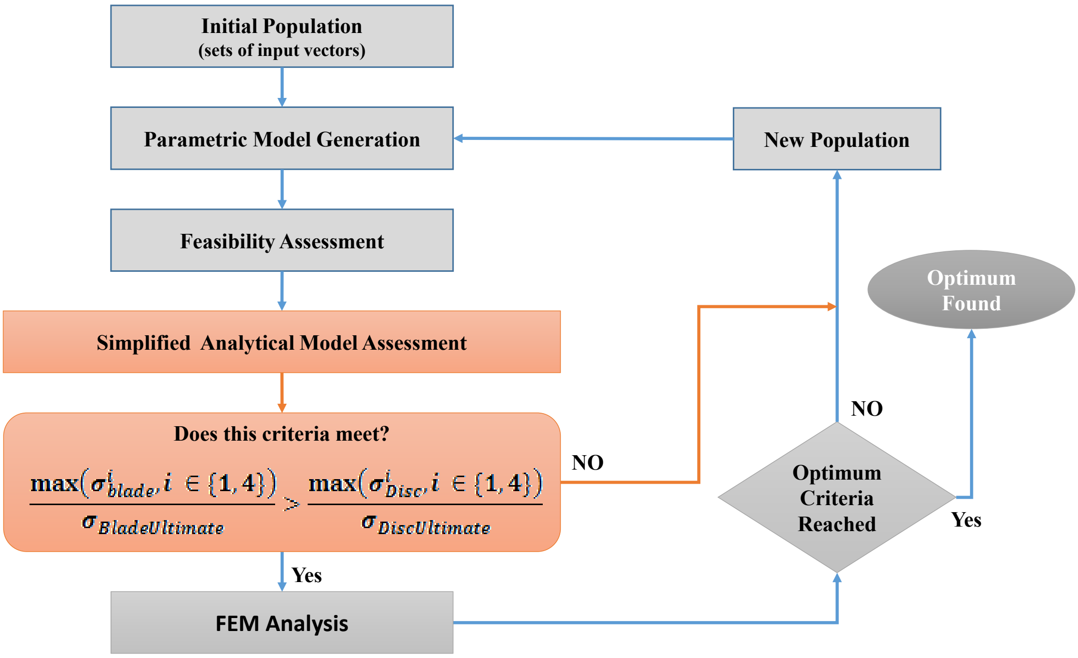

Figure 6.22: Optimization with GA embedding simplified model in addition to FEM callbacks.

The criteria for the simplified model is that the maximum average stress in the blade notch sections (Fig. 2.7) should not be less than the maximum average stress in the disc notch section both normalized to their corresponding material ultimate stress value. In fact, it is favorable to have the blade failure before disc failure for the practical reasons. Hence,

$$\frac{\mathrm{Max}(\sigma^i_{Blade}) \in \{1,4\}}{\sigma_{BladeUltimate}} = \frac{\mathrm{Max}(\sigma^i_{Disc}) \in \{1,4\}}{\sigma_{DiscUltimate}} \tag{6.2}$$

Although the analytical approach provides approximate results, at this level of filtration the stress obtained by the analytical approach is not compared to an absolute stress (for example the ultimate stress value of the material) but is compared with a stress obtained with the same method (analytical) on the other parts of the model. In other words, the comparison is made with the same tool, in the same conditions and with the same accuracy. Hence, the probability of facing a situation in which a candidate fails in the analytical approach but satisfy the same criteria with FEM is very rare (for the current trail it did not happen).

Using the LHS method, a brutal-force search were performed over the working domain of the current case study for which more than 8000 samples were evaluated by FE analysis in addition to simplified analytical model. The criteria of Eq.6.2 were evaluated with both models and it was found that only 6.5% of the searching domain fail in the analytical criteria but pass the same criteria by the FEM model.

Although, in the case of facing such conditions, the candidate may not be close to the optimum and would be filtered out in the proceeding generations. Moreover, if there is a candidate which does not satisfy the analytical approach but satisfy the same criteria with FEM and is still an optimum one, its robustness is questionable and is not recommended for considering as an optimum robust solution.

6.3.3 Analytical Assisted FEM Results

By applying the analytical approach in advance to the FE analysis in the optimization process, it was found a 7% improvement in time reduction for the total process. In fact, 7% of the callbacks for the objective values is done by the analytical part instead of high fidelity FE method. It is worth noting that the candidates filtered out are recorded and went under later evaluation to reassure the competency of the simplified analytical model filtration. It was found that all the filtered out candidates were incapable of satisfying the same criteria with FEM, hence in case of having no simplified model, all the filtered out candidates should have been evaluated by time-consuming FEM. Although, one may consider the fact that the improvement value obtained by the authors in the current trial is not a definite number due to the probability nature of the population selection of the GA method. It means that the GA initial population is selected from the searching domain by random selection, hence, by every different run, the optimization process will obtain the optimum searching through different population selections. Therefore one may not find the same ratio of the improvement by using the analytical evaluation.

In order to evaluate the behavior of the analytical results in comparison with the high fidelity ones (FEM results) during the optimization, the results of the analytical calculations were recorded for every individual shape of the fir-tree attachment during the optimization. Then, the results of the total populations were sorted for different criteria. Figure 6.23 compares the sorted mean contact pressure obtained by FEM and the analytical approach normalized to the blade ultimate stress. Also, Figs. 6.24 and 6.25 compare the maximum normalized mean tensile stress of the populations in the blade and disc sections, respectively. It was found that the analytical approach, although does not provide an accurate estimation of the stress (due to extreme simplification), but its general trend agrees with the FEM results. In another word, by minimizing the mean contact stress with the analytical approach, the same results with the FEM analysis would be minimized. The same behavior is evident for sections mean tensile stress. This phenomenon is utilized for another optimization approach which will be described next.

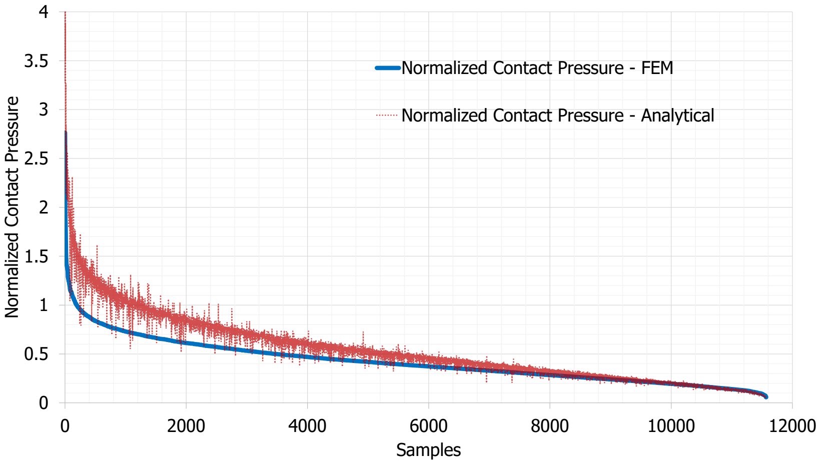

Figure 6.23: Contact pressure comparison in FE and analytical methods.

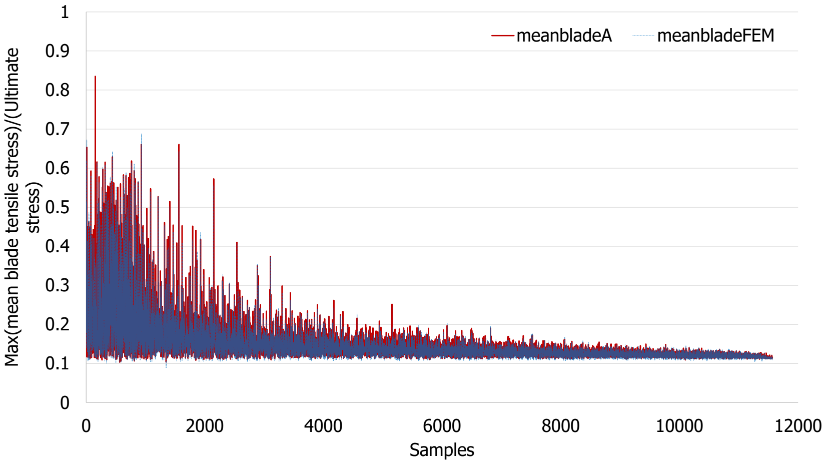

Figure 6.24: Normalized mean tensile stress in blade notch sections, the comparison in FE and analytical methods.

In addition, for having an understanding of the consistency of the two analysis approach, the error for the values obtained for every individual had been recorded during the optimization. This value was obtained by calculating the difference between FE value and the analytical value divided by the FE value again,

$$Err = \frac{FEM - Analytical}{FEM}$$

Total sample errors in the mean contact pressure, mean tensile stress in the blade and in the disk are shown as histograms in Figs. 6.26, 6.27 and 6.28 respectively.
It was found that the analytical calculations provided the best competency to the FEM results in blade section average stress. The mean contact normal stress had the highest

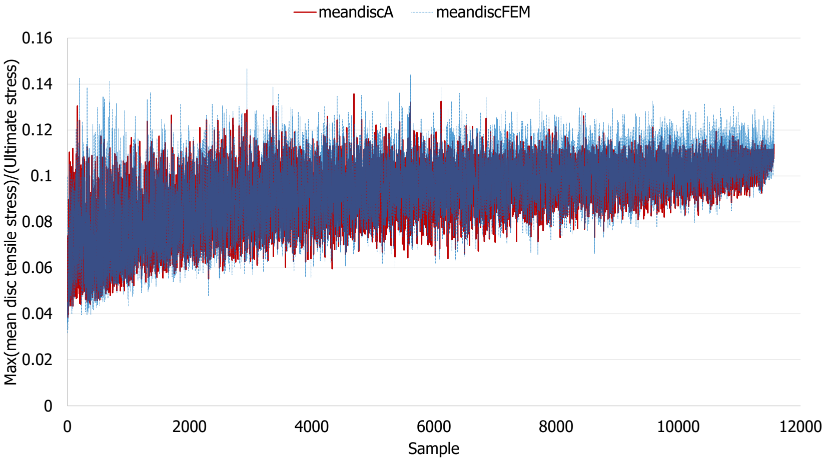

Figure 6.25: Normalized mean tensile stress in disc notch sections, the comparison in FE and analytical methods.

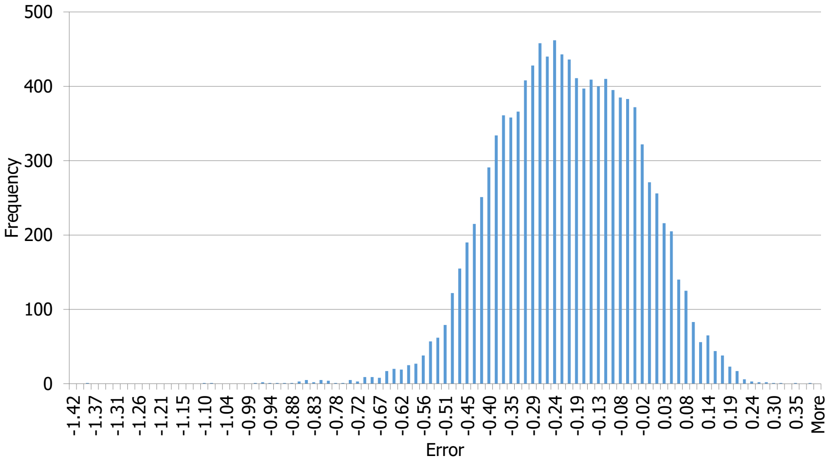

Figure 6.26: Histogram of the error for mean contact pressure (Standard deviation = 0.17).

standard deviation, hence, least competency to the FEM results among the three values.

In the previous optimization, it was found that the analytical approach, although did not provide good predictions for the objective values, its behavior in the optimization was in the same manner as the FE method. Hence, in another attempt, the authors tried to apply multi-objective optimization of the fir-tree attachment on just the analytical solver for the two objectives of a minimum of the maximum normalized sections tensile stress in addition to the minimum of the normalized mean contact stress. Due to the fact that the analytical method is not able to have any prediction of the maximum stress in the notch area, hence, the parameter of notches radius (R_{C1} and R_{C2}) will not be addressed in an

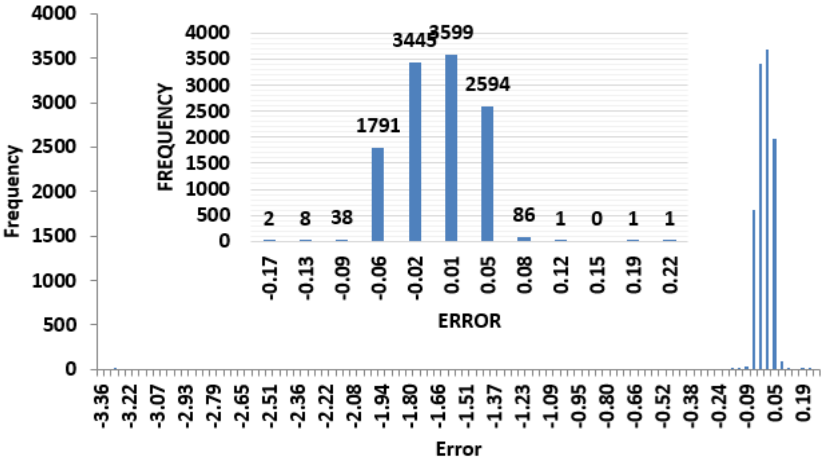

Figure 6.27: Histogram of the error for mean tensile stress on the blade (standard deviation = 0.046).

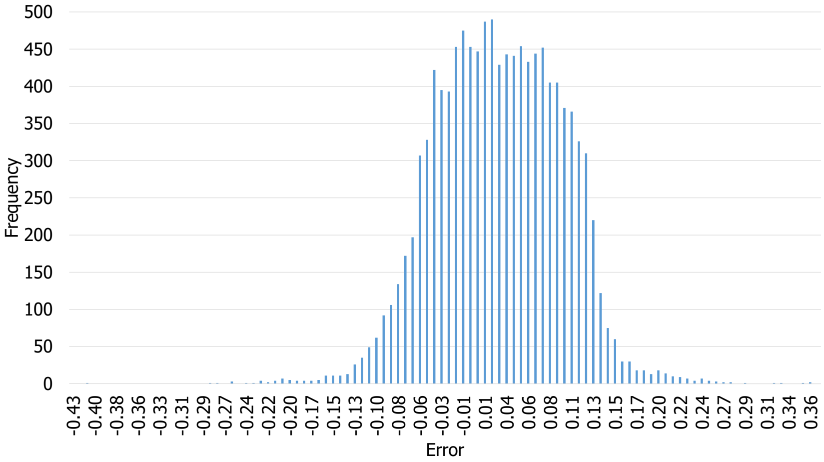

Figure 6.28: Histogram of the error for mean tensile stress on the disc (standard deviation =0.067).

optimization based on just analytical approach. To rectify this problem, these parameters must be kept constant during the optimization. It means that for all combinations of R_{C1} and R_{C2} the multi-objective optimization shall be carried out. Due to the fact that the analytical approach is not a complex calculation, so this process is comparatively a fast practice. The results in this level would be a number of Pareto fronts. Then, all the points obtained in the Pareto fronts went through FE analysis. The final results were collected and sorted. The sample having the minimum von Mises stress yet meeting the constraints would be considered as the optimum fir-tree attachment shape (Fig. 6.30). This method is referred to Analytical Multi-Objective FEM validated Optimization in the current study.

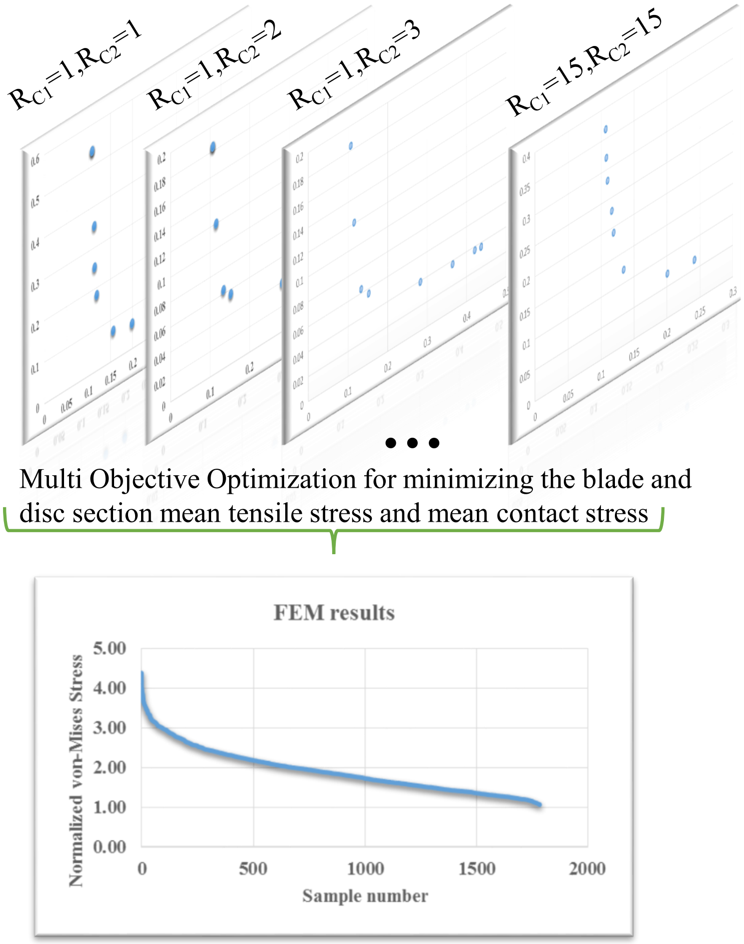

Figure 6.29: General idea for the analytical multi-objective FEM validation optimization method.

As the objective for the optimization of the blade fir-tree in the current study was minimizing the von Mises stress, the results from the previous step were again fed into another single objective GA optimization, but, with a reduced searching domain. To do so, the optimum set of parameters found in the previous optimization were used as the median of the new range of parameters variations and were subjected to a variation of +/-10%. This reduced range of parameters made this level of optimization much faster to converge because there was a smaller domain to search. This method is referred to as Analytical-FEM Multi-Objective Multi-Level Optimization in the current study.

To sum up, in order to reduce the convergence time in minimizing the von-Mises stress in a fir-tree attachment, four different methods were applied to a parametric model;

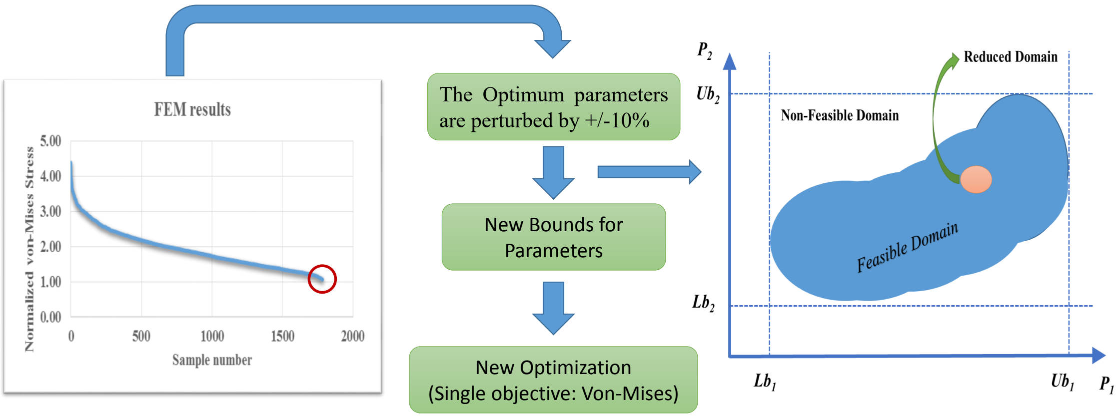

Figure 6.30: Reducing the searching domain using a simplified analytical model.

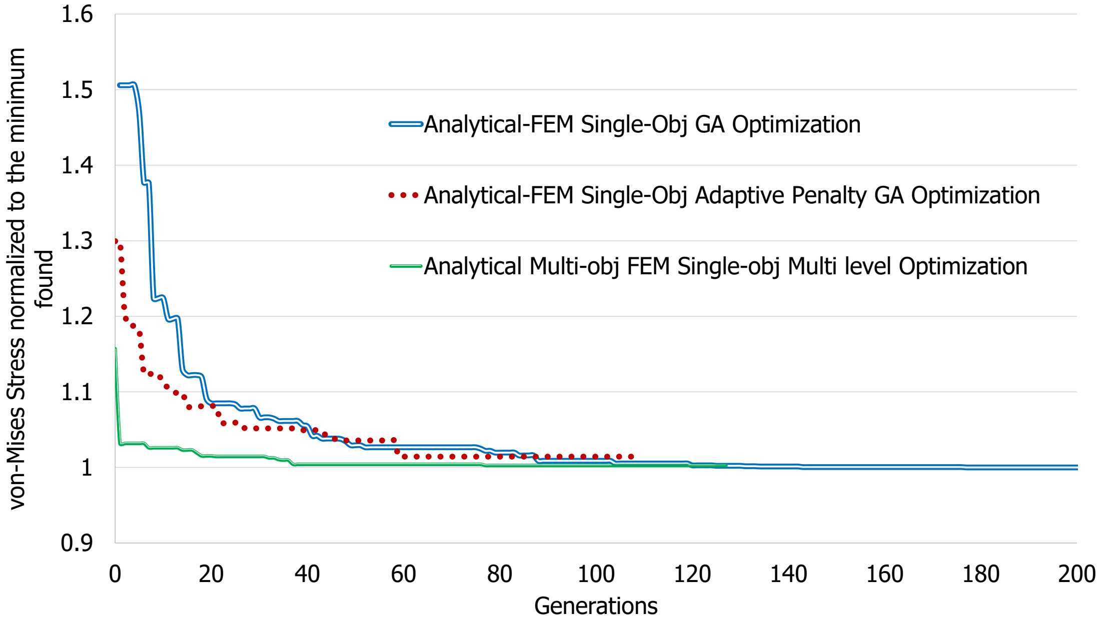

Figure 6.31: The comparison of optimization convergence for different methods.

Analytical-FEM Single Objective Optimization, Analytical Multi-Objective FEM validated Optimization, Analytical-FEM Multi-Objective Multi-Level Optimization and Adaptive Penalty Analytical-FEM Single Objective Optimization. Figure 6.31 compares the optimization convergence for different methods described so far. For the case of Analytical-FEM Multi-Objective Multi-Level Optimization, just the second level of optimization convergence is shown in this figure due to the fact that the first level includes a high number of optimizations. Also, it is worth to note that in this case a faster convergence is

Table 6.5: Improvement comparison of different methods of optimization.

Method of Optimization	Improvement in Optimization Time	Normalized Min von-Mises found
Analytical-FEM Single Objective Optimization	7%	1
Adaptive Penalty Analytical-FEM Single Objective Optimization	47%	1.014
Analytical-FEM Multi objective Multi level Optimization	32%	1.005
Analytical Multi objective FEM validated Optimization	86%	1.104

evident as the search domain has been decreased in the first level of optimization. Moreover, as seen, the proposed adaptive penalty has successfully improved the ability of the optimizer in finding the optimum.

Table 6.5 compares the improvement in the optimization time according to the number of callbacks to FEM analysis for different methods. Also, the optimum objective value normalized to the best value found is compared in this table. It is found that the adaptive penalty based on LHS method decreased the time for convergence significantly. Furthermore, the analytical approach could successfully reduce the searching domain for the FEM optimization. Although the optimization using just an analytical approach may provide the fastest convergence (about 86% less FEM callbacks), the result is not satisfied (more than 10% error). Whereas, using the results of this method for reducing the searching domain in the second level optimization provided 32% improvement in the convergence time plus a satisfactory optimum value (less than 1% error).

6.4 Co-Kriging GA Optimization applying Adaptive Penalty

In this section, a dovetail in addition to a four lob fir-tree parametric model are under optimization investigation using co-Kriging surrogate function embedded in the genetic algorithm as described in section 4.4. Moreover, the penalty method proposed in section 4.6 is applied for examining its capability to provide fast convergence.

6.4.1 Parametric Model

The parametric models described in A.2 and A.3 were used for dovetail and fir-tree optimization, respectively.

6.4.2 Optimization Constraints and Objectives

In the current case, a multi-Objective optimization was performed to satisfy two objectives simultaneously. To optimize the geometry of the attachment, the parametric model is delivered to a finite element code to evaluate the state of stress. This analysis is denoted as “high fidelity” computation. In the current study, two objective functions f1 an f2 were obtained from the high fidelity analysis,

$$f1 = Max[\frac{\sigma 1_{blade}}{\sigma_{UTS_{blade}}}, S \times \frac{\sigma 1_{Disc}}{\sigma_{UTS_{Disc}}}] \tag{6.3a}$$

$$f2 = P_{CNT} \tag{6.3b}$$

where, σ_1 and P_{CNT} are the highest first principal stress in the blade or disc notches and the mean pressure in the contact, respectively. The first principal stress σ_1 was normalized by the ultimate tensile stress σ_{UTS} of the corresponding material. S is the safety factor of the disc part as it is desirable to have the failure in the blade component rather than in the disc. In the current study, it is assumed that $S = 1$. A brief description of the general optimization is that the optimizer automatically changes the set of input variable parameters (which is also called ‘input vector’) of the model and calls for the evaluation of its corresponding objective/s (which in here are states of stress defined in 6.3a and 6.3b). This loop is repeated until the objective value/s reach a minimum, hence, the best combination of the input parameters (best input vector) is found. In case of multi-objective optimization, the optimizer provided a Pareto Optimal Front in which a set of optimal solutions are given.

6.4.3 Robustness

Although the tolerance in manufacturing due to high technology tools and control devices has been reduced significantly, the component on the sketch is still far from the real fabricated one [1]. In order to reduce the expected quality loss, both variance and the difference between the mean and the nominal response should be minimized. In fact, assuming a bell-shaped response distribution (normal distribution), in robust design the main concern is to align the peak of the bell to the nominal response and make the bell curves thinner (reducing the variance) [22]. To achieve a multi-objective and robust design, the integration of parametric geometry, high fidelity (e.g. finite element) and/or a surrogate model in collaboration with an optimization algorithm is required [58]. Design optimization using computational mechanics has been recently combined with robust design and provided the term optimal robust design. Nevertheless, due to the high computational cost of high fidelity models, extensive efforts have been done to find the optimal robust solution using metamodel interpolations, although the inherent uncertainty in the metamodel interpolation may cause the solution not robust as it should be [3]. Taguchi has used Signal-Noise (S/N) ratio as the quality characteristic of the product. S/N ratio is used as measurable value instead of standard deviation due to the fact that, as the mean decreases, the standard deviation also decreases and vice versa [50]. In quality engineering, many types of signal-to-noise (S/N) ratios are usually calculated to measure the robustness for the functions of products, processes, or technologies. There are some types such as Smaller-the-better, Nominal-the-best, Larger-the-better, Signed target and Fraction defective [101]. In nominal – is – the best type approach, the quality loss occurs when the objective value does not coincide with the response value. In general, most component properties in a design process is of this type for which there is a fixed signal value (nominal value). Having the variance of the output, σ, around the nominal value, μ, the S/N ration is obtained by,

$$S/N = 10 \times \log_{10}(\frac{\mu^2}{\sigma^2}) \tag{6.4}$$

This ration is considered as the robustness scale in the current study.

6.4.4 Robust Multi-Objective Optimization

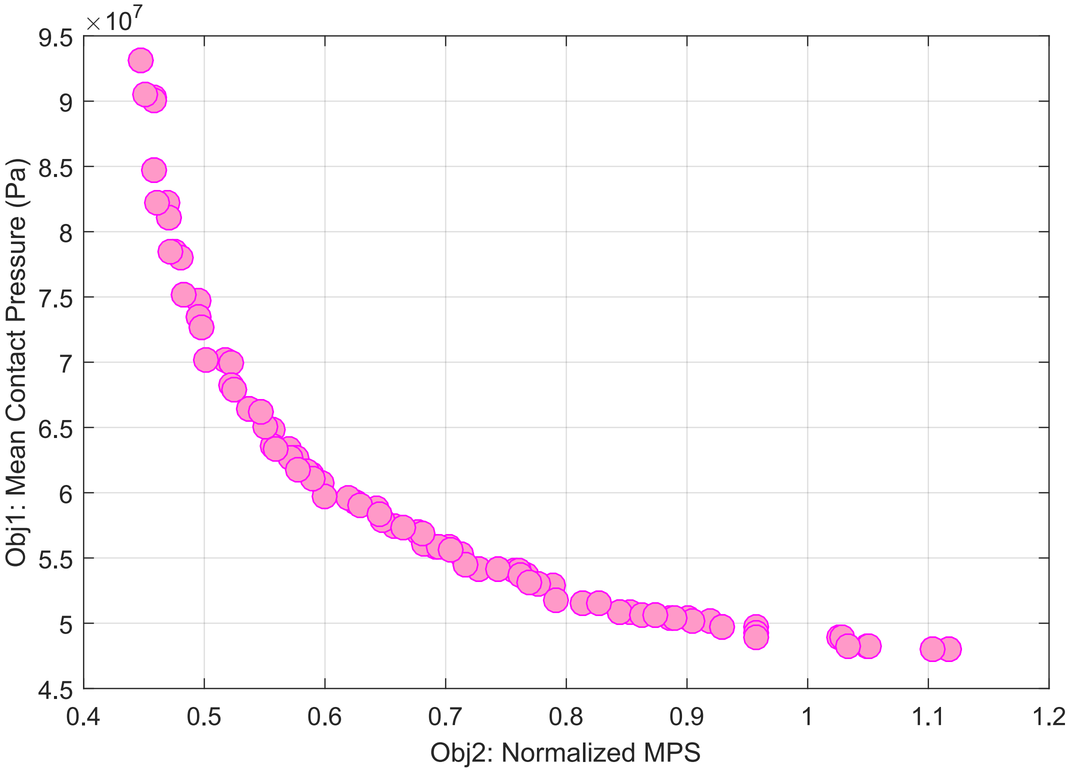

Figure 6.32: Pareto Optimal front for max first principal stress (Obj1) and mean contact pressure (Obj2)

In the current study, a multi-objective optimization was performed with two objectives, the first principal stress σ_1 and the contact mean pressure $p_{c,m}$, denoted as objective 1 and objective 2 respectively. The disk and the blade are made from different materials, then the first principal stress is normalized by the ultimate tensile stress UTS of the corresponding component material. The first principal stress can not exceed the ultimate tensile stress, then, a limit to the objective 1 must be defined. In the current analysis this limit has been set to 0.6, hence values passing this threshold were rejected in the results. Regarding the fact that the contact pressure is the same for mating surfaces this normalization can be avoided for objective 2. Figure 6.32 visualizes the results of the multi-objective optimization as a Pareto Optimal front. In a multi-objective optimization 'a point is called Pareto optimal if there is no other point that reduces at least one objective function without increasing another one' as reported in [63]. In other words, there is not a unique optimum point but a family of them. Here, an optimum point having maximum robustness was chosen among the Pareto optimal.

Maximum robustness means that by having some perturbation in the set of the parameters the objective value does not change significantly. Hence, all the points in the Pareto Optimal front were evaluated for sensitivity to find the best individual in terms of robustness.

A very simple method to evaluate sensitivity is to make small variations in one parameter at a time, keeping all other parameters unchanged and checking the deviation of the objective from its nominal value. The nominal value of the objective is given by the Pareto Optimal front. This method is called local sensitivity analysis and does not always provide a realistic indicator of sensitivity as the uncertainty may not occur only in one parameter at a time. Whereas, in a global sensitivity analysis uncertainty is applied simultaneously to every parameter of a set. Considering a model having n parameters, if sensitivity analysis requires to apply h different levels for every parameter the total number of combinations are as large as h^n. Hence, it is not suggested that the global sensitivity analysis to be performed by the high fidelity model as the process cost is terribly high in terms of time. Therefore, applying surrogate model (also called Meta model) is highly recommended in such evaluations. Moreover, the accuracy of the Meta model is expected to be especially high as the range of variations in the parameters is very narrow (at most, only 3 percent of the original value is the border of the domain).

In the current study, a maximum deviation of 3% of the parameter was applied to the input vector. This deviation was split into seven levels [-3,-2,-1,0,+1,+2,+3]% assuming a uniform discrete distribution. Hence, the total number of deviated points for a 6 parameters model was $n_e = 7^6$ for each point on the Pareto Optimal front. This huge number of evaluations makes the use of the high fidelity model quite difficult. Then, the same Meta model described in Sec. (E.1.4), was used to calculate the objective function $p_{c,m}$ per each deviated point. The corresponding standard deviation is

$$S = \sqrt{\frac{1}{n_e}\sum_{i=1}^{n_e}[(p_{c,m})_i - \mu]^2} \tag{6.5}$$

where μ is the mean of $p_{c,m}$.

6.4.5 Dovetail Robust Optima

Figure 6.33 graphs the Pareto Optimal Front obtained from the multi-objective optimization in the previous section. For every sample point in this graph two values are illustrated; the mean contact pressure and the S/N ratio (Eq. 6.4). Also, there is a dashed line in this graph which segregates samples having MPS higher than a predefined value from those having lower MPS values (from zero to the dashed line). The most robust point in terms of mean contact pressure for which the MPS has not exceeded the limit of 0.6 is selected as a candidate for the optimum robust shape. Then the robustness in terms of MPS was also evaluated to make sure that the selected optimum provides robustness in both objectives.

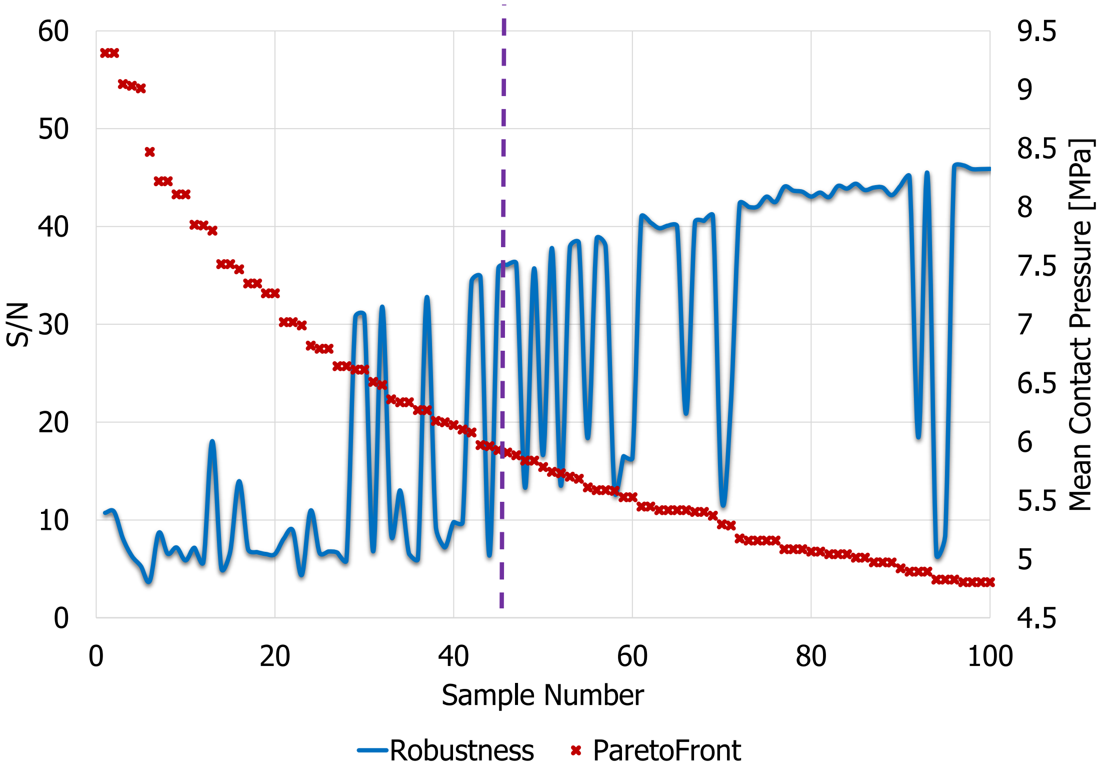

Figure 6.33: The dovetail robustness analysis of the Pareto Optimal front sets of parameter (the dashed line is the limit for MPS=0.6)

In order to obtain the optimum robust input vector, the candidate having the lowest mean contact pressure yet highest S/N value which at the same time does not exceed the threshold of MPS (dashed line) was selected (Fig. 6.33). The mean contact pressure for the selected input vector is 60 MPa and its corresponding normalized MPS is less

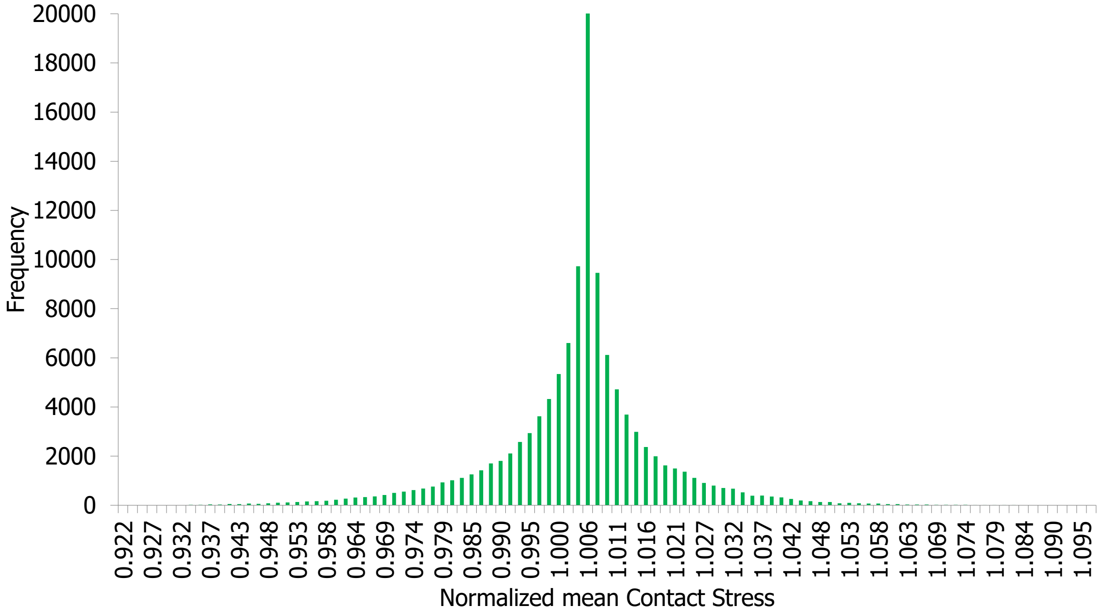

Figure 6.34: Histogram on Meta model evaluation for a 3% perturbation in Optimum Input vector (Unit is the optimum value)

than 0.59. Table 6.6 provides the results of the robustness analysis in which a robust design input vector in both objectives is provided. The histogram results of the surrogate function over the optimum geometry is shown in Fig. 6.34. The ratio of the standard deviation to the optimum is 0.029 which is quite satisfying.

Table 6.6: The robustness analysis result for the final robust optimum geometry vector

	MPS (normalized)	Contact Mean Pressure (MPa)
Standard Deviation	0.026	1.7
Mean	0.583	60.46
S/N	27	31

6.4.6 Fir-tree Robust Optima

A fir-tree of 3 lobs was also applied to the same procedure of robust optimization done for the dovetail in the previous section. In the case of fir-tree the number of parameters are higher hence to perform the robustness analysis a higher number of population should be generated and evaluated for every single input value in the Pareto Optima Front (7^8) which makes its calculation rather challenging even for a Surrogate model, therefor, 1000 points were selected using a uniform distribution selection through the perturbed population of every single sample from which the S/N was calculated. The graph of the S/N calculated for both objectives for the Pareto Optima Front candidates has been illustrated in Fig. 6.35.

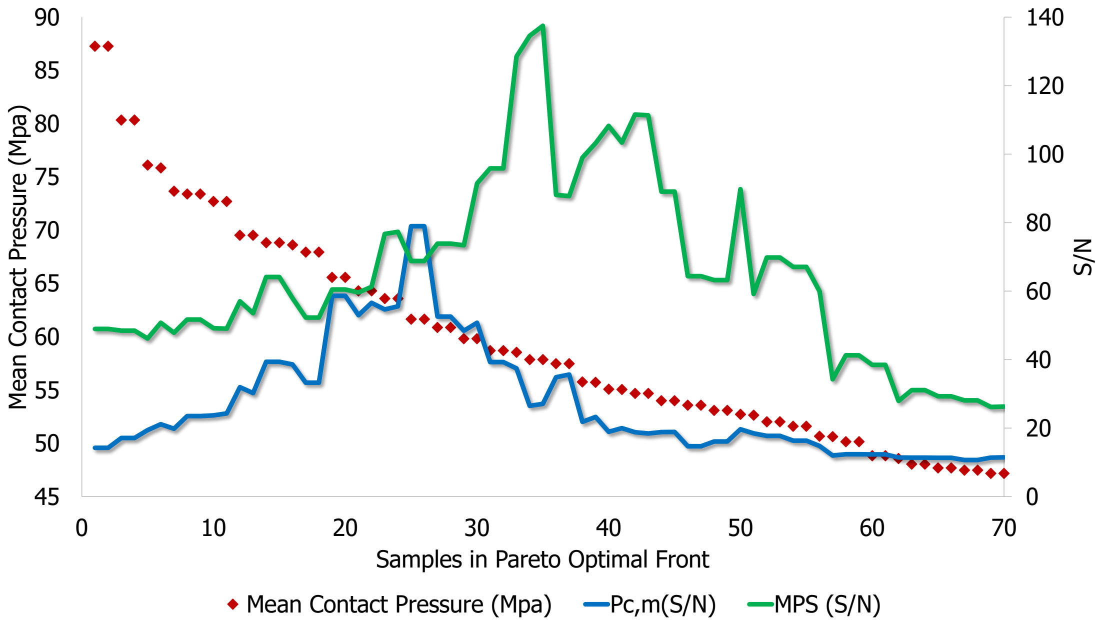

Figure 6.35: The robustness analysis of a set of Pareto Optima Front for a fir-tree

6.5 Conclusion

A dovetail parametric model was optimized for the minimum contact peak normal stress using two different approaches of FE analysis and Analytical calculations. The aim was to evaluate the possibility of the simplified analytical model in the optimization of the attachment. The results were found promising. The contact peak stress in the optimum found by the use of the analytical model was comparable to that of the FE model.

Then, the adaptive surrogate model embedded in GA (Co-Kriging method) described in section 4.4 was applied to a dovetail. The Co-Kriging method could successfully reach the optimum by 75% less computational burden. Moreover, the sensitivity of different parameters of the parametric model of the dovetail to von-Mises stress in the attachment was demonstrated. The effect of coefficient of friction on equivalent stress was also studied. It was found that decreasing the friction may transfer the peak stress zone from the contacting surfaces to the notches which is not always desired as it is more favorable to have the failure in the blade rather than in the disc component.

In another attempt to reduce the computational burden of the optimization, the simplified analytical model of a fir-tree was employed but not as a standalone response function. This model was used as a filtration before performing the FE model in the optimization cycle. In fact, the simplified analytical model was responsible in controlling the criteria of having failure in the blade component before having the rupture in the disc component. Hence, the least proper candidates were filtered out not to be passed to the high-cost FE analysis. This approach could reduce the computational time by 7%. Moreover, a multi-objective optimization was performed solely on the simplified analytical model. Although this method could reduce the computational burden by 86%, the optimum von-Mises stress was 10% far from the optimum found by the previous method (reference one). In another attempt, the results of the analytical optimization method were used to reduce the searching domain for another single objective (minimum von-Mises stress) optimization of the attachment using the FE model. This method could reduce the computational burden by 32% by a negligible error of 0.5%. Furthermore, applying the proposed adaptive penalty to the combined simplified analytical and FE model optimization could reduce the computational burden by 47% which again proved its efficiency.

Finally, the Co-Kriging method was applied to an optimization of a dovetail and also a fir-tree with the objective of minimum mean contact pressure and minimum peak principal stress. In this study, the surrogate function was also used to predict the robustness of the samples. The final results provided the designer with a set of candidates with different (weighted optimum) values of objectives in addition to their robustness in terms of both objectives. It was found that finding a robust optimum is impossible without using a surrogate function to emulate the response values.

Chapter 7

Closure

In finding the optimum shape of the dovetail and fir-tree different methods and criteria were evaluated. Two approaches of analytical and FE approach were considered in developing two types of parametric method for blade and disc attachment. Genetic algorithm was used as the optimizer. An adaptive penalty method based on LHS was proposed and evaluated in the optimization of a standard Rastrigin function manipulated to include non-feasible spaces, then, blade root dovetail was subjected to the optimization using this penalty method. In both evaluations, the proposed penalty method showed to be promising in reducing the computational time for convergence. Moreover, by targeting the optimization of a fir-tree with 3lobs it was found that in facing a more complex and higher dimension searching domain, this method is more efficient in guiding the optimizer to the feasible space and subsequently faster convergence.

In addition, employing the analytical approach as a filter before performing the high-cost FE method revealed that filtering out some part of candidates by the analytical evaluation makes an improvement in total time for convergence. Moreover, applying the Kriging function as a surrogate alone is not an efficient method in finding the feasible optimum solution, although, embedding this function as a pre-evaluation method before performing the FE analysis in the optimization loop is promising in terms of both accuracy and time savings.

Comparing different topologies of the contact surfaces in a dovetail as a sample to blade attachment was performed with four different topologies. It was found that the crown type topology proposed by [92] provided less contact peak normal stress although the designer should consider the over speeding conditions in selecting this type of topology with caution as it may lose its normal behavior in loadings higher than design point. Also, a great agreement in normal stress profile in contact surface was found between analytical punch results and the contact in the blade root attachment. Accordingly, an optimization run done by analytical estimation of the contact normal stress peak provided a promising solution.

In a multi-objective optimization of a fir-tree and dovetail, it was tried to find the optimum robust solution using S/N nominal-the-best ratio. The Kriging function used in optimization was also utilized in evaluating the global sensitivity and robustness of the candidates obtained in Optimal Pareto Front.

The findings in the current study are summarized in the followings,

1. Some parametric models of both fir-tree and dovetail for the FE analysis in addition to the analytical model were developed. The models were able to generate similar mesh density over contacting surfaces which made the peak contact pressure comparison possible among different samples.
2. It was confirmed that the equivalent punch test in 2D could estimate the peak stress in the dovetail. Also, the coefficient of friction could reduce the peak normal stress in the contact.
3. It was found that the searching domain of the blade and disc attachment, either dovetail and fir-tree, having any of Type-I to IV contact topologies, defined and parametrized in the current study, is a single district (island) space.
4. It was found that applying a high radius curve at the edge of the contact will provide less peak normal contact stress.
5. It was confirmed that the adaptive penalty method based on Euclidean distance is quite effective in reducing the time to find the optimum.
6. An adaptive penalty method based on Latin Hypercube Sampling was proposed to make the adaptive penalty application possible. With this method, the ratio of the feasible space to the whole searching domain could also be estimated.
7. The proposed method was found to be more efficient in a higher dimension complex searching domain.
8. It was confirmed that the Kriging function is successful in emulating the high fidelity function with much less computational cost.
9. To take advantage of the fast calculation of surrogate function in addition to maintain the accuracy of results in an optimization, the Kriging method was embedded into the GA. The results were satisfying.
10. It was found that in order to obtain a robust optimum, the use of the surrogate function is unavoidable.
11. A modified mutation procedure was established to rectify the problem of finding global optimum in a multi-district feasible domain. Nonetheless, the current problem in this study was of type single district feasible domain.
12. It was showed that the simplified analytical model is useful in reducing the time to find the optimum either as a standalone response function or in combination with the FE model.

Appendix A

Parametric models of the blade and disc attachment

An optimization process is generally a high cost process in terms of time due to high number of numerical analysis call back by the algorithm. Increasing the number of parameters needed to define the geometry, dramatically, increases the time for accomplishing of the entire optimization process and makes it harder to converge. On one hand a designer should select those parameters to which the objective function is less sensitive and consider proper constant values for them. Moreover, there are some parameters in the parametric model which should be constant mandated by other phases of a design process. On the other hand, the parameters to which the objective function is expected to be dependent on or to be more sensitive should be left as variable parameters. The number of the variable parameters defines the dimension of an optimization problem. High number of variable parameters means a high dimension domain in which the optimizer should find the optimum in it. In addition to enlarging the domain by additive dimensions, this makes the ratio of feasible space to non-feasible space much smaller. Consequently, the problem becomes two fold, i.e. the domain is larger and the feasible space is smaller, hence, there should be much effort for optimizer to converge. As a result, the selection of variable parameters play an important role in an optimization process.

A.1 Analytical Approach - Simplified Fir-tree

Figure A.1 illustrates a schematic sketch of a blade with a fir-tree in meridional (left) and annulus (right) view. The blade is simplified into three main parts of vane, shank and root. The mass values for the vane and shank are inputs to the analysis.

The fir-tree root height is a function of number of lobs, n_{lobs} as seen in fig. A.2. Hence,

$$H_{fitree} = n_{lobs} \times h_{lob} \times \cos(\gamma)$$

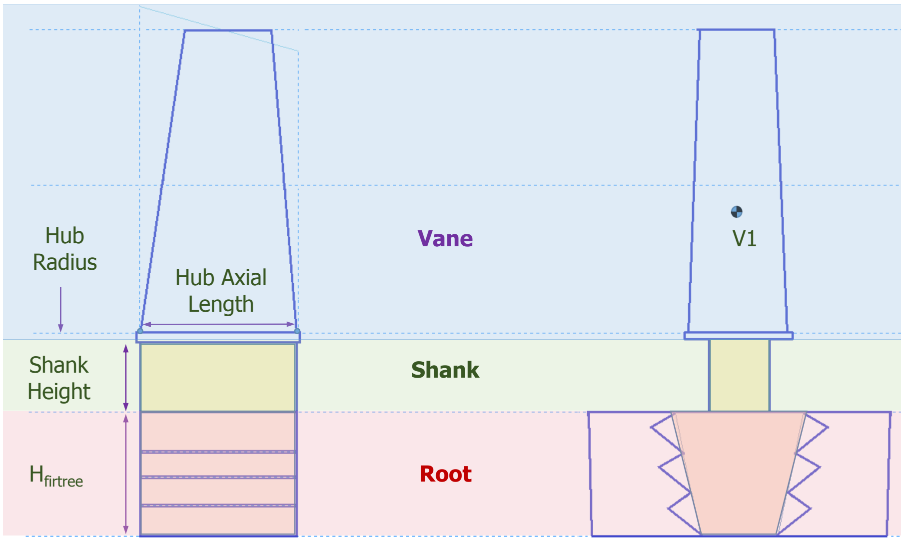

Figure A.1: Schematic sketch of a blade in analytical approach.

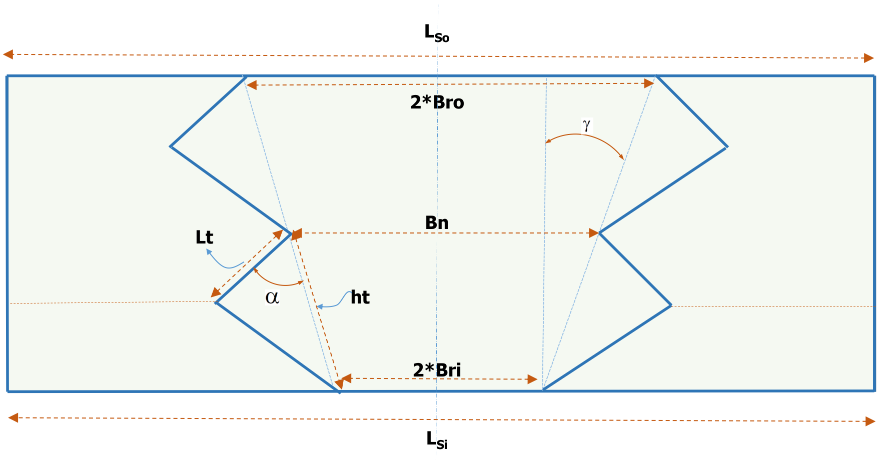

Figure A.2: Schematic sketch of a fir-tree in analytical approach.

Moreover, the length of the segments in outer and inner rim can be calculated as,

$$L_{So} = \frac{2 \times \pi \times (\text{Hub Radius} - \text{Shank Height})}{\text{Number of Blades}}$$
$$L_{So} = \frac{2 \times \pi \times (\text{Hub Radius} - \text{Shank Height} - H_{firtree})}{\text{Number of Blades}}$$

The outer width of the blade root section is,

$$B_{ro} = B_{ri} + H_{firtree} \times \tan(\gamma)$$

where, B_{ri} is given as input to the analysis. The total centrifugal force exerting the hub section of the vane is sum of the centrifugal force of the blade and the shroud mass,

$$F_V = M_V \times \rho_{blade} \times R_{MV} \times \omega^2$$

where, R_{MV} is the radial location of the center of gravity for the vane. The centrifugal forces due to the shank, F_{shank} is also calculated correspondingly. Considering a trapezoidal geometry for the blade root, the central gravity of the blade root is estimated as,

$$CG_{firtree} = \text{Hub Radius} - \text{Shank Height} - H_{firtree} \times \left(\frac{B_{ri}}{(B_{ro} + B_{ri}) + \frac{(B_{ro} - B_{ri})}{3 \times (B_{ro} + B_{ri})}} \right)$$

Consequently, the centrifugal force of the blade root $F_{CFBladeroot}$ is calculated. Figure A.3 illustrates the schematics of center of gravity for a section of the fir-tree between two notches. Assuming the same load carrying for every lob, the total centrifugal force that every contact surface on the fir-tree lob should resist is,

$$F_{bladeTotal} = F_V + F_{shank} + F_{CFBladeroot}$$
$$F_r = F_{bladeTotal} / (2 \times n_{lobs})$$
$$F_N = \frac{F_r}{\sin(\alpha_T - \gamma)} + \mu \times \cos(\alpha_T - \gamma)$$

where, F_N is the normal contact load and F_r is its projection in radial direction. The notch width for the k^{th} notch of the blade is,

$$B_n = 2 \times (B_{ro} - k \times h_T \times \sin(\gamma))$$

The volume of the space between every notch is the enclosed trapezoidal area plus two lobs,

$$V_{lob}^{k} = \left[\frac{(B_n^k + B_n^{k-1})}{2} \times h_T \times \cos(\gamma) + 2 \times A_{lob} \right] \times \text{Rim Axial Length}$$

Hence the centrifugal force due to this mass is,

$$F_{cf}^{k} = V_{lob}^{k} \times \rho_{blade} \times \left[\text{Hub Radius} - \text{Shank}_{\text{Height}} - \left(k - 1 + \frac{1}{2} \right) \times h_T \times \cos(\gamma) \right] \times \omega^2$$

Subsequently, the tensile stress on every section are found,

$$\sigma_{Shank} = \frac{F_V + F_{Shank}}{\mathrm{Shank}_{\mathrm{width}} \times \text{Hub Axial Length}}$$
$$\sigma^k_{bladenotch} = \frac{F^i_{lob}}{B^k_n \times \text{Hub Axial Length}}$$
$$\text{Specific Contact Pressure} = \frac{F_N}{w_T \times \text{Hub Axial Length}}$$

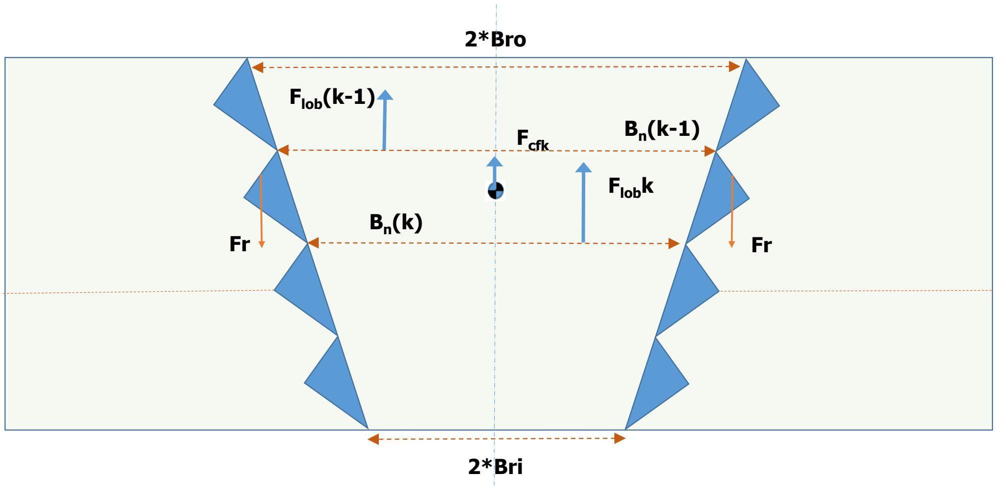

Figure A.3: Schematic sketch of a fir-tree loading in analytical approach.

A.2 FEM Approach - Dovetail Parametric Model

The 2D geometry of the dovetail was parameterized as illustrated in Fig. A.4 and A.5. This model is the most general but thorough geometry of a dovetail. The main feature of this geometry is the two conduct lines a and b which roughly identify the contribution of the blade root, the intermediate space and the disc. The notches on the disk are tangent to these two conduct lines. Point P_{ab} is the origin of the two conduct lines. For dovetail model, this point is fixed so it is considered as a constant parameter. In fact, if P_{ab} is kept far enough from the root section, all the possible geometries could be produced by changing the slope of the two conduct lines parameters α_a and α_b that are variable parameters.

The attachment geometry shape in the blade side can be different from the disc side but there are some relations which interconnect their parameters. For example the curve R_{C1b} can not have a radius less than R_{C1}. Moreover, the curvature of the blade root R_{C1b} can follow the same curvature of the disc to provide a smoother contact profile of stress

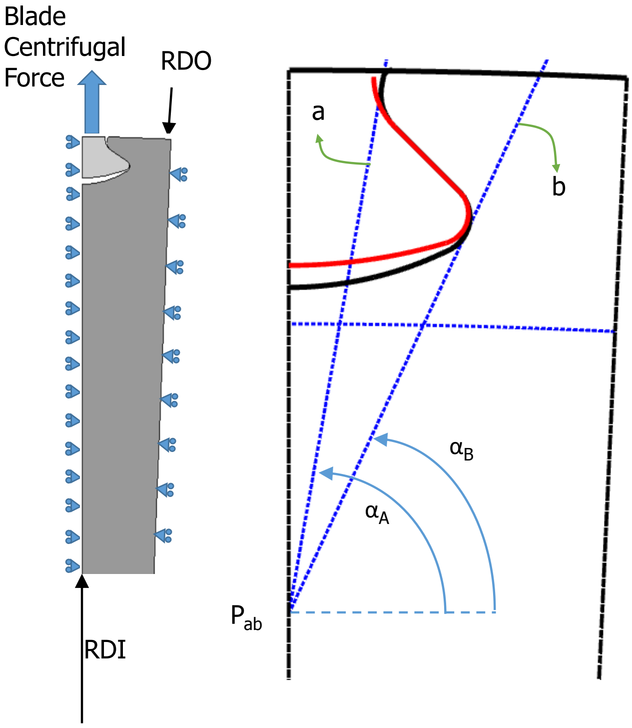

Figure A.4: Parameters definitions Boundary conditions, loadings and conduct lines

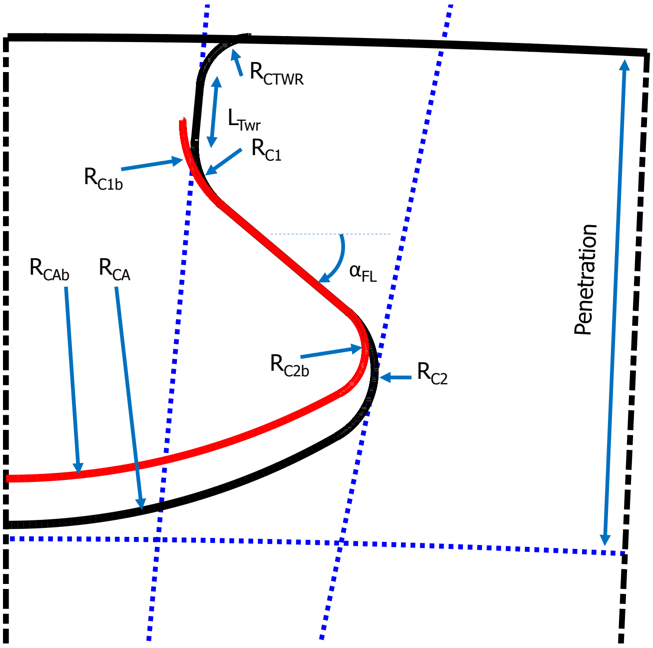

Figure A.5: Detailed Parameters of a dovetail.

in addition to eliminate more variable parameters and consequently, decreasing the computational time for optimization. For assembly reasons although, the blade parameters are defined as a function of the disc parameter as:

$$R_{C1b} = 1.05 \cdot R_{C1} \tag{A.1a}$$

$$R_{C2b} = 0.85 \cdot R_{C2} \tag{A.1b}$$

Moreover, in order to provide enough tolerance for manufacturing reasons and avoiding the interference with the disc groove, the curvature of the blade root lower part is related to the corresponding groove of the disc as below,

$$R_{CAb} = 1.05 \cdot R_{CA} \tag{A.2}$$

All the constant and variable parameters are tabulated in Table A.1. As previously explained some parameters can be derived as a function of other parameters or left as variable parameters to be optimized. It is a matter of time, accuracy and designer decision for selecting one of these options. It is the variable parameters which govern the shape of the blade and disc attachment and by manipulating these variables the optimizer will find the best attachment in terms of objectives.

A.3 FEM Approach - Fir-tree Parametric Model

The same parametric model can be used for generating a fir-tree blade root. Figure A.6 illustrated a parametric model of a fir-tree having four lobs. For the case of a fir-tree, the origin of the two conduct lines a and b are located separately with a reasonable distance from each other. Also, the slope of the two conduct lines are kept equal in order to provide similar contact lines for all lobes. Moreover, for a fir-tree the slope of the non-contact lines, α_{SL}, is an additive variable parameter. Therefore, for a fir-tree, at least eight variable parameters are defined.

Due to the symmetry, just half of the blade and disc section has been illustrated. In this model, the same parameters can be used for generating the shape of the blade as used for the disc but with a tolerance which is inevitable. If there is not any space between upper lob on the blade and the lower lob on the disc, the bending of the lower lobs may affect the upper one. It means that the non-contact line in this case is also a contact line and some normal pressure is endured by this line.

Similar to the dovetail model, the area devoted for the fir-tree attachment is divided into three parts; blade area, lobs or intermediate area and disc area. The role of two major guide lines a and b is more highlighted to segregate these areas as described for the dovetail in previous section. Hence, the slope (α_a and α_b) along with the position of the base of these two guide lines (P_a and P_b) play significant role on the shape determination

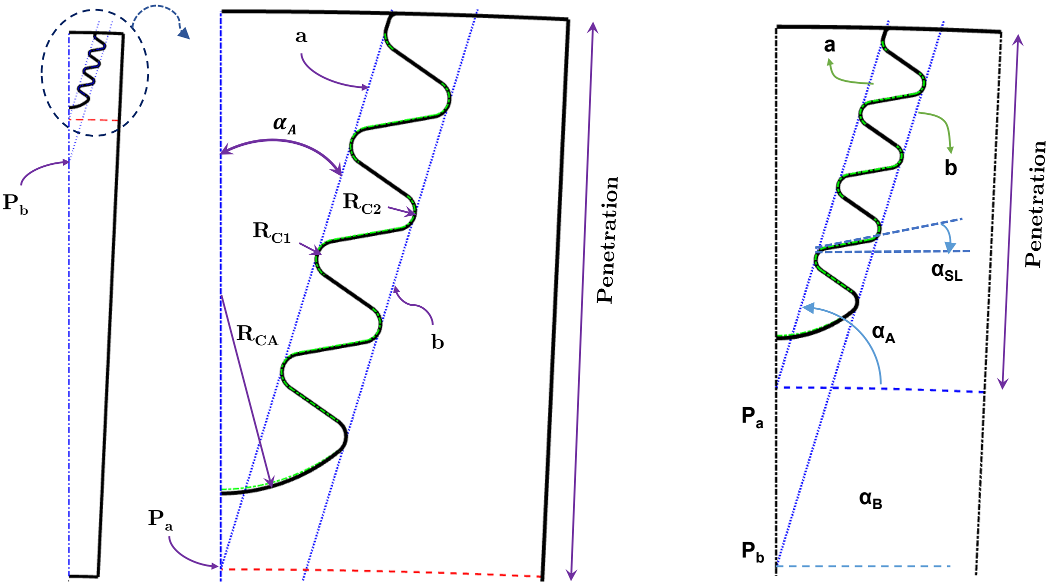

Figure A.6: Parametric model of a fir-tree.

of the fir-tree. Besides, every individual lob shape is defined by four parameters of which two are the slopes of the contact line, α_{FL} (which endure the normal contact pressure) and non-contact line of the lob, α_{SL} and the other two parameters are the radius of the curves (R_{C1} and R_{C2}). The lower part of the fir-tree attachment makes a groove in the disc with the radius of R_{CA}. The maximum radial length of the fir-tree attachment is limited by the parameter *Penetration*. It is common to keep the two parameters α_a and α_b equal in order to have the same contact length for all lobs.

Table A.1: The parameters and variables of the blade and disc attachment

Parameter	Description	Type of variable	Type of Geom
P_{ab}	Radial distance of the origin of conduct lines from the center of the disc	Constant	Dovetail
P_a	Radial distance of the origin of conduct line a to P_b	Variable	Fir-tree
P_b	Radial distance of the origin of conduct line b to center of the disc	Variable	Fir-tree
α_A *	Slope of conduct line a	Variable	Dovetail/Fir-tree
α_B *	Slope of conduct line b	Variable	Dovetail/Fir-tree
R_{CTWR}	Radius of the upper fillet on disc	Variable/Constant	Dovetail/Fir-tree
L_{Twr}	Length of the upper part of the disc	Variable/constant	Dovetail/Fir-tree
R_{C1}	Radius of the upper contact curve on disc	Variable	Dovetail/Fir-tree
R_{C2}	Radius of the lower contact curve on disc	Variable	Dovetail/Fir-tree
α_{FL}	Contact line slope (positive)	Variable	Dovetail/Fir-tree
α_{SL}	Non-Contact line slope (positive)	Variable	Fir-tree
R_{CA}	Radius of the cavity for Disc	Variable	Dovetail/Fir-tree
R_{CAb}	Radius of the lower most curve of the Blade	Variable/Derived	Dovetail/Fir-tree
R_{C1b}	Radius of the blade upper contact curve	Variable/Derived	Dovetail/Fir-tree
R_{C2b}	Radius of the blade lower contact curve	Variable/Derived	Dovetail/Fir-tree
NB	Total number of the blades	Constant	Dovetail/Fir-tree
R_{DO}	External radius of the disc	Constant	Dovetail/Fir-tree
R_{DI}	Internal Radius of the disc	Constant	Dovetail/Fir-tree
Penetration	The radial permitted space used for embedding the blade root in the disc	Constant/variable	Dovetail/Fir-tree
*	In case of same lob size in fir-tree:	$\alpha_A = \alpha_B = \alpha_{AB}$	

Appendix B

Parametric Model Development Details

B.1 Geometric Calculations

The parametric model of the dovetail or fir-tree is developed in this appendix in details. The topology of the contact described here is the simple one composed of a straight line embedded within two curvature. Figure B.1 illustrates a schematic drawing of a dovetail. Every fillet and notch is created by a circle.

Parametric Model generation

In order to obtain the coordinate the contact line, knowing the positions of points B and C_1, in addition to have α_E, α_B, R_1 and R_2, the position of points E, F and C_2 can be obtained (Fig. B.2). Point E is easily found by,

$$x_E = x_{C1} - R_1 \sin(\alpha_E)$$
$$y_E = y_{C1} - R_1 \cos(\alpha_E)$$

To Find C$_2$, firstly, a line parallel to line EF is drawn downward with a distance R_2 from line EF which we name it E', hence,

$$\text{line } E : (y - y_E) = -\tan(\alpha_E) \times (x - x_E)$$
$$\text{line } E' : (y - y_E) = -\tan(\alpha_E) \times (x + \frac{R_2}{\sin(\alpha_E)} - x_E)$$

Then, another line parallel to the guide line B with a distance R_2 to the left is drawn. Therefore,

$$\text{line } B : (y - y_B) = -\tan(\alpha_B) \times (x - x_B)$$
$$\text{line } B' : (y - y_B) = -\tan(\alpha_B) \times (x + \frac{R_2}{\sin(\alpha_B)} - x_B)$$

The point C_2 is the cross point of lines E' and B' as,

$$(y - y_E) = -\tan(\alpha_E) \times (x + \frac{R_2}{\sin(\alpha_E)} - x_E)$$
$$(y - y_B) = -\tan(\alpha_B) \times (x + \frac{R_2}{\sin(\alpha_B)} - x_B)$$

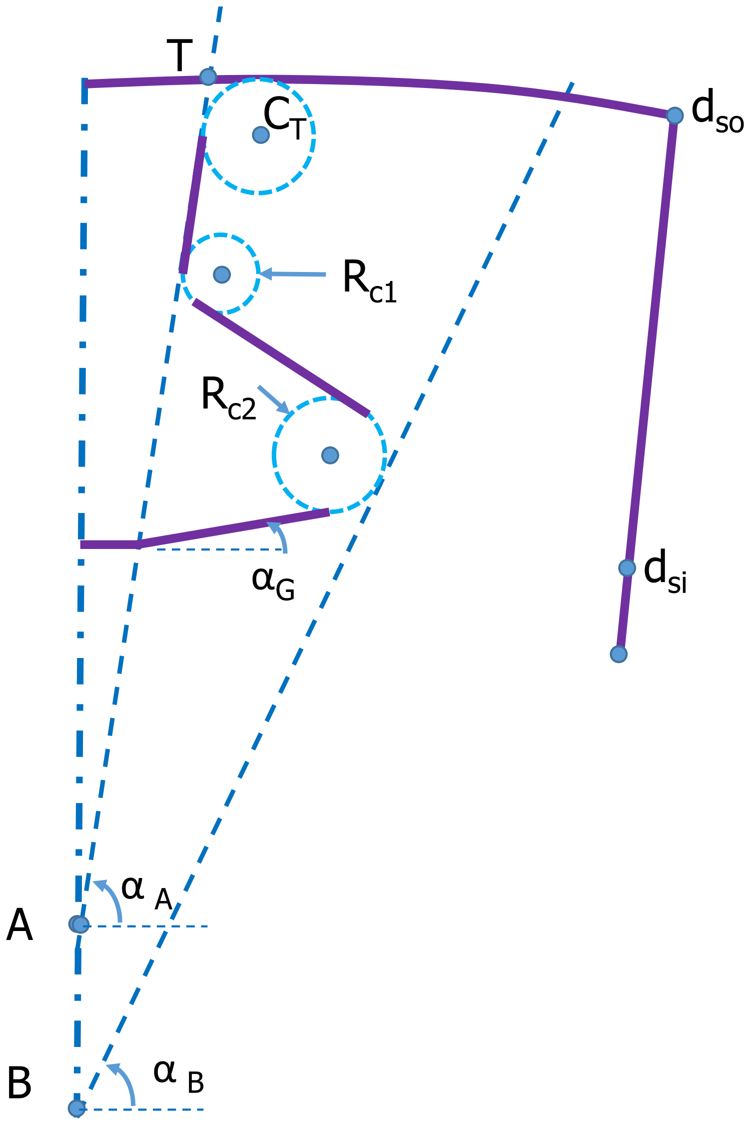

Figure B.1: Dovetail Parametric Model generation.

By solving the previous system of equations point C_2 is determined,

$$x_{C_2} = \frac{y_E - y_B + R_2 \times (\frac{-\tan(\alpha_E)}{\sin(\alpha_E)} - \frac{\tan(\alpha_B)}{\sin(\alpha_B)}) + \tan(\alpha_B)x_B + \tan(\alpha_E)x_E}{\tan(\alpha_B) + \tan(\alpha_E)}$$

$$y_{C_2} = \frac{-\tan(\alpha_B)\tan(\alpha_E)}{\tan(\alpha_B) + \tan(\alpha_E)} \left[R_2 (\frac{1}{\sin(\alpha_E)} - \frac{1}{\sin(\alpha_B)}) + x_B - x_E - \frac{y_E}{\tan(\alpha_E)} - \frac{y_B}{\tan(\alpha_B)} \right]$$

The point F is found knowing that this point is the perpendicular intersection of radius with line EF,

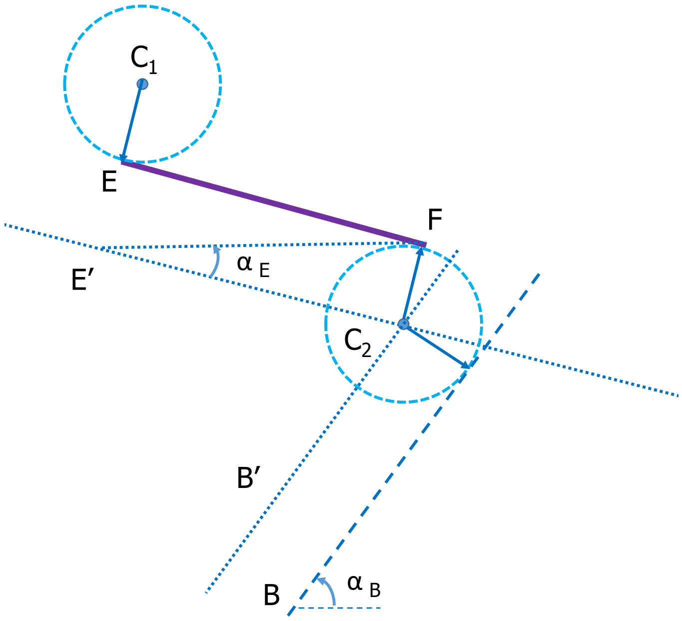

Figure B.2: Contact line coordinate calculation.

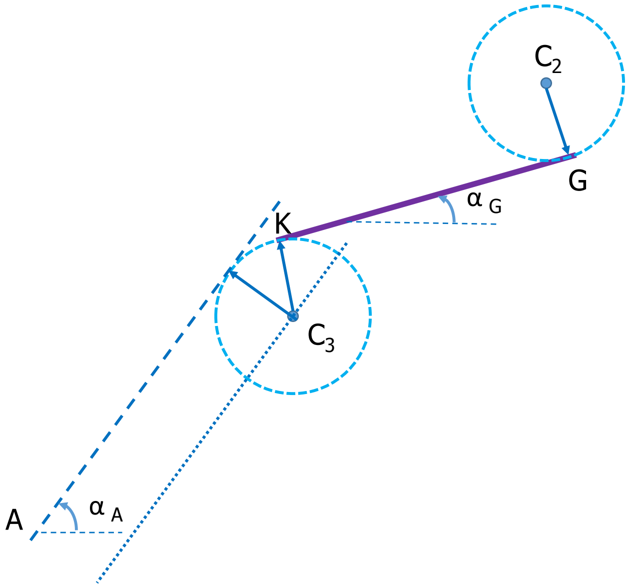

Figure B.3: Non-Contact line coordinate calculation.

$$(y - Y_{C_2}) = \frac{1}{\tan(\alpha_E)} \times (x - x_{C_2})$$

$$(y - Y_E) = -\tan(\alpha_E) \times (x - x_E)$$

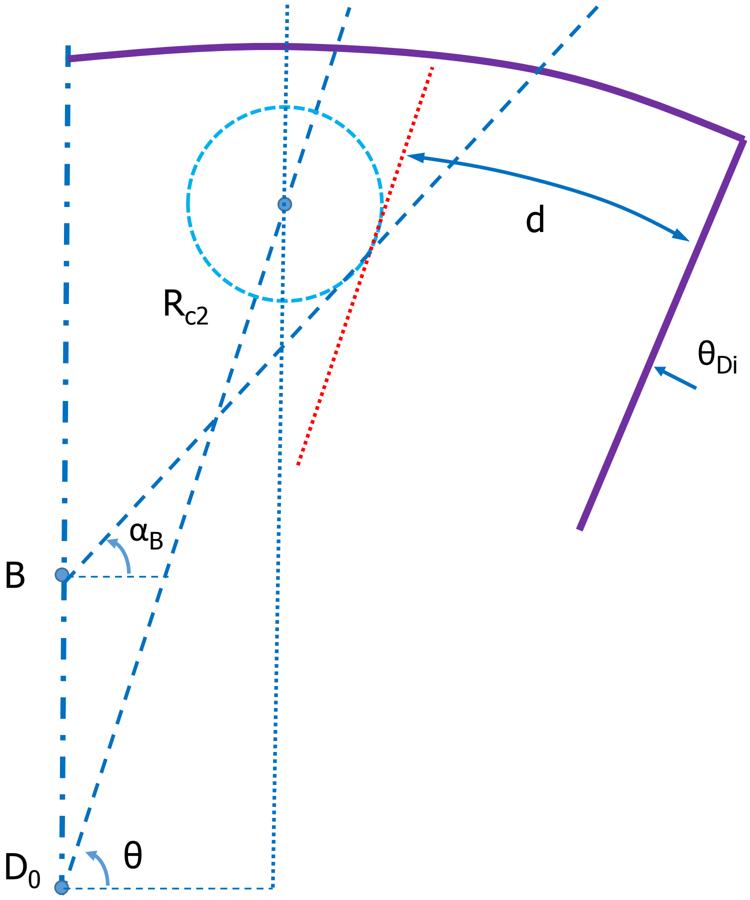

Figure B.4: Disc neck length calculation.

Hence, the point F is obtained,

$$x_F = \frac{-\tan\alpha_E x_E - \frac{x_{C_2}}{\tan\alpha_E} + y_{C_2} - y_E}{-\tan\alpha_E - \frac{1}{\tan\alpha_E}}$$

$$y_F = \frac{x_{C_2} - \frac{y_E}{Tan\alpha_E} - \tan\alpha_E y_{C_2} - x_E}{-\tan\alpha_E - \frac{1}{\tan\alpha_E}}$$

To determine the location of non-contact line (Fig. B.3), knowing the points A and C_2 and the values of R_2, R_3, α_G and α_A, the points G, K and C_3 are found (Fig. B.3). Point G is simply found as,

$$x_G = x_{C2} - R_2 \sin(\alpha_G)$$

$$y_G = y_{C2} - R_2 \cos(\alpha_G)$$

The system of equations below should be solved to find the point C_3,

$$(y - y_G) = \tan(\alpha_G) \times (x + \frac{R_3}{\sin(\alpha_G)} - x_G)$$

$$(y - y_A) = \tan(\alpha_A) \times (x + \frac{R_3}{\sin(\alpha_A)} - x_A)$$

The location of point K is found knowing the location of point C_3,

$$x_K = x_{C3} - R_3 \sin(\alpha_G)$$

$$y_K = y_{C3} - R_3 \cos(\alpha_G)$$

The rest of points are calculated similarly. Moreover, to obtain the average tensile stress on every notch in the disc the length of neck on every notch should be find. As seen in Fig. B.4 the length d is demanded. This length is a part of curve determined as below,

$$d = l - R_C$$

$$l = 2\pi R \frac{\theta - \theta_{Di}}{360}$$

$$\theta = \arctan\left(\frac{y_C - y_{D_0}}{x_C}\right)$$

$$R = \sqrt{x_C^2 + (y_C - y_{D_0})^2}$$

B.2 Stiffness Calculation

The fir-tree attachment is simplified as shown in Fig. B.5. As seen, the attachment can be simplified with a system of springs.

Now the bending stiffness of every lob of the fir-tree should be calculated. First, considering a single lob of the fir-tree illustrated in Fig. B.6 it is shown that the base of the lob has the height of H and its longitude is L.

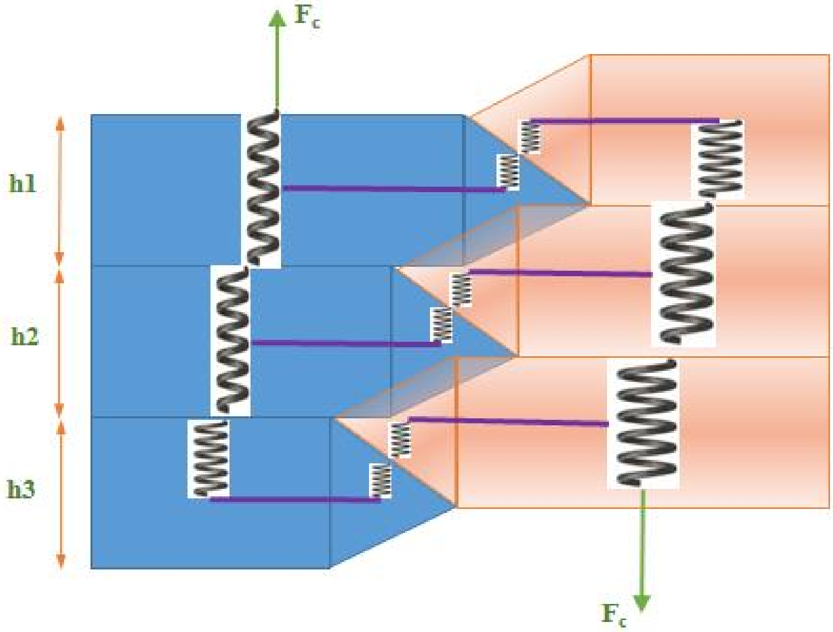

Figure B.5: Simplified fir-tree attachment.

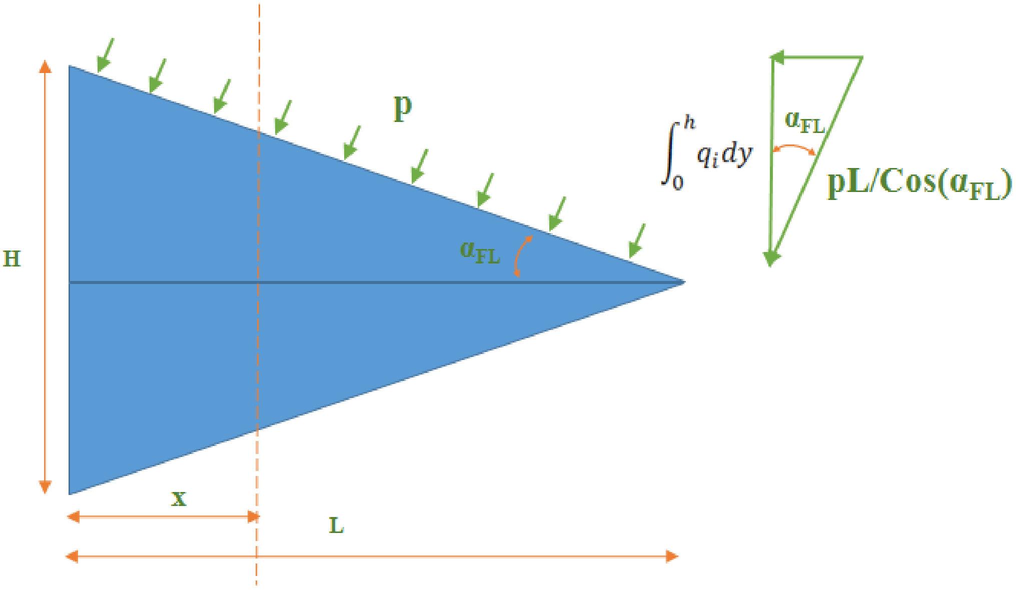

Figure B.6: Single lob of a fir-tree under uniform contact load.

Assuming the same contact load on every lob,

$$p = \frac{F_C L}{3}$$

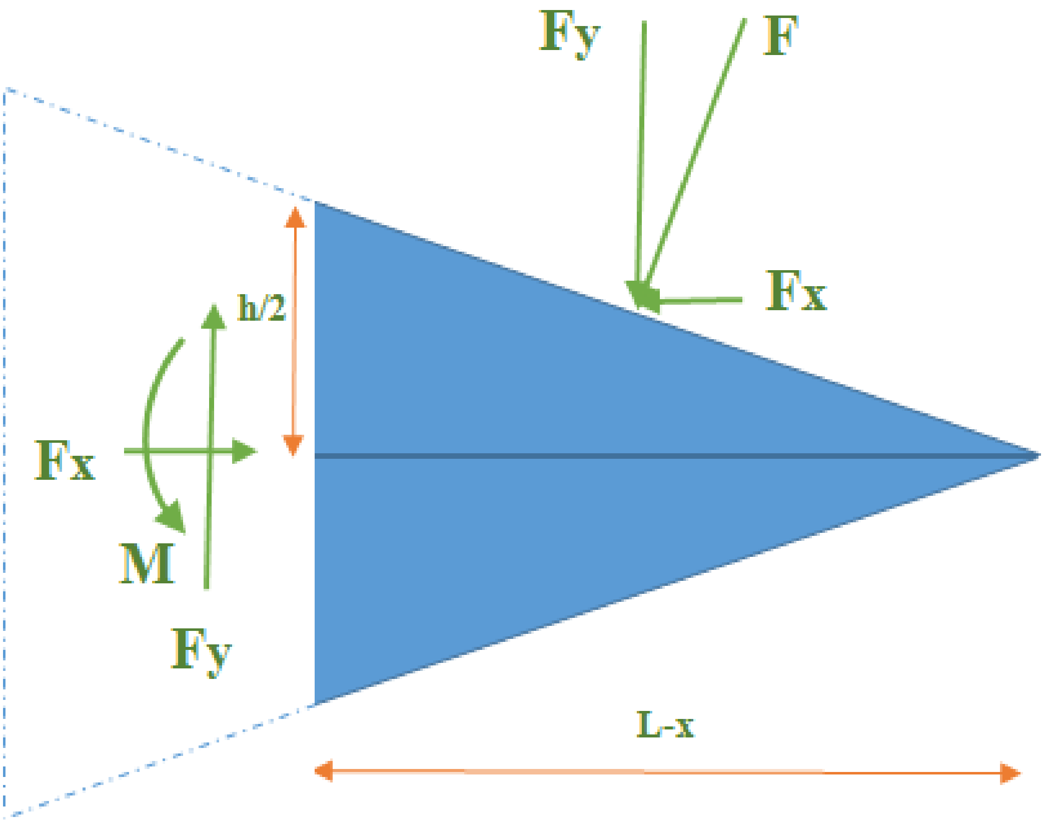

Figure B.7: Free body diagram of a single lob.

In order to calculate the bending deflection of the lob according to Euler-Bernoulli beam theory a free body diagram of the lob is illustrated in Fig. B.7. Hence,

$$
\begin{aligned}
h &= H\left(1-\frac{x}{L}\right)\\
F &= \frac{p(L-x)}{\cos(\alpha)}\\
F_x &= p\frac{h}{2} = p\frac{H}{2}(1-\frac{x}{L})\\
F_y &= p(L-x)\\
M &= F_y\frac{(L-x)}{2} - F_x\frac{h}{4}\\
I_x &= \frac{1}{12}bH^3\left(1-\frac{x}{L}\right)^3\\
y'' &= \frac{M}{EI_x}
\end{aligned}
$$

Considering fully constrained boundary condition for the base of the lob we have $y\prime = 0$ and $y = 0$ at $x = 0$. Solving above equations together results the deflection of the lob in terms of P,H,E,b and x which is the longitudinal location of interested point. Finally, the equivalent bending stiffness would be,

$$K = \frac{PL}{y} = -\frac{2bEH^3}{3(H^2-4L^2)((L-x)\log(1-\frac{x}{L})+x)}$$

In addition to the lob the body of the attachment (the rectangular shape in Fig. B.8) is also simulated with a spring. Every section of the attachment body is divided into two parts separated by mid-line as illustrated in Fig. B.8.

The tensile stiffness of the body is obtained as,

$$KB_i = \frac{E_BA_i}{h_i}$$

Subsequently, the system of springs illustrated in Fig. B.9 should be solved in order to predict the load sharing on contacts. Hence, to obtain the lateral displacement of every point in Fig. B.9 and subsequently obtaining the load sharing over every lob of the

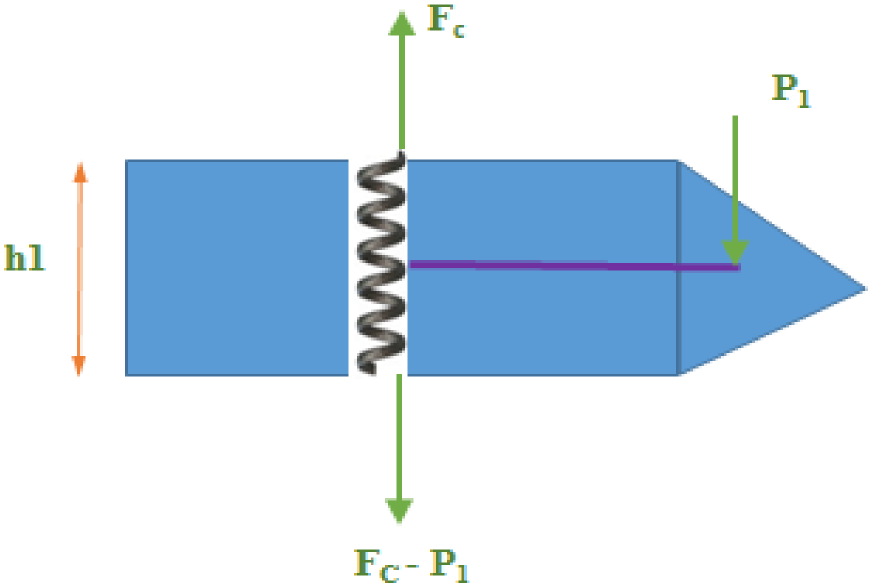

Figure B.8: Free body diagram of a single lob in Fig. B.5.

fir-tree, the matrix equation below should be solved,

$$\left\{\begin{matrix} KB1 & -KB1 & 0 & 0 & 0 & 0 & 0 & 0 \\ -KB1 & KB1+KT1+KB2 & -KB2 & 0 & -KT1 & 0 & 0 & 0 \\ 0 & -KB2 & KB2+KT2+KB3 & -KB3 & 0 & -KT2 & 0 & 0 \\ 0 & 0 & -KB3 & KB3+KT3 & 0 & 0 & -KT3 & 0 \\ 0 & -KT1 & 0 & 0 & KT1+KD1 & -KD1 & 0 & 0 \\ 0 & 0 & -KT2 & 0 & -KD1 & KD1+KT2+KD2 & -KD2 & 0 \\ 0 & 0 & 0 & -KT3 & 0 & -KD2 & KD2+KT3+KD3 & -KD3 \\ 0 & 0 & 0 & 0 & 0 & 0 & KD3 & -KD3 \end{matrix}\right\}$$

$$\times \left\{\begin{matrix} \delta_{b0} \\ \delta_{b1} \\ \delta_{b2} \\ \delta_{b3} \\ \delta_{d1} \\ \delta_{d2} \\ \delta_{d3} \\ \delta_{d0} \end{matrix}\right\} = \left\{\begin{matrix} F_C \\ 0 \\ 0 \\ 0 \\ 0 \\ 0 \\ 0 \\ F_C \end{matrix}\right\}$$

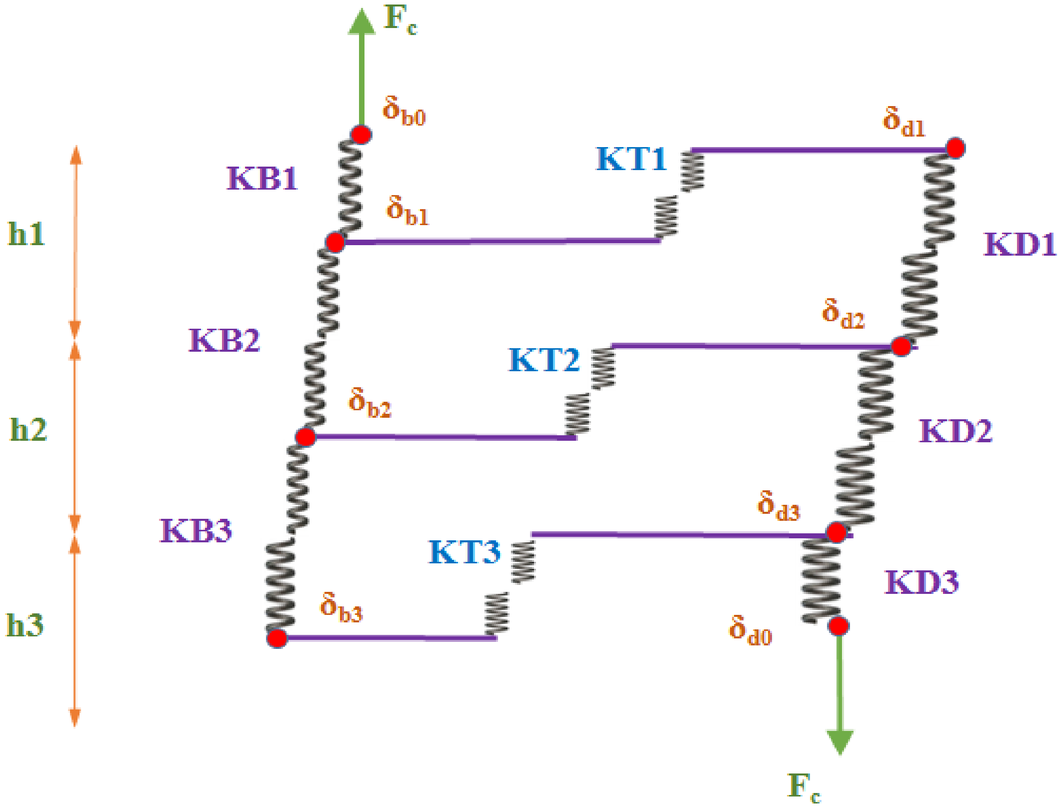

Figure B.9: Fir-tree equivalent system of springs.

Appendix C

APDL and MATLAB Flow Charts for Dovetail parametric model

In this appendix the Flow charts developed with APDL and MATLAB to construct and analysis the FE 2D dovetail parametric model is given.

C.1 MATLAB Function - Geometry development

Figure C.1 illustrates the flow chart of construction of 2d geometry. The output would be an index determining if the input vector define a geometric feasible shape or not.

C.2 MATLAB Function - Decision Maker

Figure C.2 illustrates the flow chart of the main core of the decision making.

C.3 APDL Flow Chart

Figure C.3 illustrates the flow chart of APDL model preparation, meshing and analysis.

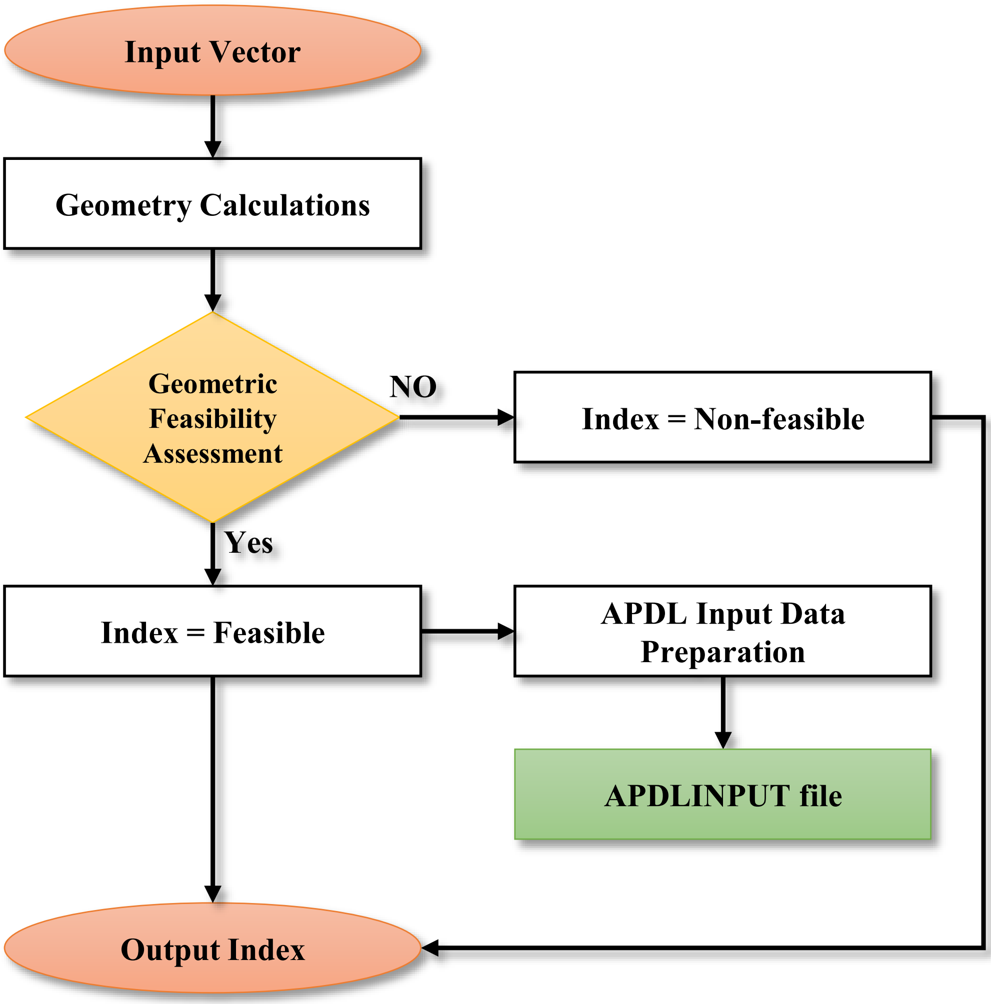

Figure C.1: Geometry Developer Flow Chart.

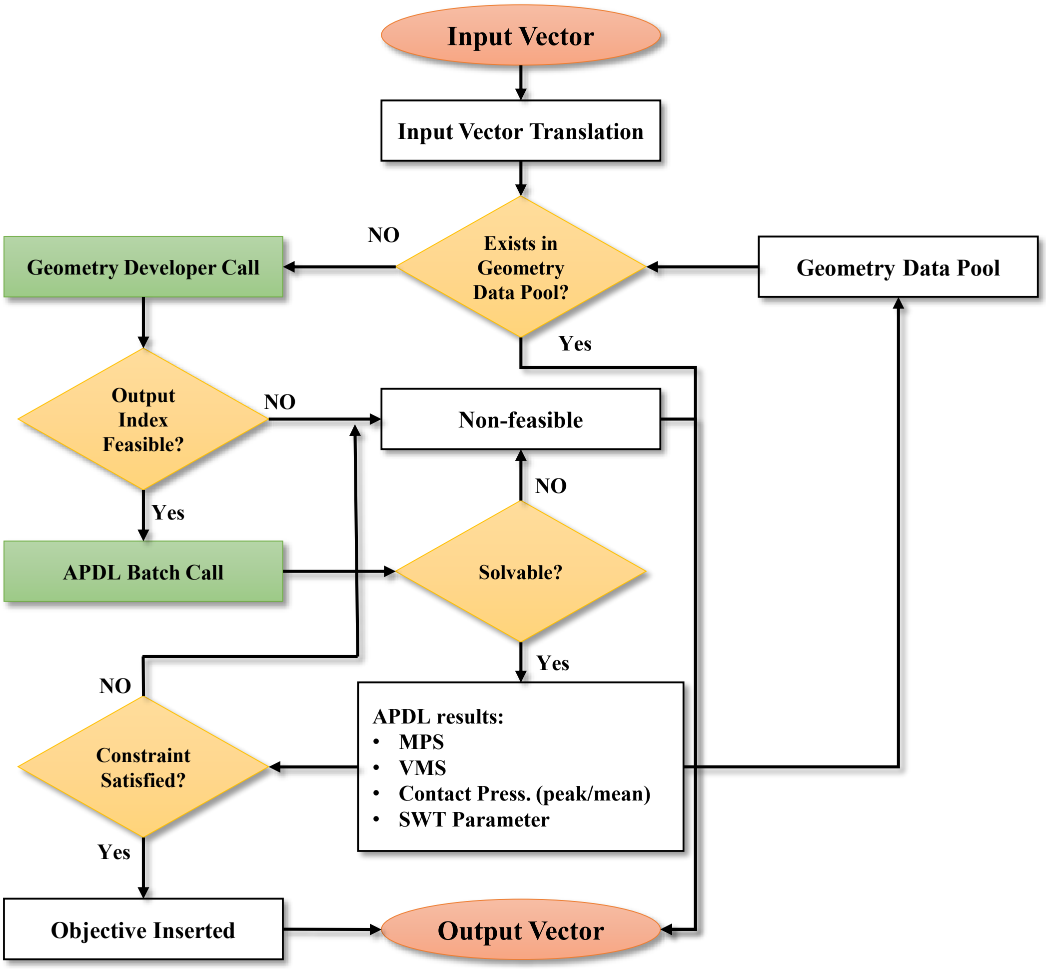

Figure C.2: Decision Maker Flow Chart.

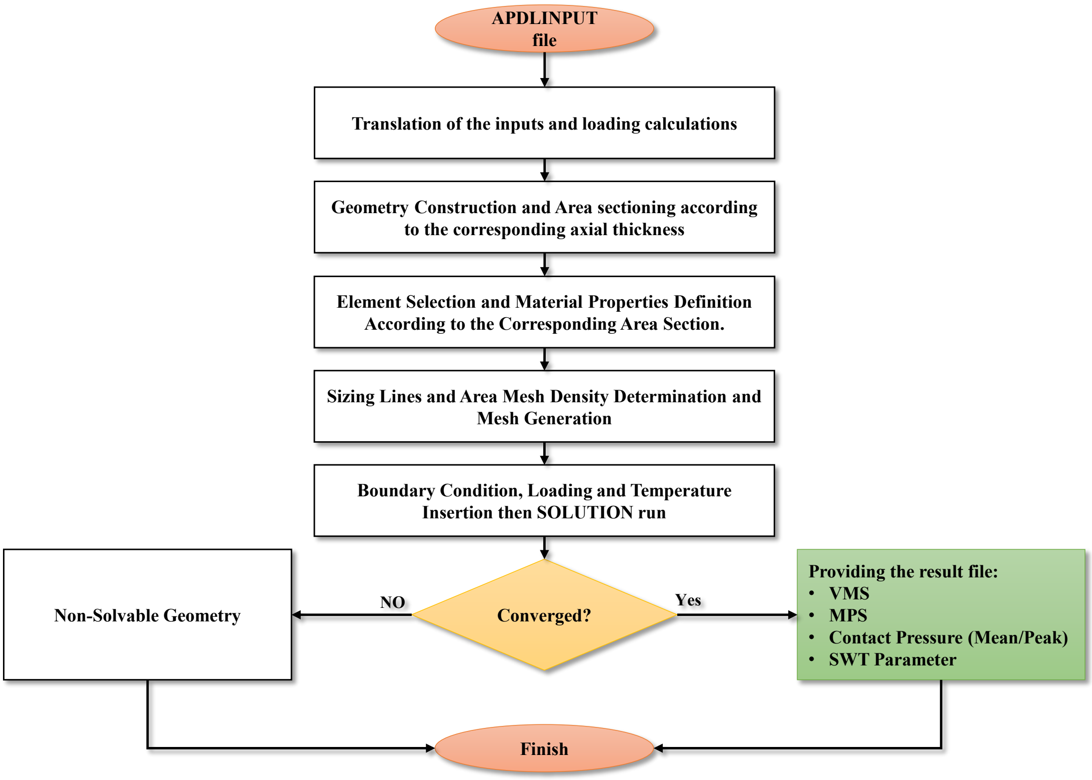

Figure C.3: APDL Batch FE Analysis Flow Chart.

Appendix D

Optimization by Genetic Algorithm

In general, optimization is a systematic search through input values within an allowable set (searching domain) to find the minimum or maximum of a response function. Three main conventional search methods are [36],

1. Calculus based
2. Enumerative
3. Random search

Calculus based is divided into indirect and direct types. The indirect method utilizes the gradient of the objective function in order to find the local extrema. In this method the search seeks the points in which the slips are zero in all directions. The direct type as in the "hill climbing" method the algorithm climbs the function in the steepest permissible direction to find the local optimum. The enumerative methods is the most likely kind similar to human way of searching just like finding an extrema in a short list. Its idea is to find the best objective value by searching all possible values one by one. In the random search which is divided into two classes of "Las Vegas algorithm" and "Monte Carlo Algorithm", the algorithm tries to find the optimum through randomly selected points in the searching domain. In a long run this method has no advantage over the enumerative one. The problem raises with all the conventional methods of optimization is that they all rely on a continuous ideal constrained and derivable objective functions but the real world of optimization problems are fraught with non-feasibility, discontinuity and multi dimensionality.

D.1 Genetic Algorithm

Years after the first introduction of a primitive “learning machine” by English computer scientist, mathematician, logician, cryptanalyst, philosopher, and theoretical biologist Alan Turing, various types of genius algorithms has been developed to solve different problems. John Holland firstly developed the genetic algorithm which was an important discovery in the field of artificial intelligence science. The genetic algorithm is a method for solving optimization problems that is inspired by Charles Darwin's theory of natural selection, the process that provides biological evolution [64]. In this method the algorithm deals with the code transform of the parameters not the parameters directly. It means that the parameters are coded into some genes forming a chromosome. Also, the GA apply random selection a population of points hence is categorized as a randomized algorithm. This method repeatedly modifies a population of individual solutions. At each step, the genetic algorithm selects individuals at random from the current population to be parents and uses them produce the children for the next generation. Over successive generations, the population "evolves" toward an optimal solution. Genetic algorithm uses three main types of rules at each step to create the next generation from the current population:

- Selection rules select the individuals, called parents that contribute to the population at the next generation.
- Crossover combine two parents to form children for the next generation.
- Mutation apply random changes to individual parents to form children.

D.1.1 Selection

In this phase of the process, the individuals are selected in the population to be mated for generation of offspring for next generation. The main idea is that the fittest individuals are hoped to provide offspring with higher fitness. Hence, the probability for selection of the fittest individuals as parents are higher. There are some different methods for selection of parents,

- Roulette Wheel
- Stochastic Universal Sampling
- Sigma Scaling
- Elitism
- Boltzmann selection
- Rank selection
- Tournament selection
- Steady state selection

Here, a brief description of each method is explained.

Roulette Wheel

The selection of individual is based on the probability of the individual fitness value divided by the average fitness of the population. In this method every individual is assigned a slice of a circular roulette wheel proportional to its fitness value. To obtain a population of N individual the wheel is rotated N times. When the wheel stops the individual under the wheel pointer is selected as a parent for the next generation.

Stochastic Universal Sampling

In the method of roulette wheel there is a chance that the all offspring are generated from the worst individual by rotating the wheel. The stochastic universal sampling introduced by James Baker (1987) [8], rectified such problem by proposing a modification in that instead of rotating the wheel N times rotate once and select through N number of pointers which are equally spaced.

Sigma Scaling

In the two methods of roulette wheel and stochastic universal sampling the premature convergence may happen. Because when the generation converge to some fitter individuals the individuals are very similar and the variance is very low. This makes the halt of the evolution. In the sigma scaling introduced by Forrest 1985, the individual's expected fitness value is a function of its fitness, population mean and the standard deviation. Therefore, in the beginning of an optimization when the standard deviation is high, the fitness of the fitter individuals are also high comparing to the mean fitness hence the function provides a lower probability for the fitter individuals preventing the premature convergence. On the other hand, when run proceeds, the population is more converged and the standard deviation is lower but the difference of the fitter individual to the mean is also low, hence, the function generates a fitness value in a way that allows evolution to continue.

Elitism

In this method which was introduced by Kenneth De Jong (1975) [47], during the transfer to next generation a number of fittest individuals are retained in hope that the next generation would provide fitter offspring (Fig. D.1).

Boltzmann selection

The previous method provided a constant balancing of the fitness value allocation but in Boltzmann selection a continuous varying temperature controls the rate of balancing of the fitness value allocation [59]. The effect is such that in the initial of the run every

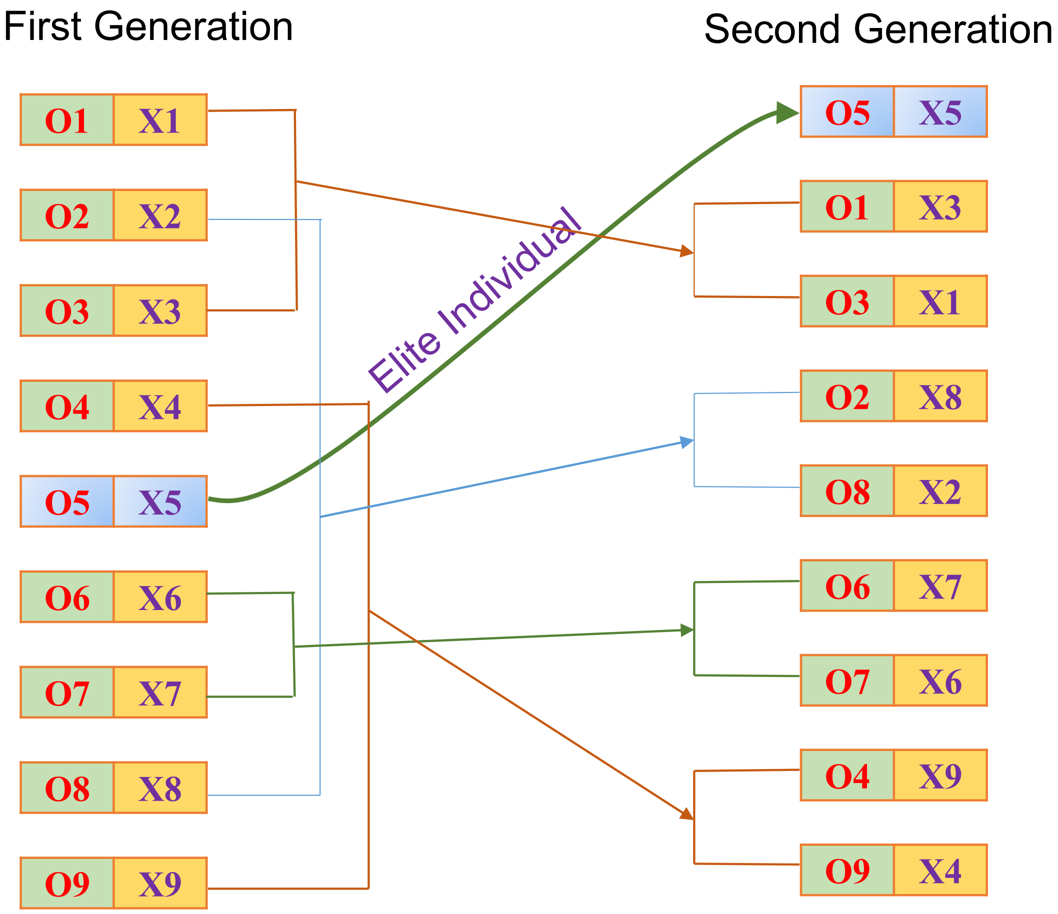

Figure D.1: The schematic of elitism in genetic algorithm.

individual has some acceptable probability of reproduction but when run proceeds the fitter individuals are more focused while appropriate degree of diversity is maintained.

Rank selection

In this method the individuals are allocated the selection probability according to their ranking of their fitness rather than their absolute fitness value. This selection type prevents high number of offspring from small group of highly fit individuals yet maintains the selection priority over more converged run.

Tournament selection

In this method two individuals are selected at a time from the population in a random selection then one is selected randomly to be parent for next generation.

Steady state selection

Opposite the other selection methods in which all or at least a major part of the population is renewed in every generation, in this method, a small fraction of population is replaced by new individuals in each generation.

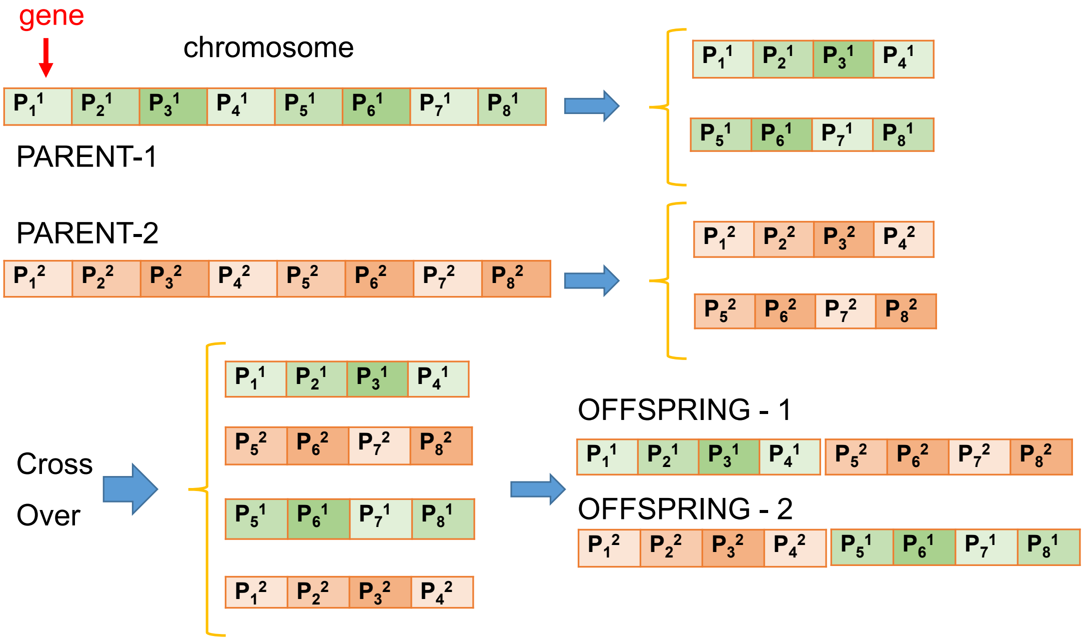

Figure D.2: The schematic of Crossover in genetic algorithm.

D.1.2 Crossover

The crossover is the most identical feature of the genetic algorithm. This is a process of developing offspring from parents. As exists in the nature the genetic components of a pair of parents mix to generate offspring. In a single crossover (D.2), a position is chosen in the input vector (chromosome) of parents and the input vectors are divided into parts in that selected position then the parts are swapped to form two new input vectors (offspring). There are a number of types of crossover such as one point crossover, *N*-Point crossover, segmented crossover, Uniform crossover and shuffle crossover.

D.1.3 Mutation

The last operation in the genetic algorithm applied to the new population in an iteration is the mutation which maintain the diversity of the samples and protect the algorithm in stocking in a local optima. It is a random deformation of the smallest element of an individual chromosome. The resultant solution may be different entirely from the original one (Fig. D.3). In this phase of the algorithm every gen has assigned a predefined probability to be changed with a new gen.

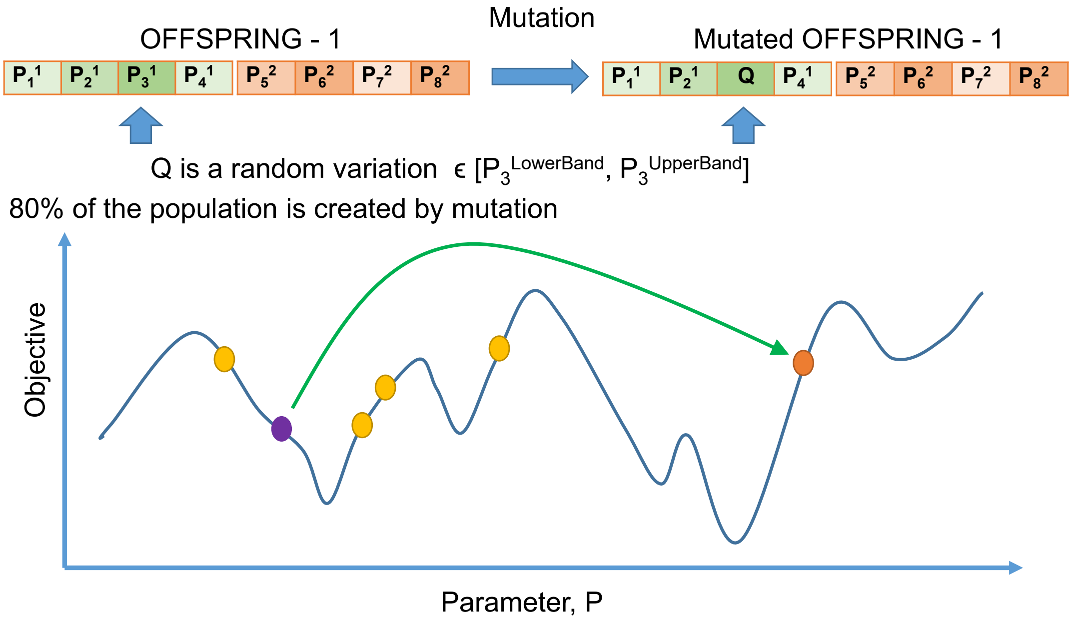

Figure D.3: The schematic of Mutation in genetic algorithm.

D.2 The Traveling Salesman Problem (TSP)

TSP is the most famous and practical problem to be used as a benchmark to optimization algorithms such as genetic algorithms, simulated annealing, Tabu search, ant colony optimization, river formation dynamics and the cross entropy method. Moreover, one may find an analogy between this problem and the case in the current study in the fact that the high number of trails for brute-force solution is not affordable for a computer to solve. The travelling salesman problem (TSP) asks the following question: Given a list of cities and the geographical location of cities, what would be the shortest possible distance that visits each city just once and returns to the origin city?

Although, the crossover method used for this problem due to permutation is rather different from the current case under investigation but the principals of the algorithm is the same. Hence, the evaluation of this problem can be a validation for the algorithm.

D.2.1 TSP evaluation results:

For evaluation the location of a number of cities are given to both genetic algorithm and brutal-force method. In the direct search (brutal-force) method all possible solutions

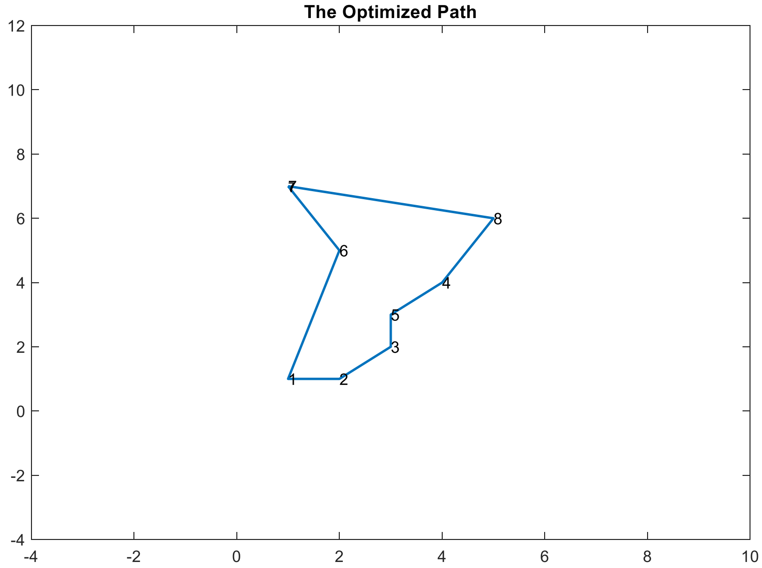

Figure D.4: The Optimum path for 8 cities.

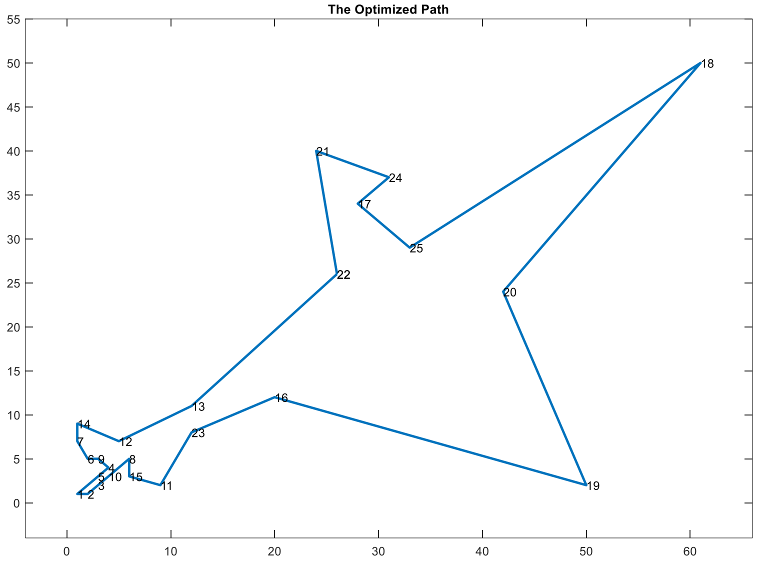

Figure D.5: The Optimum path for 25 cities.

were found one be one hence the optimum is the definite optimum of the problem. As the first trail, eight cities were given to the algorithm by defining a vector of two for each city representing its location in x-y Cartesian coordinate. The time to perform the Brutal-force solution was 10.89 seconds and the optimum distance distance found was 18.8088, while the GA code found exactly the same value just in 0.121544 seconds. Figure D.4 shows the graphical illustration of the solution found for eight cities

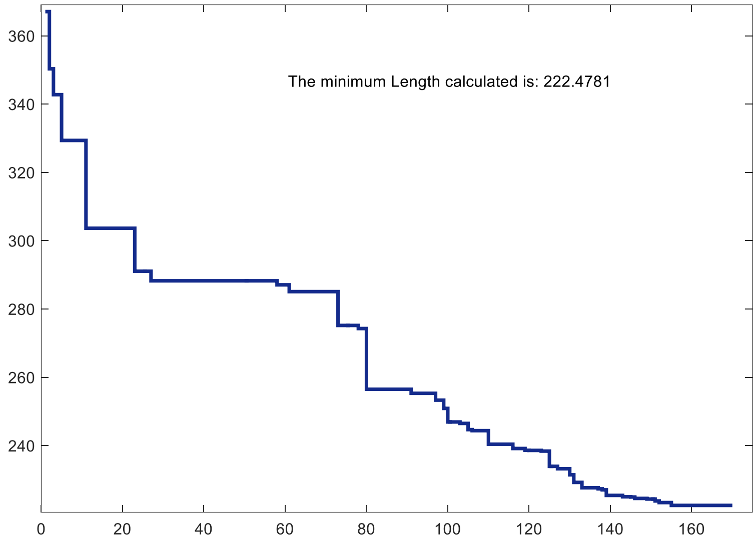

Figure D.6: The Convergence to find Optimum path for 25 cities.

For 9 cities the direct solution took 280.23 seconds to find the optimum distance value of 19.2521, comparing to 0.145042 seconds for GA to find the same optimum value. If one increase the number of cities the time for direct solution would roughly be calculated as,

$$\text{Computational Time} = \frac{(\text{number of cities})!}{9!} \times 280.23 \text{ (seconds)} \tag{D.1}$$

For example, for 25 cities it will take 11978357557436734464000 seconds for direct solution, while the GA found the optimum solution just in 1.003382 seconds. The graphical illustration of the cities is in fig. D.5 and the convergence of the solution is illustrated in Figure D.6.

D.3 Punch Test Problem

Stepping toward the problem in the current study, a punch test has been taken under investigation for optimization. A puncher comprises of a flat surface in the contact area in addition to curved edges with fixed radius.

The optimization problem is to find the best R to have the least peak stress provided the lateral width of the puncher is maintained with the same value. This is a simulation of the contact for the blade root as the main goal is to avoid high peak stress while maintaining the same contact span in the blade root. So, in this problem there is just one variable parameter. In this case, the total lateral width of the puncher (L) is constant and equal to 3 mm, a=L-R, the total load is $P = 721$ [N/mm] and R is examined limited to the bound of [0.2,1.0] mm.

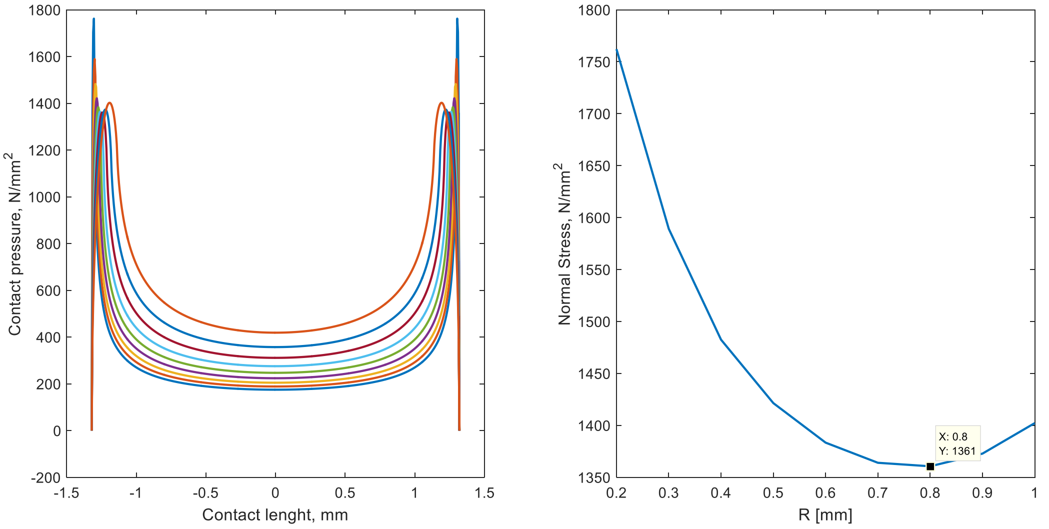

Figure D.7: Punch test normal pressure spectrum for different edge radius.

The direct brutal-force solution results with the increment of 0.1 mm are illustrated in fig. D.7. The contour of the normal pressure on the contact is the left graph, while the variation of the peak stress versus R is found in the right graph.

This diagram shows that the minimum (optimum) peak normal stress occur if we have $R = 0.8$. In order to optimize this problem with the help of GA, an encoding of the input R should be performed. To do this, a series of chromosome should be defined which are all unique and also their genes represents theirs characteristics i.e. by changing the genes, another number (R) should be developed which stands in the predefined range. A binary encoding has been used to provide the input vector of the optimization. The GA algorithm could find the optimum in $R=0.7763$ (mm) less than 0.2 seconds. The results were perfectly conform to the brute-force method.

Appendix E

Surrogate Models and Sampling Methods

E.1 Surrogate Models

Surrogates have been interesting models to many scientists in various disciplines because of their capability to predict the black box functions in addition to their low calculative costs. There are three types of applications for surrogates. The first class which is the major application of surrogates is to model the target function and predict the outputs. The second type is to predict the objective functions for which no derivatives are available in an optimization process. This type is generally called derivative free optimization (DFO) [81]. The third type is to analyze the feasibility of the design. The surrogate models are developed by two major approaches; the models providing unbiased predictions at the sampled data are known as interpolation models. Some examples for this category are Radial Basis Function (RBF) and Kriging function. The models generated by minimizing the error of prediction are referred to as regression models such as linear regression and support vector regression models.

E.1.1 Linear regression

In a linear regression the prediction function is proposed as below [87],

$$f(\mathbf{X}) = \beta_0 + \sum_{i=1}^{p} x_p \beta_p \tag{E.1}$$

where β is the vector of model parameters and is obtained by minimizing the sum of squared error between prediction and the target function output of the samples (the Euclidean norm),

$$min \, \|\mathbf{X}\beta - \mathbf{y}\|_2^2 \tag{E.2}$$

Where, $\mathbf{X}$ is the matrix of vectors of inputs $\mathbf{x}$ plus a column of unit vector (to handle β_0). An analytical form of solution for the foregoing equation is,

$$\beta = \frac{\mathbf{X}^T \mathbf{y}}{\mathbf{X}^T \mathbf{X}} \tag{E.3}$$

In case of having higher number of variable parameters for the target function respect to the number of sample points, the denominator term of the foregoing equation is singular. Such problem occurs for high dimensional problems. There are two method to address this problem; screening and regularization. Screening or subset selection methods filter out some certain variable parameters which have the least impact on the output. The regularization method adds a penalty term to the error measure of the regression which leads to continuous reduction of the model parameters.

E.1.2 Support vector regression

The Support Vector Regression (SVR) surrogates take the form of weighted sum of basis functions in addition to a constant term [26]. A general form of SVR surrogate is given as,

$$f(\mathbf{X}) = \mu + \sum_{i=1}^{n} \omega^i \psi(\mathbf{X}, X^i) \tag{E.4}$$

Assuming $\psi(.) = \mathbf{X}$, the surrogate can be rewritten as,

$$f(\mathbf{X}) = \mu + \omega^T \mathbf{X} \tag{E.5}$$

Although the form of the surrogate is similar to that of RBF and Kriging but the unknown parameters are obtain in a different way. The unknown parameters μ and ω in the model are obtained by minimizing a mathematical statement given by,

$$\frac{1}{2} \|\omega\|^2 + C \sum_{i=1}^{n} \zeta_i + \zeta_i^\star \tag{E.6}$$

Subject to,

$$\begin{gathered} y_i - \omega x_i - \mu \leq \varepsilon + \zeta_i \\ \omega x_i - y_i + \mu \leq \varepsilon + \zeta_i^\star \\ \zeta_i, \zeta_i^\star \geq 0 \end{gathered}$$

Where, $C > 0$ is the penalized coefficient to tailor the trade off between function flatness and the fitness. This coefficient provides a measure by which the resultant function can tolerate $\pm\varepsilon$ deviation from the output at sample points while keeping the shape of the function flat. The slack variables $\zeta_i, \zeta_i^\star$ ensure handling non-feasibility of the problem. Although, the SVR prediction is fast and accurate, the time required to find the unknown parameters is relatively high.

E.1.3 Radial basis functions

The Radial Basis Functions was first developed by [39]. The general form of Radial basis functions (RBF) is

$$f(x) = \sum_{i=1}^{n} \lambda_i \phi(\|x - x_i\|_2) \tag{E.7}$$

Where, λ is the vector of unknown parameters which can be obtained simply by replacing the left term with the vector of sample point outputs, ϕ is the basis function for which there are a verity of options for selection. Bjoerkman and Holmström [17] have found cubic basis function, $\phi(r) = r^3$, with a linear additive term, a successful one,

$$f(x) = \sum_{i=1}^{n} \lambda_i \phi(\|x - x_i\|_2) + a^T x + b$$

E.1.4 Kriging

This function was firstly proposed by Krige [53] for the field of geostatistics but gained its popularity after being used for design and analysis in computer experiments by Sacks et al. [84]. As a successful example of Kriging application, Rahimidehgolan et al. [77] applied this model in a combination of experimental, numerical simulation and optimization to determine the constants of a model to describe the plastic deformation and damage behavior of ductile material (following by a previous study done using GA by Rahimidehgolan et al. [76]). As they also examined the Polynomial Regression method for their application, they found that the Kriging method provides more accurate results while fewer initial samples are needed for this model. One may find a detailed explanation of Kriging model in [46]. Statistic is the main approach of the Kriging function for interpolating the response over some sample point which are also known as training sample points.

Assuming to have n samples in a searching space of a response function and for the point i, the input vector is $\mathbf{X}^{\mathrm{i}}$. Since the objective function requires k number of input parameters, the input vector is defined as $\mathbf{X}^{\mathrm{i}}$=$(x_1^i, \ldots, x_k^i)$ and the function output is a scalar, $y^{(i)} = y(\mathbf{x}^i)$. A simple form of interpolation over the sample points is to apply a linear regression as,

$$y(\mathbf{X}^i) = \mathbf{X}^{i^T} \beta + \varepsilon^i \tag{E.8}$$

where, β is the vector of regression coefficients and ε is the error of approximation which has a zero mean and also the variance of σ^2. In stochastically techniques, it is assumed that the error is a function of euclidean distance of training samples to the point we are interested in. Therefore, the error terms are function of $\mathbf{X}$ so $\varepsilon^{(i)} = \varepsilon(X^{(i)})$. By applying weighting coefficients to the distance term the correlation between errors is determined as

$$Corr[\varepsilon(\mathbf{X}^i), \varepsilon(\mathbf{X}^j)] = \exp(-\sum_{h=1}^{k} \theta_h |x_h^i - x_h^j|^{p_h}) \tag{E.9}$$

Coefficient θ_h reflects the importance for the variable parameter h. In fact higher θ for an input parameter means that this parameter variation provides higher changes to the output value of the function $y(X)$. Exponent p_h which can take value 1 or 2, determines the smoothness of the response function in dimension h . The value of 2 is considered for the exponent p_k is 2 for all distance terms. As the correlation modeling of the error is so convincing, there is a possibility to unburden the load of prediction for regression terms and delegate it to the error terms. Therefore the the response function is more simplified by replacing the regression terms with a constant β_0,

$$y(\mathbf{X}) = \beta_0 + \varepsilon(X) \tag{E.10}$$

The variance of $y(X)$ is,

$$\sigma^2(\beta_0, \theta, c) = \Big(\frac{1}{n}(\mathbf{y_s} - \beta_0\mathbf{1})^T\mathbf{R}^{(-1)}(\mathbf{y_S} - \beta_0\mathbf{1})\Big) \tag{E.11}$$

where, $\mathbf{1}$ is the unit n-vector and $\mathbf{R}$ is the Correlation Matrix

$$\mathbf{R} = \begin{bmatrix} Corr(\varepsilon^{(1)}, \varepsilon^{(1)}) & Corr(\varepsilon^{(1)}, \varepsilon^{(2)}) & \dots & Corr(\varepsilon^{(1)}, \varepsilon^{(n)}) \\ Corr(\varepsilon^{(2)}, \varepsilon^{(1)}) & Corr(\varepsilon^{(2)}, \varepsilon^{(2)}) & & Corr(\varepsilon^{(2)}, \varepsilon^{(n)}) \\ \vdots & \vdots & \ddots & \vdots \\ Corr(\varepsilon^{(n)}, \varepsilon^{(1)}) & Corr(\varepsilon^{(n)}, \varepsilon^{(2)}) & \dots & Corr(\varepsilon^{(n)}, \varepsilon^{(n)}) \end{bmatrix} \tag{E.12}$$

for which the terms are defined by Eq. E.9. To obtain the constant term β_0, the variance in Eq. E.11 should be minimized. Hence,

$$\begin{gathered} \frac{\partial \sigma^2}{\partial \beta_0} = 0 \\ \frac{\partial((\mathbf{y_s} - \beta_0\mathbf{1})^T\mathbf{R}^{(-1)}(\mathbf{y_S} - \beta_0\mathbf{1}))}{\partial \beta_0} = 0 \end{gathered} \tag{E.13}$$

Therefore, we have,

$$\beta_0 = \frac{\mathbf{1}^T\mathbf{R}^{-1}\mathbf{y_S}}{\mathbf{1}^T\mathbf{R}^{-1}\mathbf{1}} \tag{E.14}$$

The parameters θ_h of the correlation should be selected in a way that the likelihood of the interpolating function is maximized. From statistics, it is known that the joint probability density p of a normal distribution $N(\mu, \sigma^2)$ for a set of n correlated variables y having a covariance matrix **cov** is,

$$p(\mathbf{y} \mid \mu, \sigma^2) = \frac{1}{\sqrt{(2\pi)^n \times \det(\mathbf{cov})}} \exp(-\frac{1}{2}(\mathbf{y} - \mu)\mathbf{cov}^{-1}(\mathbf{y} - \mu)^T) \tag{E.15}$$

Therefor, for the function in E.10 assuming a normal distribution for the error function $\varepsilon(X)$, consequently, the likelihood function for $\mathbf{y}$ is

$$L(\beta_0,\sigma^2,\theta,P)=\frac{1}{\sqrt{2\pi^n(\sigma^2)^n \mid \mathbf{R} \mid}}\exp\{-\frac{1}{2}\frac{(\mathbf{y_S}-\beta_0\mathbf{1})^T\mathbf{R}^{-1}(\mathbf{y_S}-\beta_0\mathbf{1})}{\sigma^2}\} \tag{E.16}$$

The parameters θ_h are found after maximizing the likelihood function E.16 . To do so, a GA algorithm was used in the current study. Assuming $\mathbf{r}$ is the correlations between the error term at the interested point $\mathbf{X}'$ and training samples $\mathbf{X}^{\mathrm{i}}$ for $i=1,...,n$,

$$\mathbf{r}=\begin{Bmatrix} Corr(X^{(1)},X') \\ Corr(X^{(2)},X') \\ \vdots \\ Corr(X^{(n)},X') \end{Bmatrix} \tag{E.17}$$

the best linear unbiased predictor of y($\mathbf{X}'$) is [84],

$$y(\mathbf{X}')=\beta_0+\mathbf{r}^T(\mathbf{X})\mathbf{R}^{-1}(\mathbf{y_S}-\beta_0\mathbf{1}) \tag{E.18}$$

There are different correlation models to be used for kriging development known as Exponential, Squared Exponential, Linear, Spherical and Matern [21]. The Kriging described above is called ordinary Kriging (OK) [52]. The universal Kriging (UK) replaces β_0 in equation (E.18) by $f(\mathbf{X})^T\beta$, where $f(\mathbf{X})$ is a P-dimensional vector of known functions of $\mathbf{X}$ and β. Most Kriging models uses the ordinary type as for the universal type it is required to find extra (P-1) unknown parameters. For the current study an ordinary Kriging with Squared Exponential correlation model was used.

E.2 Sampling Methods

As the surrogate model is fitted to the samples, the accuracy of the estimation is highly dependent to the sample placements in the problem landscape unfolding the phenomena design of experiments (DOEs). In other words, building a surrogate model requires generation of a set of initial sample points. In order to have a better understanding of the system by the surrogate model, the initial population should cover whole parameter space at a certain discrete resolution. There are many ways to sample the parameter domain. Two most popular methods are Monte Carlo Simulation and Latin Hypercube Sampling (LHS).

E.2.1 Monte Carlo Simulation

The Monte Carlo sampling was the first formal method of the modern DoE as this method tries to fill the domain uniformly by randomly placing the samples in the domain [35]. In fact, Monte Carlo simulation (MCS) or pseudo-random sampling firstly proposed by Metropolis and Ulam [62] is a traditional method for sampling that randomly examines the cumulative distributions to obtain a set of samples hoping to result in space-filling of the domain. Considering a surrogate model having N variable parameters, the MCS generate $N \times L$ number of samples in a random selection from [0,1] and maps to the cumulative distribution functions for every N variable. The MCS was later improved by the method of Stratified Monte Carlo Sampling (SMCS) to provide more uniform distribution by dividing the domain into non-random strata then applying the MCS over every territory.

E.2.2 Latin Hypercube Sampling

Latin Hypercube Sampling (LHS) was firstly introduced by McKay et al [60]. The LHS method benefit from the advantage of stratifying each univariate mean simultaneously which causes uniform sampling of the univariate distribution. Moreover, the sampling is done by LHS on a basis of random selection which provides unbiased series of samples. Considering N variable parameters for the surrogate model, LHS stratify the cumulative distribution function of every parameter variable to L levels which leads to L^{N} hypercubes. Then select a number in every hypercube by uniform random process. Doing this, the drawback of non-uniformity of random distribution is rectified, while, the unbiased nature of the selection is maintained.

Orthogonal Sampling is a type of LHS which induce even distribution of samples over the entire searching domain. The maximinLHS as a post process after LHS run tries to maximize the distance between samples in the searching domain [45]. In this method an initial point is selected randomly in the design parameters domain then the next point is selected from the available locations (which are already discretized by stratifying process of LHS) in a way that the new point has the most minimum distance to the already selected points. This process leads to a multi-dimensional uniform distribution of samples over the parameters domain. One may find other types of LHS in the literature, such as orthogonal-array-based LHS designs [55], orthogonal-maximinLHS designs [48] and orthogonal and nearly orthogonal designs [16].

Appendix F

Multi-district non-continuous domain

In real applications of optimization, especially in mechanical problems, the function we are dealing with is not always a continuous function and also the function is not a mathematical function. In fact, usually the response of mechanical analysis is a black box function in which there are many numerical calculations combined to reach the solution. In these cases, the problem is not only the high computational time needed to reach the optimum but also due to the non-feasibility of some large parts of domain, the Genetic Algorithm may not be able to reach the global optimum.

In this section two ideas were utilized in order to cope this problem. Firstly, the different feasible districts of a search domain is detected. Then, using the information of districts, the mutation operation in the GA is replaced by a random pattern to force the algorithm search some districts other than the one in which the optimizer is trapped in. Second, the non-feasibility was rectified introducing a penalty function to the black box function in order to make it a continuous function through its search domain.

F.1 Finding Districts

In order to find different districts in a domain a Latin Hypercube Sampling was used to distribute a number of samples on the domain, then the samples feasibility were examined. It is worth noting that the feasibility check of a set of parameters in mechanical problems is usually a fast calculation. Then, the Euclidean distance among sample points are calculated. If the distance between two sample points are small enough they are tagged the same district number. By performing this process the input points in the working domain which are close together are tagged with the same district number means that they are in the same district. Doing this, different districts in a searching domain is determined.

Then, the standard mutation procedure in the GA is replaced with a selection method based on a roulette wheel method in a way that the smallest district has the highest probability for being selected. Such procedure provides a change for the optimizer to periodically check the small outland districts to check if an optimum may be found in them.

For evaluating the performance of this method an artificial black box function having two distinct districts was provided by Rastrigins function (which is a bench mark to examine the optimization efficiency). The feasible domains lay in the range of [1-5] and [7-9] in a two dimensional of total [0-10] working domain (Fig. F.1). As seen, there are two districts in which the feasibility exists and in between is the non-feasible domain. Moreover, the global optimum is set in the smaller district (at point [8,8]).

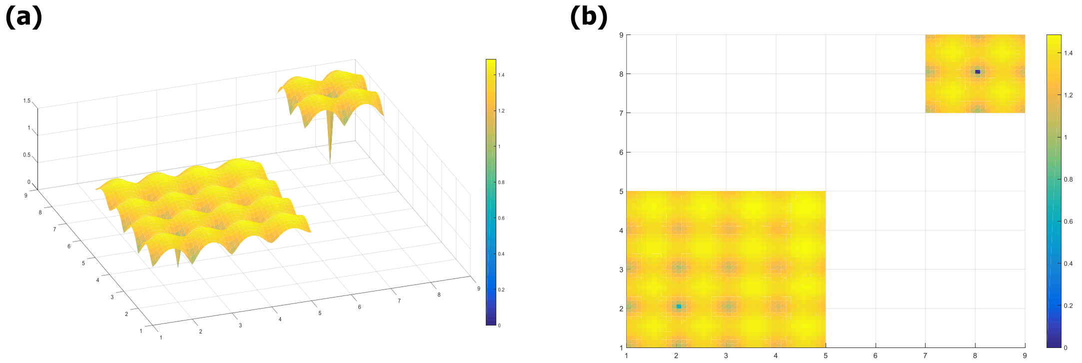

Figure F.1: Manipulated Rastrigins Function as a benchmark a) 3D view b) Top View.

F.2 Rectifying non-continuity

In order to make the function continuous, the response function was replaced by a penalty function for the non feasible space as below,

$$Y_{Penalty} = max(\mathbf{Y}_{Samples}) \times (1 + L_P(Y_i, \mathbf{Y}_{Samples})), \text{ if, } \mathbf{X}_i \in \{\text{Non-feasible Space}\} \tag{F.1}$$

Where, $L_P(Y_i, \mathbf{Y}_{Samples})$ is the euclidean distance of input vector, $\mathbf{X}_\mathrm{i}$ to the nearest sample point. The resultant function is shown in fig. F.2.

The genetic algorithm code has been modified to take into account the arrangements required for comparing the function with death and adaptive penalty. Also the new method of mutation has been applied to the new GA code. In order to make the optimization possible for the case in which the response function is not continuous (to which adaptive penalty has not been applied) the non-feasible points are given a zero fitness value to make the optimizer to filter out these points from the population. Such method is called death penalty method.

The optimization was performed for 100 generations and the number of population was 30. For adding more complexity to the case study, the dimension of the problem

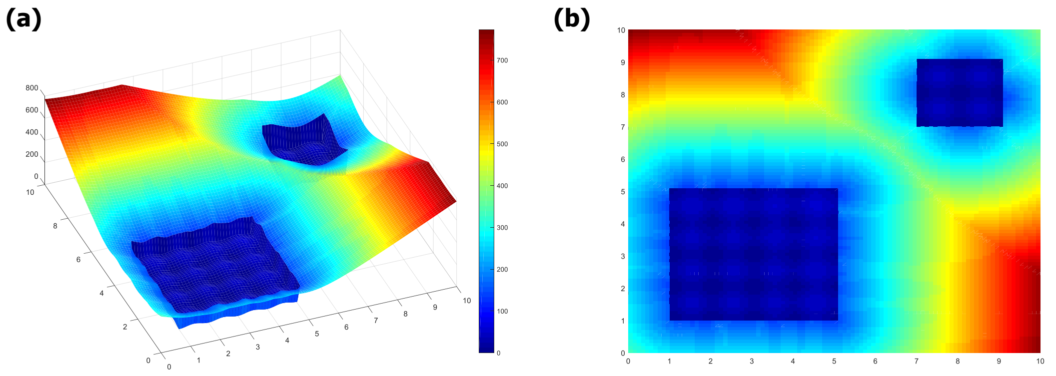

Figure F.2: Adaptive Penalty on Rastrigins Function a) 3D view b) Top View.

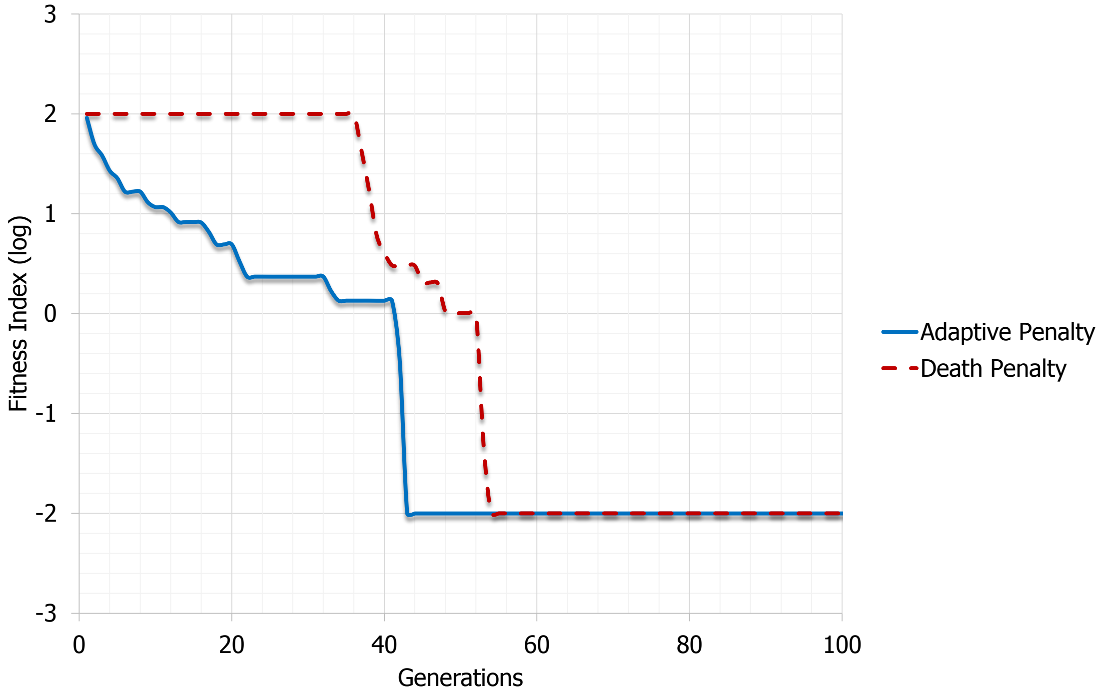

Figure F.3: Optimization Convergence by GA applying adaptive and death penalty on Rastrigins function.

was set to 6. The comparison of the results for both methods are graphed in fig. F.3. Moreover, in a high number of trails, GA could not find a feasible space, hence, failed to converge. To have an estimation of GA convergence failure using death penalty and standard mutation, 150 trails were performed. The results revealed that the rate of success in the case of applying death penalty and standard mutation is 46% (70 out of 150) while by applying adaptive penalty and district finder mutation, a hundred percent of trails were successful and converged to the optimum. More details about the proposed adaptive penalty method for the case of blade and disc attachment are found in next section.

F.3 Corresponding Codes

In this section the code developed with MATLAB to assess two methods proposed to address the non-feasibility in the searching domain has been prepared.

Test functions

Penalty added

```
function y=fitvalucomplex(x)
    global X_Dist Y_Dist % the values for feasible districts
    index=1;
    for i=1:length(x)
        if (x(i)<1||x(i)>5),index=0;end;
    end;
    if index==1,y=rastriginsfcn(x-2)+0.01;else y=inf;end
    index=1;
    for i=1:length(x)
        if (x(i)<7||x(i)>9),index=0;end;
    end;
    if index==1,y=rastriginsfcn(x-8);end
    if y==inf
        Lp=inf;
        for i=1:length(X_Dist)
        L=0;
        for j=1:length(x)
            L=L+(x(j)-X_Dist(i,j))^2;
        end
        L=L^0.5;
        if L<Lp, Lp=L;end
        end
        y=max(Y_Dist)+max(Y_Dist)*Lp^1;
    end
end
```

Original

```
function y=fitvalu(x)
    index=1;
    for i=1:length(x)
        if (x(i)<1||x(i)>5),index=0;end;
    end;
    if index==1,y=rastriginsfcn(x-2)+0.01;else y=inf;end
    index=1;
    for i=1:length(x)
        if (x(i)<7||x(i)>9),index=0;end;
    end;
    if index==1,y=rastriginsfcn(x-8);end
end
```

District Finder

```
function ProximityCheck(proximity,samplenumbers)
    global OPTIONS
    Parametersnumber=OPTIONS.numVar;
    % lb=[10 ,20 ,5 ,5 ,10 ,4];
    % ub=[90 ,100 ,40 ,30 ,60 ,60];
    lb=ones(1,Parametersnumber)*0;
    ub=ones(1,Parametersnumber)*10;
    samples(samplenumbers,Parametersnumber,lb,ub);
    global X_Original Y_Original district X_Dist Y_Dist
    X_Dist=X_Original; % X=X(:,1:Parametersnumber);
    Y_Dist=Y_Original;
    a=zeros(length(Y_Dist),1);
    X_Dist=[X_Dist,a];
    counter=1;
    for i=1:length(X_Dist)
        if Y_Original(i) =inf
            Y_Dist(counter)=Y_Original(i);
            X_Dist(counter,1:Parametersnumber)=X_Original(i,:);
            counter=counter+1;
        end
    end
    Y_Dist=Y_Dist(1:counter-1);
    X_Dist=X_Dist(1:(counter-1),:);
    district=1;
```

```
    % proximity=0.04;
    for i=1:(length(X_Dist(:,1))-1)
        % display(i)
        if Y_Dist(i) =inf
            for j=(i+1):length(X_Dist(:,1))
            if (Y_Dist(j) =inf)
            index=1;
        for k=1:Parametersnumber
        if ((X_Dist(j,k)+proximity*(ub(k)-lb(k)))<X_Dist(i,k))||((X_Dist(j,k)-proximity*(ub(k)-
lb(k)))>X_Dist(i,k))
        index=0;
        end
    end
        if index==1
            if X_Dist(i,Parametersnumber+1)==0
        if X_Dist(j,Parametersnumber+1)>0
            X_Dist(i,Parametersnumber+1)=X_Dist(j,Parametersnumber+1);
        else
            X_Dist(i,Parametersnumber+1)=district;
            X_Dist(j,Parametersnumber+1)=district;
            district=district+1
        end
        else
        if X_Dist(j,Parametersnumber+1)>0
            if X_Dist(j,Parametersnumber+1) =X_Dist(i,Parametersnumber+1)
        for p=1:length(X_Dist(:,1))
            if X_Dist(p,Parametersnumber+1)==max(X_Dist(j,Parametersnumber+1),X_Dist(i,Para
    X_Dist(p,Parametersnumber+1)=min(X_Dist(j,Parametersnumber+1),X_Dist(i,Parametersnumber+
            end
        end
    end;
    else
        X_Dist(j,Parametersnumber+1)=X_Dist(i,Parametersnumber+1);
    end
    end
    end
    end
    end
    if X_Dist(i,Parametersnumber+1)==0
    X_Dist(i,Parametersnumber+1)=district;
    district=district+1
    end
```

```
    end
    end
    display(’District fist step done’);
    % if X(length(X),Parametersnumber+1)==0
    % X(length(X),Parametersnumber+1)=district;
    % end
    district =[];
    for i =1:length(X_Dist(:,1))
    index=0;
    for j=1:length(district)
    if X_Dist(i,Parametersnumber+1)==district(j),index=1;end
    end
    if index==0,district=[district,X_Dist(i,Parametersnumber+1)];end
    end
    district=[district(2:length(district));zeros(1,length(district)-1)];
    for i=1:length(X_Dist(:,1))
    for k=1:length(district(1,:))
    if X_Dist(i,Parametersnumber+1)==district(1,k)
    district(2,k)=district(2,k)+1;
    end
    end
    end
    X=[];
    for i=1:length(X_Dist(:,1))
    if X_Dist(i,Parametersnumber+1) =0,X=[X;X_Dist(i,:)];end
    end
    X_Dist=X;
    % display(X)
    display(strcat(’Number of districts: ’,num2str(length(district))))
    % display(district)
    district=[district;district(2,:)+mean(district(2,:))];
    district=[district;1-(district(3,:)/sum(district(3,:)))];
end
```

Sampling with LHS

```
  function samples(samplenumbers,Parametersnumber,lb,ub)
% global X Y
global X_Original Y_Original
X=lhsdesign(samplenumbers,Parametersnumber);% ,’criterion’,’maximin’,’iterations’,2);
display(’LHS finished’);
```

```
for i=1:length(X)
for j=1:Parametersnumber
X(i,j)=(ub(j)-lb(j))*X(i,j)+lb(j);
end
end
Y=zeros(length(X),1);
for i=1:length(Y)
Y(i)=fitvalu(X(i,:)); % min(fitvalu(X(i,:)),1000);
end
X_Original=X;
Y_Original=Y;
end
```

Modified GA by District Random method

```
function [MinCost] = GADist(ProblemFunction, DisplayFlag)
global district X_Dist
% Genetic algorithm for optimizing a general function.
% INPUTS: ProblemFunction is the handle of the function that returns
% the handles of the initialization, cost, and feasibility functions.
% DisplayFlag says whether or not to display information during iterations and plot results.
if  exist('DisplayFlag', 'var')
DisplayFlag = false ; % true;
end
[OPTIONS, MinCost, AvgCost, InitFunction, CostFunction, FeasibleFunction, ... Population] = InitDist(DisplayFlag, ProblemFunction);
pin=zeros(OPTIONS.popsize,2);
Xover_Type = 1; % crossover type: 1 = single point, 2 = two point, 3 = uniform
OPTIONS.pcross = 1; % crossover probability
OPTIONS.pmutate = 0.01; % initial mutation probability
Keep = 2; % elitism parameter: how many of the best individuals to keep from one generation to the next
% Begin the evolution loop
for GenIndex = 1 : OPTIONS.Maxgen
% Compute the inverse of the cost. Fitness increases with inverse cost.
InverseCost = [];
for i = 1 : OPTIONS.popsize
InverseCost = [InverseCost, 1 / Population(i).cost];
end
for k = Keep+1 : 2 : OPTIONS.popsize % begin selection/crossover loop
```

```
% Select two parents to mate and create two children - roulette wheel selection
mate = [];
for selParents = 1 : 2
Random_Cost = rand * sum(InverseCost);
Select_Cost = InverseCost(1);
Select_index = 1;
while Select_Cost < Random_Cost
Select_index = Select_index + 1;
if Select_index > OPTIONS.popsize
disp(’error:Select_index > OPTIONS.popsize’);
break; %disp(InverseCost);Select_index,Select_Cost,
end
Select_Cost = Select_Cost + InverseCost(Select_index);
end
mate = [mate Select_index];
end
Parent(1, :) = Population(mate(1)).chrom;
Parent(2, :) = Population(mate(2)).chrom;
% Crossover
switch Xover_Type
case 1
% single point crossover
if OPTIONS.pcross > rand
% crossover the parents
Xover_Pt = ceil(rand * OPTIONS.numVar);
% x = genes in parent 1 that are not in parent 2 (after crossover point)
x = setdiff(Parent(1, Xover_Pt:OPTIONS.numVar), Parent(2, Xover_Pt:OPTIONS.numVar));
% y = genes in parent 2 that are not in parent 1 (after crossover point)
y = setdiff(Parent(2, Xover_Pt:OPTIONS.numVar), Parent(1, Xover_Pt:OPTIONS.numVar));
child(k-Keep, :) = [Parent(1, 1:OPTIONS.numVar-length(y)), y];
child(k-Keep+1, :) = [Parent(2, 1:OPTIONS.numVar-length(x)), x];
else
% clone the parents
child(k-Keep, :) = Parent(1, :);
child(k-Keep+1, :) = Parent(2, :);
end
case 2
% multipoint crossover
if OPTIONS.pcross > rand
Xover_Pt1 = ceil(rand * OPTIONS.numVar);
Xover_Pt2 = ceil(rand * OPTIONS.numVar);
if Xover_Pt1 > Xover_Pt2
```

```
temp = Xover_Pt2;
Xover_Pt2 = Xover_Pt1;
Xover_Pt1 = temp;
end
child(k-Keep, :) = [Parent(1, 1:Xover_Pt1) Parent(2, Xover_Pt1+1:Xover_Pt2) Parent(1, Xover_Pt2+1:OPTIONS.numVar)];
child(k-Keep+1, :) = [Parent(2, 1:Xover_Pt1) Parent(1, Xover_Pt1+1:Xover_Pt2) Parent(2, Xover_Pt2+1:OPTIONS.numVar)];
else
child(k-Keep, :) = Parent(1, :);
child(k-Keep+1, :) = Parent(2, :);
end
case 3
% uniform crossover
for i = 1 : OPTIONS.numVar
if OPTIONS.pcross > rand
child(k-Keep, i) = Parent(1, i);
child(k-Keep+1, i) = Parent(2, i);
else
child(k-Keep, i) = Parent(2, i);
child(k-Keep+1, i) = Parent(1, i);
end
end
end
end % end selection/crossover loop
% Replace the non-elite population members with the new children
for k = Keep+1 : 2 : OPTIONS.popsize
Population(k).chrom = child(k-Keep, :);
Population(k+1).chrom = child(k-Keep+1, :);
end
% Mutation
distp=district(4,:);
```

$$distp, andis$$

```
=sort(distp,’ascend’);
for individual = Keep + 1 : OPTIONS.popsize % Don’t allow the elites to be mutated
if OPTIONS.pmutate > rand
Randn = rand*sum(distp);
Selectp = distp(1);
Select_index = 1;
while Selectp < Randn
```

```
Select_index = Select_index + 1;
if Select_index > OPTIONS.popsize,disp(’error:Select_index in mutation > districts’);
break;end
Selectp = Selectp + distp(Select_index);
end
kk=1;ll=2;
limitkk=floor(rand*length(X_Dist));
while kk<limitkk
if ll>length(X_Dist), ll=1;end
if X_Dist(ll,OPTIONS.numVar+1)==district(1,andis(Select_index)), kk=kk+1;end
ll=ll+1;
end
%district(1,andis(Select_index))
Population(individual).chrom=X_Dist(ll-1,1:OPTIONS.numVar);
end
end
% Make sure the population does not have duplicates.
Population = ClearDupsDist(Population,OPTIONS);
% Make sure each individual is legal.
Population = FeasibleFunction(OPTIONS, Population);
% Calculate cost
Population = CostFunction(OPTIONS, Population);
% Sort from best to worst
Population = PopSortDist(Population,pin);
% Compute the average cost of the valid individuals
[AverageCost, nLegal] = ComputeAveCostDist(Population);
% Display info to screen
MinCost = [MinCost Population(1).cost];
AvgCost = [AvgCost AverageCost];
if DisplayFlag
disp([’GA: The best and mean of Generation # ’, num2str(GenIndex), ’ are ’,... num2str(MinCost(end)),
’ and ’, num2str(AvgCost(end))]);
end
end
Conclude(DisplayFlag, OPTIONS, Population, nLegal, MinCost);
return;
```

Appendix G

Fatigue Life Assessment

In gas or steam turbine engines the blades and disc are exposed to high temperature in addition to high centrifugal forces. The high centrifugal forces provide high stress profile over the components and high temperature deteriorates the material strength which makes the situation even worse. In addition the high vibration of the engine during its normal operation examines the endurance of the components. In fact, the service life of the critical aerospace components are highly affected by different types of degradation such as high cycle fatigue, low cycle fatigue, static yielding, corrosion, erosion, wear and also creep. Among different components of the engines the blade, the disc and also the attachments which holds them together are the most critical components which need especial attention for design as they suffer high thermal and mechanical loads during their service life. These intense conditions are even more detrimental in case of especial heavy operational conditions of the engines such as short take off of an aero-engine in special occasions which cause over-speeding of the disc. The failure in handling the exhausting conditions by the components lead to engine puncture due to a blade off or disc burst. Therefore, the life assessment of the turbine components has a priority importance in design to increase the reliability and safety of the engines. In means that by knowing the service life of the components, the chance of unexpected failure of the engine is reduced and the safety level increases. Although fatigue has been the cause of many failures in different components of the industry yet the mechanism of fatigue has not been fully understood. One may find different studies and valuable books ([85], [79]) devoted to high cycle fatigue ([66], [89], [88], [90], [82]), low cycle fatigue ([29], [41], [86]) and also the fracture mechanics applications in evaluating the crack propagations in different industries in addition to fretting fatigue ([34], [106], [37], [107], [83], [57], [5], [6], [4], [7], [11], [12], [13], [14], [15], [43], [27], [23], [25], [105], [28], [78], [102]). There are lots of parameters affecting the fatigue behavior of components such as the loading condition ([2], [61], [104], [91], [72]), residual stress ([70]), surface morphology ([51]), the material properties ([5]), temperature ([54], [96]), etc. Among all, for the blade attachments, the fretting fatigue is a prominent issue when service life exceeds 4000h ([107], [73]).

G.1 Fretting fatigue

Fretting can happen when two mating surfaces under contact are under high pressure with a relative displacement (local slip) which may cause surface damage and crack nucleation. Small vibratory movement of the contacting surfaces in the attachment during normal operational conditions is the main cause of fretting [79]. The fretting fatigue may introduce significant reduction of life to the components and the crack generated by the fretting fatigue may propagate due to subsequent high cycle fatigue. Hence, to estimate the fretting fatigue life, two phases are considered, which are the crack initiation and the crack propagation. Although several models consider both phases to predict the total life, it is common to consider only the crack initiation for the component attachment lifing [57] especially in the case of blade attachment. There is not a general model for the criteria and the selection of the most proper criteria depends on the component material, geometry, type of contacts and loading conditions.

G.1.1 Critical Plane Approach

1. Kandil et al. [49] presented a shear and normal strain based model, based on the critical plane approach, which postulates that cracks initiate and grow on certain planes and that the normal strains to those planes assist in the fatigue crack growth process. $\gamma_m ax$ is the max shear strain on the critical plane and ε_n is the normal strain on the same plane and S is a constant, N is the cycles to initiation.

$$\gamma_m ax + S \times \varepsilon_n = f(N) \tag{G.1}$$

2. Socie et al. [95] included mean tensile stress to this theory as

$$\frac{\Delta\gamma}{2} + \frac{\Delta\varepsilon_n}{2} + \frac{\sigma_{no}}{E} = f(N) \tag{G.2}$$

   Where, $\Delta\gamma$ is the maximum shear strain amplitude,$\Delta\varepsilon$ is the normal strain amplitude and σ_{no} is the maximum shear strain amplitude.

3. Bannantine and Socie [9] modified the uniaxial parameter proposed by Smith, Watson and Topper (SWT) to account for mean-stress effects for multiaxial loading. Here the maximum principal strain amplitude is modified by $\sigma_{n,max}$ which is the maximum stress in the direction of maximum principal strain amplitude that occurs over one cycle

$$\sigma_{n,max}(\frac{\Delta\varepsilon_1}{2}) = f(N) \tag{G.3}$$

   This Equation has been used for prediction of crack initiation in fretting fatigue, for aluminum, and titanium polycrystalline alloys.

4. Fatemi and Socie [30] suggested a parameter combining the shear strain amplitude and maximum normal stress on the critical plane. The life equation is

$$\gamma_t + k\frac{\sigma_{n,max}}{S_y} = \frac{\tau'_f}{G}(2N_f)^{b'} + \gamma'_f(2N_f)^{c'} \tag{G.4}$$

Where, γ_t is the shear strain amplitude, and $\sigma_{n,max}$ is the maximum normal stress on the critical plane.

G.1.2 Fretting fatigue specific parameters:

1. **Slip amplitude δ**. δ is the relative tangential displacement of contacting particles during the cycle, which is similar to the strain amplitude in conventional fatigue. The parameter was only used in some early studies [71].

2. **Frictional energy dissipation parameter Q**. The Parameter Q, which is also called F1 or fretting wear parameter [23], is given as

$$Q = \tau\delta = \mu\sigma_N\delta \tag{G.5}$$

3. **SWT Parameter**. Under some conditions, fretting fatigue can be considered as fatigue with local stress concentrations. Smith et al. added a mean stress correction to the relation proposed by Coffin and Manson and developed SWT relationship as,

$$SWT = \sigma_1(\frac{\Delta\varepsilon}{2}) = \frac{{\sigma'_f}^2}{E}(2N_f)^{2b} + \sigma'_f\varepsilon'_f(2N_f)^{b+c} \tag{G.6}$$

This parameter can be applied as a criteria for the crack initiation under fretting.

4. **Ruiz's parameter**. Ruiz et al. [83] studied a dovetail joint fretting problem in a typical gas turbine attachment. Three common material types were studied by them: a titanium alloy, Ti-IM1829; a nickel-based alloy, IHCO901; and a chromium-rich steel alloy, FV535. Their study was both experimental investigation of crack observation and FE analysis of the stress over the contacting surfaces in addition to the relative displacement. To provide an interpretation over the location of the crack nucleation, they proposed the parameter K carrying the effects of localized tensile and shear stresses and the relative displacement,

$$K = (\sigma_T)_{max}(\tau\delta)_{max} \tag{G.7}$$

Where, $(\sigma_T)_{max}$, is the maximum tangential stress (tensile stress parallel to the surface) and, $(\tau\delta)_{max}$ is the maximum frictional work, which is the product of the shear stress and slip amplitude, at the surface. Although this parameter could not predict the initiation location, the tendency of cracks to nucleate under a tensile stress and remaining dormant under a compressive stress was considered in this parameter. Ruiz et al, proposed a second model that combined the frictional work parameter $\tau\delta$ and the effect of the tangential stress, σ_T in the form of,

$$\kappa = \sigma_T \tau \delta \tag{G.8}$$

This second parameter, κ, successfully predicted the nucleation location at the edge of contact comparing to the experimental results. This parameter, which is also called F2 or fretting fatigue (FF) parameter, empirically takes into account the evidence that cracks are more likely to develop in regions of tension rather than compression [23]. It can also be described as

$$FF = Q\sigma_T = \tau\delta\sigma_T = \mu\sigma_N\delta\sigma_T \tag{G.9}$$

Where Q is the fretting wear parameter.

Arakere and Swanson [5] studied Crystallographic initiation and crack growth along octahedral planes Single crystal nickel base super-alloy turbine blades. They performed a three dimensional FE analysis over a single crystal turbine blade under centrifugal, thermal and aerodynamic loadings. They provided the stress in the attachment as well as the tip area of the blade as a function of primary and secondary crystal orientation. They found that the maximum shear stress amplitude, $\Delta\tau_{max}$, is the most effective fatigue failure criterion. However, for the fretting fatigue inside the attachment area no correlation could be found to $\Delta\tau_{max}$. For the secondary orientation the damage parameter $\sigma_{max}\Delta\varepsilon/2$ has better correlation with the fretting fatigue crack initiation. Several findings were obtained by Szolwinski et al. [100]. Firstly, the effect of increased friction tends to accelerate the formation of a crack. Also, the effect of material properties in addition to the friction were evaluated. Attention was turned to the field of multiaxial fatigue, which offered models to predict life from cyclic stresses and strains. The Smith-Watson-Topper model for cracks which formed under the influence of localized shear and then turned quickly to grow further on a plane of principal stress seemed to capture the fretting crack nucleation mechanism reported by several researchers. They used an incremental Westergaard function approach to estimate the elastic cyclic stresses and strains for applying the SWT fatigue criteria. The verification showed that the SWT model predicted not only the observed crack origin but also crack orientation. From these estimates, it is concluded that the formation of a fretting fatigue crack consumed most of the total life in the tests considered. Lykins et al. [57] evaluated numerous fatigue parameters in determination of the crack nucleation in a component subjected to plain fatigue under constant amplitude loading. The evaluation was based on the parameter's ability to predict the number of cycles to initiation and location for crack nucleation. They found no significant difference in the results obtained by the critical plane SWT parameter comparing to that of SWT parameter. They resulted almost the same cycles to crack initiation and nucleation location from both parameters. Moreover, by applying the F-S parameter, some difference was found between the plain fatigue and fretting fatigue crack nucleation comparing to other strain and critical plane parameters. The F-S parameter also predicted the location of crack initiation successfully. In addition, after applying the K and FF parameters developed by Ruize, they found that the K parameter is unable to predict the location of the crack initiation due to the fact that the maximum tangential stress does not occur where the maximum frictional work happens. On the other hand, although the FF parameter was ineffective to provide correlation with cycles to crack nucleation it predicted the location of the crack in agree with the experimental data.

G.1.3 Methods based on fracture mechanics

Similar to S-N curve, Naboulsi [68] obtained the crack analogy fatigue (CAF) parameter life curve to predict the fretting life. Later they introduced a geometry correction to develop a modified crack analogy method (MCAM). Due to the analogy, the fretting fatigue life can be approximated using the propagation life. The fretting fatigue crack growth process can be divided into two stages, stage I is the crack initiation from the surface and the stage II is the crack propagation. Alternatively, small crack propagation is considered as an approximation of the fretting fatigue life. Pre-cracks can be located as an initial assumption at the position of peak stress to represent a defect on the contact surface [69], and then the small crack propagation law is used to calculate the propagation life. Findley [31] using the critical plane theory, for ductile metals, proposed that the cracks first nucleate due to shear stress along slip bands in the crystal of the material. It was experimentally observed that the slip bands coincide with the plane of maximum shear strain amplitude. The initial nucleation stage is referred as “stage I” by Forsyth [33]. The crack developed by the initial stage is later propagate alone the plane of maximum principal stress. This process of propagation is known as stage II as labeled by Forsyth [33]. Wei et al. [107] used Sinclair criterion for mesh convergence. They applied local meshing method in the edges of the contacts for more reduction of element size and obtaining more accurate results. For considering the plasticity of the material, a multi-linear constitutive equation combining isotropic strengthen law is used in calculation. Moreover, the coulomb friction model was used to simulate the friction with friction factor of 0.3. They used pre-crack modeling with different angle of crack initiation and propagation then calculating the stress intensity factor they fixed the crack initiation angle according to the mode II. They applied a combination of plastic stress and strain in a multiaxial fatigue critical plane theory to predict the crack nucleation life. Then they used Paris formula to predict the crack propagation. Golden and Naboulsi [37] used a computational hybrid technique (CHT) to obtain the necessary stress distributions required in order to apply damage tolerance analysis of the blade and disc attachment in terms of fretting fatigue. They divided the 3D problem into multiple 2D problems which significantly decreased the computational burden while maintaining the accuracy of the results. In order to predict the life a probabilistic damage tolerance framework were used in which initial crack size were assumed as a random variable.

G.1.4 Prediction of fretting Crack Location in a dovetail

The state of stress in the attachment of the blade and disc is of type multiaxial in nature. Hence, the use of critical plane theories in understanding the fatigue behavior of the contact region is advantageous. In the current study, two type of approaches of critical plane theory and fretting fatigue specific parameter are evaluated in prediction of crack nucleation of the fretting surfaces in a dovetail. The experimental result obtained by [54] is used to make the comparison between the two methods. Firstly, in order to evaluate the state of stress and the relative displacement of the contacting surfaces the dovetail and the disc were modeled and analyzed using FE method. To obtain high accuracy, a high mesh density were applied over and near the contacting surfaces. The SWT parameter in the critical plane were used as the critical plane approach. For applying this method to locate the crack initiation, the state of stress and strain must be determined in all nodal points along the contact surfaces. Then the stress and strain values must be calculated in different angles in order to find the maximum SWT parameter in addition to the critical plane direction. Considering θ as the angle relative to the normal line of the contacting surfaces (see Fig. G.1, the following formula were used to calculate the stress and strain in an arbitrary angle of θ,

$$\sigma_\theta = \frac{\sigma_x + \sigma_y}{2} + \frac{\sigma_x - \sigma_y}{2}\cos(2\theta) + \tau_{xy}\sin(2\theta) \tag{G.10}$$

$$\varepsilon_\theta = \frac{\varepsilon_x + \varepsilon_y}{2} + \frac{\sigma_x - \sigma_y}{2}\cos(2\theta) + \gamma_{xy}\sin(2\theta) \tag{G.11}$$

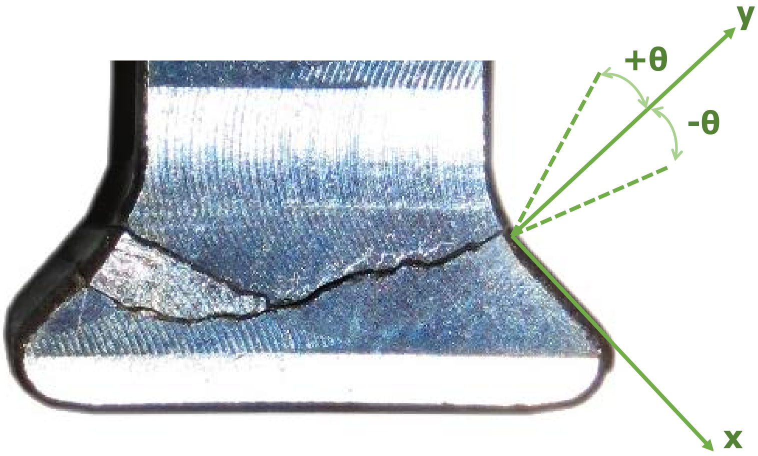

Figure G.1: The angle of critical plane over contacting surfaces in a dovetail attachment.

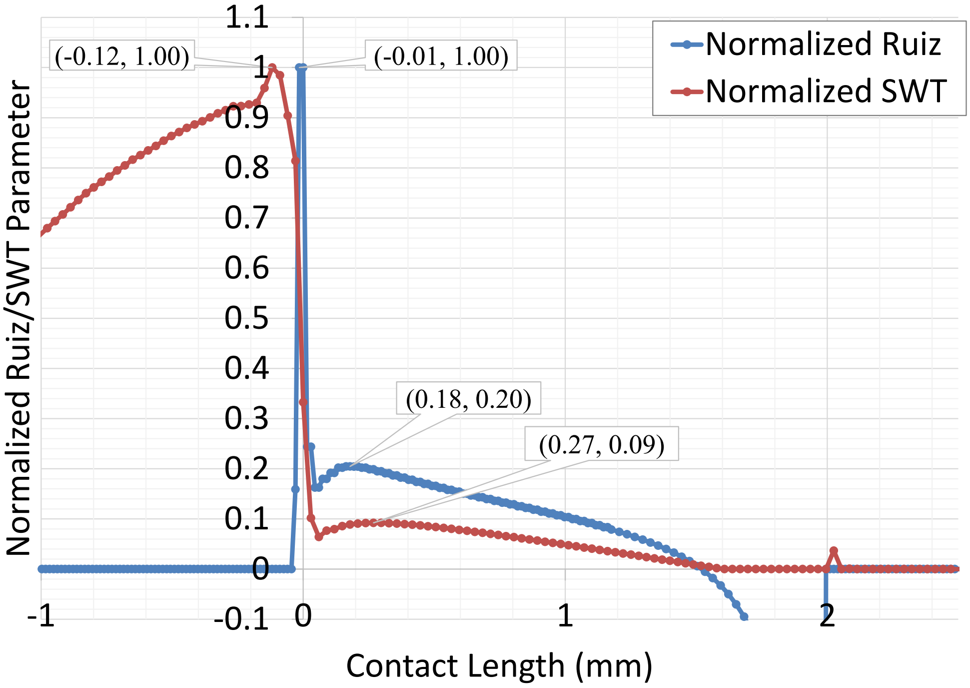

Figure G.2: SWT and Ruize Parameters normalized fretting results over a dovetail.

The SWT parameter in the critical plane and the Ruize parameter were calculated on every node of the contacting surfaces. The graph of the results obtained by both methods are plotted in Fig. G.2. As there are different values obtained for the two methods in order to make the comparison all values are normalized to the maximum value obtained for both methods. The nominal length (the length of the straight line of the contact geometry) of the contact for the dovetail in the current study is 2mm. Both methods predicted the location of the crack initiation near the leading edge of the contact surface and both confirm with the experimental results but as the difference between the results was small it is hard to judge on which method has a higher conformity.

Bibliography

[1] Farhad Alinejad et al. “Reduction of the design space to optimize blade fir-tree attachments”. In: *Proceedings of ASME Turbo Expo 2018: Turbomachinery Technical Conference and Exposition*. 2018.

[2] Kaliyaperumal Anandavel, Raghu V Prakash, and Antonio Davis. “Effect of preloading on the contact stress distribution of a dovetail interface”. In: *International conference on Mechanical and Industrial Engineering (ICMIE 2010), Singapore*. Vol. 69. 2010, pp. 360–365.

[3] Daniel W. Apley, Jun Liu, and Wei Chen. “Understanding the Effects of Model Uncertainty in Robust Design With Computer Experiments”. In: *Journal of Mechanical Design* 128.4 (2006), p. 945. DOI: `10.1115/1.2204974`.

[4] J AraÃºjo. “Analysis of pad size effects in fretting fatigue using short crack arrest methodologies”. In: *International Journal of Fatigue* 21.9 (Oct. 1999), pp. 947–956. DOI: `10.1016/s0142-1123(99)00077-8`.

[5] Nagaraj K. Arakere and Gregory Swanson. “Fretting Stresses in Single Crystal Superalloy Turbine Blade Attachments”. In: *Journal of Tribology* 123.2 (2001), p. 413. DOI: `10.1115/1.1308032`.

[6] JA ARAUJO and FC Castro. “A comparative analysis between multiaxial stress and ΔK-based short crack arrest models in fretting fatigue”. In: *Engineering Fracture Mechanics* 93 (2012), pp. 34–47.

[7] J ARAUJO et al. “On the use of the Theory of Critical Distances and the Modified Wöhler Curve Method to estimate fretting fatigue strength of cylindrical contacts”. In: *International Journal of Fatigue* 29.1 (Jan. 2007), pp. 95–107. DOI: `10.1016/j.ijfatigue.2006.02.041`.

[8] J. E. Baker. “Reducing bias and inefficiency in the selection algorithm”. In: *Proceedings of the Second International Conference on Genetic Algorithms on Genetic algorithms and their application*. 1987.

[9] Julie A. Bannantine. *Fundamentals of Metal Fatigue Analysis*. PRENTICE HALL, Sept. 11, 1989. 288 pp. ISBN: 013340191X.

[10] S. Barella et al. “Failure analysis of a third stage gas turbine blade”. In: *Engineering Failure Analysis* 18.1 (Jan. 2011), pp. 386–393. DOI: `10.1016/j.engfailanal.2010.09.017`.

[11] L. Bertini and C. Santus. “Fretting fatigue tests on shrink-fit specimens and investigations into the strength enhancement induced by deep rolling”. In: *International Journal of Fatigue* 81 (Dec. 2015), pp. 179–190. DOI: `10.1016/j.ijfatigue.2015.08.007`.

[12] Nadeem Ali Bhatti, Kyvia Pereira, and Magd Abdel Wahab. “A continuum damage mechanics approach for fretting fatigue under out of phase loading”. In: *Tribology International* 117 (Jan. 2018), pp. 39–51. DOI: `10.1016/j.triboint.2017.08.009`.

[13] Nadeem Ali Bhatti and Magd Abdel Wahab. “A numerical investigation on critical plane orientation and initiation lifetimes in fretting fatigue under out of phase loading conditions”. In: *Tribology International* 115 (Nov. 2017), pp. 307–318. DOI: `10.1016/j.triboint.2017.05.036`.

[14] Nadeem Ali Bhatti and Magd Abdel Wahab. “Finite element analysis of fretting fatigue under out of phase loading conditions”. In: *Tribology International* 109 (May 2017), pp. 552–562. DOI: `10.1016/j.triboint.2017.01.022`.

[15] Nadeem Ali Bhatti and Magd Abdel Wahab. “Fretting fatigue crack nucleation: A review”. In: *Tribology International* 121 (May 2018), pp. 121–138. DOI: `10.1016/j.triboint.2018.01.029`.

[16] D. Bingham, R. R. Sitter, and B. Tang. “Orthogonal and nearly orthogonal designs for computer experiments”. In: *Biometrika* 96.1 (Jan. 2009), pp. 51–65. DOI: `10.1093/biomet/asn057`.

[17] Mattias Björkman and Kenneth Holmström. “Global Optimization of Costly Nonconvex Functions Using Radial Basis Functions”. In: *Optimization and Engineering* 1.4 (2000), pp. 373–397. DOI: `10.1023/a:1011584207202`.

[18] D. Botto and F. Alinejad. “Innovative Design of Attachment for Turbine Blade Rotating at High Speed”. In: *Volume 7A: Structures and Dynamics*. ASME, June 2017. DOI: `10.1115/gt2017-64959`.

[19] D. Brujic et al. “Shape Optimisation in CAE”. In: *EUROCON 2005 - The International Conference on "Computer as a Tool"*. IEEE, 2005. DOI: `10.1109/eurcon.2005.1629977`.

[20] Djordje Brujic et al. “CAD based shape optimization for gas turbine component design”. In: *Structural and Multidisciplinary Optimization* 41.4 (Nov. 2009), pp. 647–659. DOI: `10.1007/s00158-009-0442-9`.

[21] Hao Chen et al. “Analysis Methods for Computer Experiments: How to Assess and What Counts?” In: *Statistical Science* 31.1 (Feb. 2016), pp. 40–60. DOI: `10.1214/15-sts531`.

[22] W. Chen, M. M. Wiecek, and J. Zhang. “Quality Utility—A Compromise Programming Approach to Robust Design”. In: *Journal of Mechanical Design* 121.2 (1999), p. 179. DOI: `10.1115/1.2829440`.

[23] M Ciavarella and G Demelio. “A review of analytical aspects of fretting fatigue, with extension to damage parameters, and application to dovetail joints”. In: *International Journal of Solids and Structures* 38.10-13 (Mar. 2001), pp. 1791–1811. DOI: `10.1016/s0020-7683(00)00136-0`.

[24] M Ciavarella, D A Hills, and G Monno. “The influence of rounded edges on indentation by a flat punch”. In: *Proceedings of the Institution of Mechanical Engineers, Part C: Journal of Mechanical Engineering Science* 212.4 (Apr. 1998), pp. 319–327. DOI: `10.1243/0954406981521259`.

[25] M Ciavarella and G Macina. “New results for the fretting-induced stress concentration on Hertzian and flat rounded contacts”. In: *International Journal of Mechanical Sciences* 45.3 (Mar. 2003), pp. 449–467. DOI: `10.1016/s0020-7403(03)00061-4`.

[26] Stella M. Clarke, Jan H. Griebsch, and Timothy W. Simpson. “Analysis of Support Vector Regression for Approximation of Complex Engineering Analyses”. In: *Journal of Mechanical Design* 127.6 (2005), p. 1077. DOI: `10.1115/1.1897403`.

[27] D. Nowell D. A. Hills. *Mechanics of Fretting Fatigue*. Springer Netherlands, Dec. 8, 2010. 256 pp. ISBN: 9048144094.

[28] Daniele Dini, David Nowell, and Igor N. Dyson. “The use of notch and short crack approaches to fretting fatigue threshold prediction: Theory and experimental validation”. In: *Tribology International* 39.10 (Oct. 2006), pp. 1158–1165. DOI: `10.1016/j.triboint.2006.02.033`.

[29] Norman E. Dowling. “Mean Stress Effects in Stress-Life and Strain-Life Fatigue”. In: *SAE Technical Paper Series*. SAE International, Apr. 2004. DOI: `10.4271/2004-01-2227`.

[30] Ali Fatemi and Darrell F. Socie. “A CRITICAL PLANE APPROACH TO MULTIAXIAL FATIGUE DAMAGE INCLUDING OUT-OF-PHASE LOADING”. In: *Fatigue & Fracture of Engineering Materials and Structures* 11.3 (Mar. 1988), pp. 149–165. DOI: `10.1111/j.1460-2695.1988.tb01169.x`.

[31] William Nicholas Findley. *A theory for the effect of mean stress on fatigue of metals under combined torsion and axial load or bending*. 6. Engineering Materials Research Laboratory, Division of Engineering, Brown University, 1958.

[32] Alexander I.J. Forrester and Andy J. Keane. “Recent advances in surrogate-based optimization”. In: *Progress in Aerospace Sciences* 45.1-3 (Jan. 2009), pp. 50–79. DOI: `10.1016/j.paerosci.2008.11.001`.

[33] PJE Forsyth. “A two stage process of fatigue crack growth”. In: *Proceedings of the Crack Propagation Symposium*. Vol. 1. Cranfield. 1961, pp. 76–94.

[34] Camille Gandiolle and Siegfried Fouvry. “Stability of critical distance approach to predict fretting fatigue cracking: a “ ℓ opt – b opt ” concept”. In: *International Journal of Fatigue* 82 (Jan. 2016), pp. 199–210. DOI: `10.1016/j.ijfatigue.2015.07.016`.

[35] Sushant S. Garud, Iftekhar A. Karimi, and Markus Kraft. “Design of computer experiments: A review”. In: *Computers & Chemical Engineering* 106 (Nov. 2017), pp. 71–95. DOI: `10.1016/j.compchemeng.2017.05.010`.

[36] David E. Goldberg. *Genetic Algorithms in Search, Optimization, and Machine Learning*. Addison-Wesley Professional, 1989. ISBN: 0201157675.

[37] Patrick J. Golden and Sam Naboulsi. “Hybrid contact stress analysis of a turbine engine blade to disk attachment”. In: *International Journal of Fatigue* 42 (Sept. 2012), pp. 296–303. DOI: `10.1016/j.ijfatigue.2012.01.023`.

[38] Youngwon Hahn and John I. Cofer. “Design Study of Dovetail Geometries of Turbine Blades Using Abaqus and Isight”. In: *Volume 7: Structures and Dynamics, Parts A and B*. ASME, June 2012. DOI: `10.1115/gt2012-68566`.

[39] Rolland L. Hardy. “Multiquadric equations of topography and other irregular surfaces”. In: *Journal of Geophysical Research* 76.8 (Mar. 1971), pp. 1905–1915. DOI: `10.1029/jb076i008p01905`.

[40] J. Haslinger and R. A. E. Mäkinen. *Introduction to Shape Optimization: Theory, Approximation, and Computation (Advances in Design and Control)*. Society for Industrial and Applied Mathematics, 2003. ISBN: 0-89871-536-9.

[41] Jianfu Hou, Bryon J Wicks, and Ross A Antoniou. “An investigation of fatigue failures of turbine blades in a gas turbine engine by mechanical analysis”. In: *Engineering Failure Analysis* 9.2 (Apr. 2002), pp. 201–211. DOI: `10.1016/s1350-6307(01)00005-x`.

[42] H. Murthy I.G. Goryacheva and T.N. Farris. “Contact problem with partial slip for the inclined punch with rounded edges”. In: *International Journal of Fatigue* 24.11 (Nov. 2002), pp. 1191–1201. DOI: `10.1016/s0142-1123(02)00026-9`.

[43] ASTM International. *Fretting Fatigue: Advances in Basic Understanding and Applications (Astm Special Technical Publication, 1425,)* ASTM International, 2003. ISBN: 0-8031-3456-8.

[44] R. Jin, W. Chen, and T.W. Simpson. “Comparative studies of metamodelling techniques under multiple modelling criteria”. In: *Structural and Multidisciplinary Optimization* 23.1 (Dec. 2001), pp. 1–13. DOI: `10.1007/s00158-001-0160-4`.

[45] M.E. Johnson, L.M. Moore, and D. Ylvisaker. “Minimax and maximin distance designs”. In: *Journal of Statistical Planning and Inference* 26.2 (Oct. 1990), pp. 131–148. DOI: 10.1016/0378-3758(90)90122-b.

[46] Donald R. Jones, Matthias Schonlau, and William J. Welch. “Efficient Global Optimization of Expensive Black-Box Functions”. In: *Journal of Global Optimization* 13.4 (1998), pp. 455–492. DOI: 10.1023/a:1008306431147.

[47] Kenneth De Jong. “Analysis of the behavior of a class of genetic adaptive systems”. PhD thesis. University of Michigan, 1975.

[48] V. Roshan Joseph and Ying Hung. “Orthogonal-Maximin latin hypercube designs”. In: *Statistica Sinica* 18.1 (2008), pp. 171–186. ISSN: 10170405, 19968507. URL: http://www.jstor.org/stable/24308251.

[49] F A Kandil, M W Brown, and KJ Miller. “Biaxial low-cycle fatigue failure of 316 stainless steel at elevated temperatures”. In: *Mechanical behaviour and nuclear applications of stainless steel at elevated temperatures*. 1982.

[50] Shyam Karna, Karna D Ph, and A P Scholar. “An Overview on Taguchi Method”. In: (Apr. 2018).

[51] Randall Kelton et al. “Study of the Surface Roughness Evolution of Pinned Fatigue Cracks, and its Relation to Crack Pinning Duration and Crack Propagation Rate Between Pinning Points”. In: *Volume 9: Mechanics of Solids, Structures and Fluids NDE, Structural Health Monitoring and Prognosis*. ASME, Nov. 2017. DOI: 10.1115/imece2017-70729.

[52] Jack P.C. Kleijnen. “Regression and Kriging metamodels with their experimental designs in simulation: A review”. In: *European Journal of Operational Research* 256.1 (Jan. 2017), pp. 1–16. DOI: 10.1016/j.ejor.2016.06.041.

[53] d g Krige. “A Statistical Approach to Some Mine Valuation and Allied Problems on the Witwatersrand”. MA thesis. Witwatersrand, 1951.

[54] Mario Lavella and Daniele Botto. “Fretting Fatigue Analysis of Additively Manufactured Blade Root Made of Intermetallic Ti-48Al-2Cr-2Nb Alloy at High Temperature”. In: *Materials* 11.7 (June 2018), p. 1052. DOI: 10.3390/ma11071052.

[55] Stephen Leary, Atul Bhaskar, and Andy Keane. “Optimal orthogonal-array-based latin hypercubes”. In: *Journal of Applied Statistics* 30.5 (June 2003), pp. 585–598. DOI: 10.1080/0266476032000053691.

[56] M. Luke et al. “Experimental and numerical study on crack initiation under fretting fatigue loading”. In: *International Journal of Fatigue* 86 (May 2016), pp. 24–33. DOI: 10.1016/j.ijfatigue.2015.09.022.

[57] C Lykins. “An evaluation of parameters for predicting fretting fatigue crack initiation”. In: *International Journal of Fatigue* 22.8 (Sept. 2000), pp. 703–716. DOI: 10.1016/s0142-1123(00)00036-0.

[58] Elina Madetoja, Kaisa Miettinen, and Pasi Tarvainen. “Issues related to the computer realization of a multidisciplinary and multiobjective optimization system”. In: *Engineering with Computers* 22.1 (July 2006), pp. 33–46. DOI: `10.1007/s00366-006-0028-8`.

[59] Michael de la Maza and Bruce Tidor. “An Analysis of Selection Procedures with Particular Attention Paid to Proportional and Boltzmann Selection”. In: *Proceedings of the 5th International Conference on Genetic Algorithms*. 1993.

[60] M. D. McKay, R. J. Beckman, and W. J. Conover. “A Comparison of Three Methods for Selecting Values of Input Variables in the Analysis of Output from a Computer Code”. In: *Technometrics* 21.2 (May 1979), p. 239. DOI: `10.2307/1268522`.

[61] S.A. Meguid, P.S. Kanth, and A. Czekanski. “Finite element analysis of fir-tree region in turbine discs”. In: *Finite Elements in Analysis and Design* 35.4 (July 2000), pp. 305–317. DOI: `10.1016/s0168-874x(99)00072-4`.

[62] Nicholas Metropolis and S. Ulam. “The Monte Carlo Method”. In: *Journal of the American Statistical Association* 44.247 (Sept. 1949), pp. 335–341. DOI: `10.1080/01621459.1949.10483310`.

[63] Kaisa Miettinen. *Nonlinear Multiobjective Optimization (International Series in Operations Research & Management Science)*. Springer, 2012. ISBN: 978-1-4613-7544-9.

[64] Melanie Mitchell. *An Introduction to Genetic Algorithms (Complex Adaptive Systems)*. The MIT Press, 1996. ISBN: 9780262133166.

[65] Marco Montemurro. “Optimal Design of Advanced Engineering Modular Systems through a New Genetic Approach”. PhD thesis. Université Pierre et Marie Curie - Paris VI, 2012. URL: `https://tel.archives-ouvertes.fr/tel-00955533/document`.

[66] R Morrissey. “Frequency and stress ratio effects in high cycle fatigue of Ti-6Al-4V”. In: *International Journal of Fatigue* 21.7 (Aug. 1999), pp. 679–685. DOI: `10.1016/s0142-1123(99)00030-4`.

[67] Jayaprakash Murugesan and Yoshiharu Mutoh. “Fretting fatigue strength prediction of dovetail joint and bolted joint by using the generalized tangential stress range–compressive stress range diagram”. In: *Tribology International* 76 (Aug. 2014), pp. 116–121. DOI: `10.1016/j.triboint.2013.11.006`.

[68] Sam Naboulsi. “Applications of crack analogy to fretting fatigue”. In: *Engineering Fracture Mechanics* 72.10 (July 2005), pp. 1610–1623. DOI: `10.1016/j.engfracmech.2004.11.006`.

[69] Carlos Navarro, Sergio Munoz, and Jaime Dominguez. “Propagation in fretting fatigue from a surface defect”. In: *Tribology International* 39.10 (Oct. 2006), pp. 1149–1157. DOI: `10.1016/j.triboint.2006.02.004`.

[70] R.W. Neu. “Progress in standardization of fretting fatigue terminology and testing”. In: *Tribology International* 44.11 (Oct. 2011), pp. 1371–1377. DOI: `10.1016/j.triboint.2010.12.001`.

[71] D. Nowell and D.A. Hills. “Crack initiation criteria in fretting fatigue”. In: *Wear* 136.2 (Mar. 1990), pp. 329–343. DOI: `10.1016/0043-1648(90)90155-4`.

[72] A. de Pannemaecker et al. “Identification of the fatigue stress intensity factor threshold for different load ratios R : From fretting fatigue to C(T) fatigue experiments”. In: *International Journal of Fatigue* 82 (Jan. 2016), pp. 211–225. DOI: `10.1016/j.ijfatigue.2015.07.015`.

[73] P. Papanikos and S. A. Meguid. “Theoretical and experimental studies of fretting initiated fatigue failure of aeroengine compressor discs”. In: *Fatigue & Fracture of Engineering Materials and Structures* 17.5 (May 1994), pp. 539–550. DOI: `10.1111/j.1460-2695.1994.tb00253.x`.

[74] P Papanikos, S.A Meguid, and Z Stjepanovic. “Three-dimensional nonlinear finite element analysis of dovetail joints in aeroengine discs”. In: *Finite Elements in Analysis and Design* 29.3-4 (June 1998), pp. 173–186. DOI: `10.1016/s0168-874x(98)00008-0`.

[75] S. Pierret. “Multi-objective and Multi-Disciplinary Optimization of Three dimensional Turbomachinery Blades”. In: *6th World Congresses of Structural and Multidisciplinary Optimization*. 2005.

[76] Foad Rahimidehgolan, Mohsen Behzadi, and Jalal Fathi Sola. “Obtaining Constants of Johnson-Cook Material Model Using a Combined Experimental, Numerical Simulation and Optimization Method”. In: *World Academy of Science, Engineering and Technology, International Journal of Mechanical, Aerospace, Industrial, Mechatronic and Manufacturing Engineering* 10.9 (2016), pp. 1615–1622.

[77] Foad Rahimidehgolan et al. “Determination of the Constants of GTN Damage Model Using Experiment, Polynomial Regression and Kriging Methods”. In: *Applied Sciences* 7.11 (Nov. 2017), p. 1179. DOI: `10.3390/app7111179`.

[78] R. Rajasekaran and D. Nowell. “Fretting fatigue in dovetail blade roots: Experiment and analysis”. In: *Tribology International* 39.10 (Oct. 2006), pp. 1277–1285. DOI: `10.1016/j.triboint.2006.02.044`.

[79] Ali Fatemi Ralph I. Stephens. *Metal Fatigue in Engineering*. JOHN WILEY & SONS INC, Nov. 11, 2000. 496 pp. ISBN: 0471510599.

[80] Jon T. Richardson et al. “Some Guidelines for Genetic Algorithms with Penalty Functions”. In: *ICGA*. 1989.

[81] Luis Miguel Rios and Nikolaos V. Sahinidis. “Derivative-free optimization: a review of algorithms and comparison of software implementations”. In: *Journal of Global Optimization* 56.3 (July 2012), pp. 1247–1293. DOI: `10.1007/s10898-012-9951-y`.

[82] R Ritchie. “Thresholds for high-cycle fatigue in a turbine engine Ti–6Al–4V alloy”. In: *International Journal of Fatigue* 21.7 (Aug. 1999), pp. 653–662. DOI: `10.1016/s0142-1123(99)00024-9`.

[83] C. Ruiz, P. H. B. Boddington, and K. C. Chen. “An investigation of fatigue and fretting in a dovetail joint”. In: *Experimental Mechanics* 24.3 (Sept. 1984), pp. 208–217. DOI: `10.1007/bf02323167`.

[84] Jerome Sacks et al. “Design and Analysis of Computer Experiments”. In: *Statistical Science* 4.4 (1989), pp. 409–435. ISSN: 0883-4237. DOI: `10.1214/ss/1177012420`.

[85] J. Schijve. *Fatigue of Structures and Materials*. Springer Netherlands, Dec. 16, 2008. URL: `https://www.ebook.de/de/product/19111086/j_schijve_fatigue_of_structures_and_materials.html`.

[86] Sebastian Schmitz et al. “Risk Estimation for LCF Crack Initiation”. In: *Volume 7A: Structures and Dynamics*. ASME, June 2013. DOI: `10.1115/gt2013-94899`.

[87] George A. F. Seber and Alan J. Lee. *Linear Regression Analysis*. Wiley, 2003. ISBN: 978-0-471-41540-4.

[88] M. Shariyat, S. A. Jazayeri, and J. Fathi Sola. “Theoretical and experimental evaluation of performance of CNG engine and pistons fatigue lives employing modified fatigue criteria”. In: *Strength of Materials* 44.4 (July 2012), pp. 438–455. DOI: `10.1007/s11223-012-9398-x`.

[89] M. Shariyat, J. Fathi Sola, and S.A. Jazayeri. “Experimentally Validated Combustion and Piston Fatigue Life Evaluation Procedures for the Bi-Fuel Engines, Using an Integral-Type Fatigue Criterion”. In: *Latin American Journal of Solids and Structures* 13.6 (June 2016), pp. 1030–1053. DOI: `10.1590/1679-78251937`.

[90] M Shen. “Reliability assessment of high cycle fatigue design of gas turbine blades using the probabilistic Goodman Diagram”. In: *International Journal of Fatigue* 21.7 (Aug. 1999), pp. 699–708. DOI: `10.1016/s0142-1123(99)00033-x`.

[91] Liang Shi et al. “An investigation of fretting fatigue in a circular arc dovetail assembly”. In: *International Journal of Fatigue* 82 (Jan. 2016), pp. 226–237. DOI: `10.1016/j.ijfatigue.2015.07.025`.

[92] G. B. Sinclair and N. G. Cormier. “Contact Stresses in Dovetail Attachments: Alleviation via Precision Crowning”. In: *Journal of Engineering for Gas Turbines and Power* 125.4 (2003), p. 1033. DOI: `10.1115/1.1584477`.

[93] G. B. Sinclair et al. “Contact Stresses in Dovetail Attachments: Finite Element Modeling”. In: *Journal of Engineering for Gas Turbines and Power* 124.1 (2002), p. 182. DOI: `10.1115/1.1391429`.

[94] Jaroslaw Sobieszczanski-Sobieski. “Sensitivity of complex, internally coupled systems”. In: *AIAA Journal* 28.1 (Jan. 1990), pp. 153–160. DOI: `10.2514/3.10366`.

[95] DF Socie, P Kurath, and J Koch. “A multiaxial fatigue damage parameter”. In: *ICBMFF2*. 1985.

[96] Staffan Söderberg, U. Bryggman, and Tim McCullough. “Frequency effects in fretting wear”. In: *Wear* 110.1 (July 1986), pp. 19–34. DOI: `10.1016/0043-1648(86)90149-3`.

[97] W. Song and A.J. Keane. “An efficient evolutionary optimisation framework applied to turbine blade firtree root local profiles”. In: *Structural and Multidisciplinary Optimization* 29.5 (Oct. 2004), pp. 382–390. DOI: `10.1007/s00158-004-0486-9`.

[98] Wenbin Song et al. “Local Shape Optimisation of Turbine Disc Firtrees Using NURBS”. In: *9th AIAA/ISSMO Symposium on Multidisciplinary Analysis and Optimization*. American Institute of Aeronautics and Astronautics, Sept. 2002. DOI: `10.2514/6.2002-5486`.

[99] Wenbin Song et al. “Turbine blade fir-tree root design optimisation using intelligent CAD and finite element analysis”. In: *Computers & Structures* 80.24 (Sept. 2002), pp. 1853–1867. DOI: `10.1016/s0045-7949(02)00225-0`.

[100] Matthew P. Szolwinski and Thomas N. Farris. “Mechanics of fretting fatigue crack formation”. In: *Wear* 198.1-2 (Oct. 1996), pp. 93–107. DOI: `10.1016/0043-1648(96)06937-2`.

[101] Genichi Taguchi. *Taguchi on Robust Technology Development: Bringing Quality Engineering Upstream (Asme Press Series on International Advances in Design Productivity)*. ASME Press (American Society of Mechanical Engineers), 1992. ISBN: 0-7918-0028-8.

[102] R Hojjati Talemi, M Abdel Wahab, and P De Baets. “Numerical modelling of fretting fatigue”. In: *Journal of Physics: Conference Series* 305 (July 2011), p. 012061. DOI: `10.1088/1742-6596/305/1/012061`.

[103] Haijun Tang et al. “Fretting fatigue failure of an aero engine turbine blade”. In: *Engineering Failure Analysis* 16.6 (Sept. 2009), pp. 2004–2008. DOI: `10.1016/j.engfailanal.2008.07.010`.

[104] Aditya A. Walvekar et al. “An experimental study and fatigue damage model for fretting fatigue”. In: *Tribology International* 79 (Nov. 2014), pp. 183–196. DOI: `10.1016/j.triboint.2014.06.006`.

[105] Da-Sheng Wei, Liang Shi, and Yan-Rong Wang. “Cyclic plastic behavior of dovetail under fretting load”. In: *Engineering Failure Analysis* 55 (Sept. 2015), pp. 100–114. DOI: `10.1016/j.engfailanal.2015.05.009`.

[106] Da-Sheng Wei, Yan-Rong Wang, and Xiao-Guang Yang. “Analysis of failure behaviors of dovetail assemblies due to high gradient stress under contact loading”. In: *Engineering Failure Analysis* 18.1 (Jan. 2011), pp. 314–324. DOI: `10.1016/j.engfailanal.2010.09.011`.

[107] Da-Sheng Wei, Shan-Hu Yuan, and Yan-Rong Wang. “Failure analysis of dovetail assemblies under fretting load”. In: *Engineering Failure Analysis* 26 (Dec. 2012), pp. 381–396. DOI: `10.1016/j.engfailanal.2012.06.007`.

[108] Lucjan Witek. “Failure analysis of turbine disc of an aero engine”. In: *Engineering Failure Analysis* 13.1 (Jan. 2006), pp. 9–17. DOI: `10.1016/j.engfailanal.2004.12.028`.

[109] Fei Xue et al. “Fretting fatigue crack analysis of the turbine blade from nuclear power plant”. In: *Engineering Failure Analysis* 44 (Sept. 2014), pp. 299–305. DOI: `10.1016/j.engfailanal.2014.05.006`.

This Ph.D. thesis has been typeset by means of the TEX-system facilities. The typesetting engine was pdfLATEX. The document class was `toptesi`, by Claudio Beccari, with option `tipotesi =scudo`. This class is available in every up-to-date and complete TEX-system installation.